

ANALYSIS AND MODELLING OF MACHINE TOOL DYNAMICS AND
CUTTING STABILITY DURING OPERATION

A THESIS SUBMITTED TO
THE GRADUATE SCHOOL OF NATURAL AND APPLIED SCIENCES
OF
MIDDLE EAST TECHNICAL UNIVERSITY

BY

ORKUN ÖZŞAHİN

IN PARTIAL FULFILLMENT OF THE REQUIREMENTS
FOR
THE DEGREE OF DOCTOR OF PHILOSOPHY
IN
MECHANICAL ENGINEERING

MARCH 2014

Approval of the thesis:
ANALYSIS AND MODELLING OF MACHINE TOOL DYNAMICS
AND CUTTING STABILITY DURING OPERATION

submitted by **ORKUN ÖZŞAHİN** in partial fulfillment of the requirements for the degree of **Doctor of Philosophy in Mechanical Engineering Department, Middle East Technical University** by,

Prof. Dr. Canan Özgen _____
Dean, Graduate School of **Natural and Applied Sciences**

Prof. Dr. Suha Oral _____
Head of Department, **Mechanical Engineering**

Prof. Dr. H. Nevzat Özgüven _____
Supervisor, **Mechanical Engineering Dept., METU**

Prof. Dr. Erhan Budak _____
Co-Supervisor, **Faculty of Engineering and Natural Sciences, SU**

Examining Committee Members:

Prof. Dr. Samim Ünlüsoy _____
Mechanical Engineering Dept., METU

Prof. Dr. H. Nevzat Özgüven _____
Mechanical Engineering Dept., METU

Prof. Dr. Yavuz Yaman _____
Aerospace Engineering Dept., METU

Assist. Prof. Dr. Yiğit Yazıcıoğlu _____
Mechanical Engineering Dept., METU

Assist. Prof. Dr. M. Bülent ÖZER _____
Mechanical Engineering Dept., TOBB ETU

Date: 20.03.2014

I hereby declare that all information in this document has been obtained and presented in accordance with academic rules and ethical conduct. I also declare that, as required by these rules and conduct, I have fully cited and referenced all material and results that are not original to this work.

Name, Last name : Orkun Özşahin

Signature :

ABSTRACT

ANALYSIS AND MODELLING OF MACHINE TOOL DYNAMICS AND CUTTING STABILITY DURING OPERATION

ÖZŞAHİN, Orkun

Ph.D., Department of Mechanical Engineering

Supervisor: Prof. Dr. H. Nevzat ÖZGÜVEN

Co-Supervisor: Prof. Dr. Erhan Budak

March 2014, 177 pages

Self-excited vibrations of machine tools during cutting result in process instability, poor surface finish and reduced material removal rate. In order to obtain stability lobe diagrams to avoid chatter vibration, tool point frequency response function (FRF) must be determined. In classical machine tool studies, tool point FRF is obtained experimentally or analytically for the idle state of the machine. However, during cutting operations, discrepancies are frequently observed between the stability diagrams obtained by using FRFs measured at the idle state and the actual stability of the process. These deviations can be attributed to the changes in machine tool dynamics under cutting conditions.

In this thesis, effects due to the operational conditions on machine tool dynamics are investigated. For that purpose, machining center subassemblies (spindle, holder and tool) are modeled using Timoshenko beam model

including gyroscopic effects, and tool point FRF is obtained using structural coupling and modification methods. Using the analytical model, effects of operating conditions on machine tool dynamics are investigated for different spindle – holder – tool assemblies and cutting speeds. In addition to the analytical modeling, variations of machine tool dynamics during operation are also investigated experimentally. A new identification method is proposed for the identification of in process tool point FRFs. Then, experimentally and analytically obtained FRFs are used in the identification of the spindle bearing parameters under cutting conditions. Finally, for a real machining center, tool point FRFs under operating conditions are determined using the identified speed dependent bearing dynamics and the analytical model proposed. Analytically calculated tool point FRFs are verified through chatter tests.

Keywords: Machine Tool Dynamics, Gyroscopic Effects, Chatter Stability

ÖZ

OPERASYON SIRASINDAKİ TEZGAH TAKIM DİNAMİĞİNİN VE KESME KARARLILIĞININ ANALİZİ VE MODELLENMESİ

ÖZŞAHİN, Orkun

Doktora, Makina Mühendisliği Bölümü

Tez Yöneticisi: Prof. Dr. H. Nevzat ÖZGÜVEN

Ortak Tez Yöneticisi: Prof. Dr. Erhan Budak

Mart 2014, 177 sayfa

Talaşlı imalatta kesme sırasında karşılaşılan kendinden kaynaklı titreşimler işlem kararsızlığı, düşük yüzey kalitesi ve talaş kaldırma oranının azalması ile sonuçlanmaktadır. Tırlamadan kaçınmak amacıyla kararlılık diyagramlarının elde edilmesi için Takım ucu frekans tepki fonksiyonunun (FTF) belirlenmesi gerekmektedir. Klasik takım tezgahı çalışmalarında takım ucu FTF'si tezgahın statik durumu için deneysel ya da analitik olarak elde edilmektedir. Halbuki, kesme sırasında, tezgahın statik durumu için elde edilen FTF'ler ile belirlenen kararlılık diyagramları ile işlemin gerçek kararlılığı arasında çoğunlukla farklılıklar gözlenmektedir. Bu farklılıklar kesme sırasında makina dinamiğinde meydana gelen değişimlere bağlı olduğu düşünülebilir.

Bu tez kapsamında, operasyon koşullarının tezgah dinamiği üzerindeki etkileri araştırılmıştır. Bu amaçla işleme merkezi alt bileşenleri (iş mili, takım tutucu

ve takım), jiroskopik etkilerin dahil edildiđi Timoshenko ubuk modeli kullanılarak modellenmiř ve takım u nokta FTF'si yapısal birleřtirme ve deđiřiklik yntemleri kullanılarak elde edilmiřtir. Analitik model kullanılarak operasyon řartlarının tezgah dinamiđi zerindeki etkileri farklı iř mili – takım tutucu – takım sistemleri ve kesme hızları iin arařtırılmıřtır. Analitik modellemeye ek olarak, kesme sırasında takım tezgahında meydana gelen deđiřiklikler deneysel olarak da arařtırılmıřtır. İřlem sırasındaki takım u nokta FTF'sinin belirlenmesi iin yeni bir yntem nerilmiřtir. Ayrıca, deneysel ve analitik olarak elde edilen FTF'ler operasyon kořulları altındaki rulman parametrelerinin belirlenmesinde kullanılmıřtır. Son olarak, gerek bir iřleme merkezinde, operasyon kořullarındaki takım u nokta FTF'si, hıza bađlı olarak belirlenen rulman dinamiđi ve analitik model kullanılarak hesaplanmıřtır. Analitik olarak elde edilen takım u nokta FTF'si tırlama testleri ile dođrulanmıřtır.

Anahtar Kelimeler: Tezgah Dinamiđi, Jiroskopik Etkiler, Tırlama Kararlılıđı.

To my wife and family

ACKNOWLEDGMENTS

The author expresses sincere appreciation to Prof. Dr. H. Nevzat Özgüven and Prof. Dr. Erhan Budak for their excellent supervision, valuable advices and guidance throughout all stages of this study.

Thanks are also due to Dr. L. Taner Tunç, Dr. Emre Özlü, Mr. Deniz Aslan for their helps in experimental procedure and for their contribution and criticisms.

Special acknowledgements are due to the author's family for their support during this work. He also offers his deepest appreciation to his wife for her love, support and understanding.

This work is also supported by Scientific and Technological Research Council of Turkey (TUBITAK) under the project numbers 110M52 and 108M340.

TABLE OF CONTENTS

ABSTRACT	v
ÖZ.....	vii
ACKNOWLEDGMENTS	x
TABLE OF CONTENTS	xi
LIST OF TABLES	xiv
LIST OF FIGURES.....	xvii
LIST OF SYMBOLS.....	xxiii
CHAPTERS	
1 INTRODUCTION	1
1.1 Chatter Stability and Machine Tool Dynamics	1
1.2 Literature Review	7
1.3 Scope of Thesis.....	10
1.4 Outline of Thesis.....	11
2 MATHEMATICAL MODELING.....	15
2.1 Modeling of the Rotating Timoshenko Beam	15
2.2 Free Vibration Solution for Rotating Timoshenko Beam.....	21
2.3 Forced Vibration Response of Rotating Timoshenko Beam	23
2.4 FRFs of Multi Segment Beams by Receptance Coupling	32
2.5 Including Bearing Dynamics	34
2.6 Elastic Coupling of Subassembly Dynamics	37
2.7 Numerical Case Studies	39
2.7.1 Verification of the Model	39
2.7.2 Computational Efficiency of the Method.....	45

3	EFFECT ANALYSIS OF GYROSCOPIC MOMENTS AND SPEED DEPENDENT BEARING STIFFNESS VARIATIONS ON TOOL POINT FRF AND STABILITY	47
3.1	Case Study 1	47
3.2	Case Study 2	55
3.3	Case Study 3	61
3.4	Case Study 4	64
4	EXPERIMENTAL IDENTIFICATION OF THE TOOL POINT FRF..	69
4.1	Spectral Density Measurement	69
4.2	Mass Loading Effect of Accelerometers on Tool Point FRF	72
4.3	Standard Cutting	73
4.4	Cutting with Specially Designed Workpiece	80
5	INVERSE STABILITY SOLUTION FOR IN PROCESS TOOL POINT FRF IDENTIFICATION	85
5.1	Mathematical Formulation.....	85
5.2	Application on real machining center	90
5.2.1	Case Study 1	90
5.2.2	Case Study 2	106
5.2.3	Case Study 3	113
6	IDENTIFICATION OF BEARING DYNAMICS.....	121
6.1	Identification of Bearing Parameters at Idle State	121
6.2	Identification of Contact Parameters	127
6.3	Effect of Bearing Dynamics on Tool Point FRF	128
6.4	Identification of Bearing Dynamics under Operational Conditions	132
7	EXPERIMENTAL VERIFICATION AND CASE STUDIES	143
7.1	Case Study 1	143
7.2	Case Study 2	150

8	CONCLUSIONS.....	159
8.1	Conclusions.....	159
8.2	Recommendations for Future Work	164
	REFERENCES	165
	CURRICULUM VITAE	175

LIST OF TABLES

TABLES

Table 2-1 Front and rear bearing properties.....	40
Table 2-2 Spindle dimensions.....	41
Table 2-3 Holder dimensions.....	41
Table 2-4 Tool dimensions.....	41
Table 2-5 Tool dimensions.....	45
Table 3-1 Spindle dimensions for case study 1.....	48
Table 3-2 Tool Dimensions for case study 1.....	48
Table 3-3 Holder Dimensions for case study 1.....	48
Table 3-4 Dynamic properties of the bearings and interfaces for case study 1.....	49
Table 3-5 Variations in the stability limits for different spindle speeds.....	52
Table 3-6 Updated bearing parameters for case study 1.....	53
Table 3-7 Dynamic properties of the bearings at the idle state.....	56
Table 3-8 Updated bearing parameters according to rotational speed.....	58
Table 3-9 Tool dimensions for case study 3.....	61
Table 3-10 Dynamic properties of the bearings at the idle state for case study 3.....	62
Table 3-11 Updated bearing parameters according to rotational speed for case study 3.....	62
Table 3-12 Tool Dimensions for case study 4.....	65
Table 4-1 Spindle speeds and corresponding tooth passing frequencies for the tool with 4 cutting edges.....	77
Table 4-2 Spindle speeds and corresponding tooth passing frequencies for the tool with 1 cutting edge.....	78
Table 5-1 Holder dimensions.....	91
Table 5-2 Tool Dimensions.....	91
Table 5-3 Modal parameters of the tool point FRF in x-direction.....	93
Table 5-4 Modal parameters of the tool point FRF in y-direction.....	93

Table 5-5 Predicted and actual values of the chatter frequency and axial depth of cut.....	99
Table 5-6 Identified modal parameters in x direction at various spindle speeds	100
Table 5-7 Identified modal parameters in y direction at various spindle speeds	101
Table 5-8 Predictions obtained using modified stability diagrams and actual values of the chatter frequency and axial depth of cut.	105
Table 5-9 Predicted and actual values of the chatter frequency and axial depth of cut for 7500 rpm spindle speed with changing feed.....	108
Table 5-10 Identified modal parameters in x direction at 7500 rpm spindle speed with various feed	109
Table 5-11 Identified modal parameters in y direction at 7500 rpm spindle speed with various feed	109
Table 5-12 Predictions obtained using idle condition, modified stability diagrams and actual values of the chatter frequency and axial depth of cut. .	111
Table 5-13 Modal parameters of the tool mode in x and y directions.....	115
Table 5-14 Predicted and actual values of the chatter frequency and axial depth of cut.....	116
Table 5-15 Identified modal parameters for tool mode in x direction at various spindle speeds.....	117
Table 5-16 Identified modal parameters in y direction at various spindle speeds.	118
Table 5-17 Actual values of the chatter frequency and axial depth of cut and predicted values by modified stability diagrams.	119
Table 5-18 Actual values of the chatter frequency and axial depth of cut and predicted values by modified stability diagrams.	120
Table 6-1 Spindle Dimensions	121
Table 6-2 Initial estimates of the interface parameters for x direction	122
Table 6-3 Initial estimates of the bearing parameters for x direction	123
Table 6-4 Dynamic properties of the interfaces in x direction.....	124
Table 6-5 Dynamic properties of the bearings in x direction.....	124

Table 6-6 Dynamic properties of the interfaces in y direction.	125
Table 6-7 Dynamic properties of the bearings in y direction.	125
Table 6-8 Identified speed dependent bearing stiffness values in x direction.	133
Table 6-9 Identified speed dependent bearing stiffness values in y direction.	133
Table 6-10 Actual values of the chatter frequency and axial depth of cut at limit and predicted values by in process FRFs and idle FRFs.	138
Table 6-11 Identified force dependent bearing stiffness values in x direction.	141
Table 6-12 Identified force dependent bearing stiffness values in y direction.	141
Table 7-1 Holder dimensions	144
Table 7-2 Actual stability limit and stability predictions using idle FRFs and in process FRF.	149
Table 7-3 Holder dimensions	150
Table 7-4 Contact parameters at holder – tool interface in x and y direction.	151
Table 7-5 Predicted and actual values of axial depth of cut.	158

LIST OF FIGURES

FIGURES

Figure 1-1 Turbine blade surface due to chatter.....	2
Figure 1-2 Cutting tool – workpiece interaction and chip thickness variation. .	2
Figure 1-3 Stability diagram of the cutting operation.	3
Figure 1-4 Tool point FRF measurement using impact test [14].	4
Figure 1-5 Machining center subassemblies.	5
Figure 1-6 Modeling approach of spindle – holder – tool assembly.....	6
Figure 1-7 Analytically obtained stability diagram and chatter test results [14].	7
Figure 2-1 Rotating Timoshenko beam generalized coordinates	15
Figure 2-2 Receptance coupling of two beams.	32
Figure 2-3 Including bearing dynamics to the rotor segment by structural modification.....	35
Figure 2-4 Subassemblies (Spindle, holder and tool) and contact parameters at spindle – holder and holder – tool interfaces.	38
Figure 2-5 Multi-segment rotor (spindle – holder – tool assembly) supported by asymmetric bearings.....	40
Figure 2-6 Tool point FRF in the x-z plane calculated using ANSYS and the analytical model.	42
Figure 2-7 Tool point FRF in the y-z plane calculated using ANSYS and analytical model.	43
Figure 2-8 Cross FRFs between the two orthogonal planes obtained with ANSYS and analytical model.....	43
Figure 2-9 Tool point FRF in the x-z plane calculated by the analytical model for the idle state and for 40000 rpm spindle speed.....	44
Figure 3-1 Comparison of the tool point FRFs calculated by using the analytical model for the idle state and for 25000 rpm spindle speed.	50

Figure 3-2 Stability diagrams predicted using the tool tip FRFs for the idle state and 25 000 rpm spindle speed.	51
Figure 3-3 Tool point FRF calculated by the analytical model for the idle state and for 25000 rpm spindle speed rotating condition.	53
Figure 3-4 Stability diagrams predicted using the tool tip FRFs for 25 000 rpm spindle speed with and without bearing stiffness variation effect.	54
Figure 3-5 Tool point FRF calculated by the analytical model for the idle state and for 25000 rpm spindle speed rotating condition.	56
Figure 3-6 Stability diagrams predicted using the tool tip FRFs for idle state and 25 000 rpm spindle speed without bearing stiffness variation effect.	57
Figure 3-7 Tool point FRF calculated by the analytical model for the idle state and for 25000 rpm spindle speed rotating condition with bearing stiffness variation.	59
Figure 3-8 Stability diagrams predicted using the tool tip FRFs for idle state and for 25 000 rpm spindle speed with and without bearing stiffness variation effect.	60
Figure 3-9 Tool point FRF calculated by the analytical model for the idle state and for 15000 rpm spindle speed rotating condition with and without bearing stiffness variation.	63
Figure 3-10 Stability diagrams predicted using the tool tip FRFs for idle state and for 15 000 rpm spindle speed with and without bearing stiffness variation effect.	64
Figure 3-11 Tool point FRF calculated by the analytical model for the idle state and for 15000 rpm spindle speed rotating condition with and without bearing stiffness variation.	65
Figure 3-12 Stability diagrams predicted using the tool tip FRFs for idle state and for 15 000 rpm spindle speed with and without bearing stiffness variation effect.	66
Figure 4-1 The effects of the measurement noise on both input and output. ...	70
Figure 4-2 Tool point–holder cross FRF (G12).	74
Figure 4-3 Spectrum of the cutting force in the x-direction with respect to the spindle axis.	75

Figure 4-4 Frequency spectrum of the laser vibrometer measurement.	76
Figure 4-5 Measurement locations for the cutting forces and response on the machining center.	79
Figure 4-6 Tool point – holder cross FRFs for static case and during cutting operation.	79
Figure 4-7 Workpiece with random surface profile.	81
Figure 4-8 Coherence function between the cutting force in the x direction with respect to the spindle axis and vibrometer measurement.	82
Figure 4-9 Tool point – holder cross FRFs for static case and during cutting operation at spindle speeds 500 rpm, 1000 rpm and 2000 rpm.	83
Figure 5-1 Inverse stability solution procedure.	89
Figure 5-2 Tool point FRF in the x – direction at the idle state.	92
Figure 5-3 Tool point FRF in the y – direction at the idle state.	92
Figure 5-4 Comparison of tool point FRF in x direction obtained using modal testing with that calculated using identified modal values.	94
Figure 5-5 Comparison of tool point FRF in y direction obtained using modal testing with that calculated using identified modal values.	94
Figure 5-6 Experimental setup.	95
Figure 5-7 Frequency spectrum of microphone measurement of the stable cutting operation at 14000 rpm spindle speed.	96
Figure 5-8 Frequency spectrum of microphone measurement of the unstable cutting operation at 14000 rpm spindle speed.	97
Figure 5-9 Workpiece surface after stable and unstable cutting operations.	98
Figure 5-10 Stability diagrams obtained for idle state and chatter test results.	99
Figure 5-11 Idle condition tool point FRF and calculated tool point FRF using identified parameters for 7400-7500 rpm spindle speed in x direction.	102
Figure 5-12 Idle condition tool point FRF and calculated tool point FRF using identified parameters for 7400-7500 rpm spindle speed in y direction.	102
Figure 5-13 Stability diagrams obtained for idle state and 6300 rpm – 6400 rpm spindle speeds.	103
Figure 5-14 Stability diagrams obtained for idle state and 7400 rpm – 7500 rpm spindle speeds.	104

Figure 5-15 Stability diagrams obtained for idle state and 13900 rpm - 14000 rpm spindle speeds.	104
Figure 5-16 Stability diagrams obtained by idle state FRF with radial immersion of 100% and 50%.	106
Figure 5-17 Stability diagrams obtained by idle state FRF with feed 0.08 mm/tooth and 0.2 mm/tooth.	107
Figure 5-18 Stability diagrams obtained by idle state FRF and identified in process FRFs at 7500 rpm spindle speed with feed of 0.1 mm/tooth, 0.16 mm/tooth, and 0.2 mm/tooth.	110
Figure 5-19 Cutting forces in x direction	112
Figure 5-20 Cutting forces in y direction	112
Figure 5-21 Cutting forces in z direction.....	113
Figure 5-22 Tool point FRF in x – direction at the idle state.....	114
Figure 5-23 Tool point FRF in y – direction at the idle state.....	114
Figure 5-24 Stability diagrams obtained for idle state and chatter test results.	116
Figure 6-1 Tool point FRF in the x direction for the idle state obtained using impact testing and initially estimated interface parameters and bearing parameters.....	123
Figure 6-2 Analytically and experimentally obtained tool point FRFs in the x direction for the idle state.	126
Figure 6-3 Analytically and experimentally obtained tool point FRFs in the y direction for the idle state.	126
Figure 6-4 Effect of translational stiffness of front bearing on tool point FRF in x direction.....	129
Figure 6-5 Effect of rotational stiffness values of front bearing on tool point FRF in x direction.....	130
Figure 6-6 Effect of translational stiffness values of rear bearing on tool point FRF in x direction.....	131
Figure 6-7 Effect of rotational stiffness values of rear bearing on tool point FRF in x direction.....	132

Figure 6-8 Analytically determined tool point FRFs in x direction for idle state and 6400 rpm spindle speed.	134
Figure 6-9 Analytically determined tool point FRFs in y direction for idle state and 6400 rpm spindle speed.	135
Figure 6-10 Analytically obtained stability diagrams for idle state, 6300 rpm spindle speed and chatter test results.	136
Figure 6-11 Analytically obtained stability diagrams for idle state, 7500 rpm spindle speeds and chatter test results.	137
Figure 6-12 Analytically obtained stability diagrams for idle state, 14000 rpm spindle speeds and chatter test results.	137
Figure 6-13 Stability diagram calculated using tool point FRF at 6300 rpm spindle speed, 14000 rpm spindle speed and combined stability diagram valid at all spindle speeds.	139
Figure 6-14 Stability diagram calculated using tool point FRF at idle state and combined stability diagram valid at all spindle speeds.	140
Figure 7-1 Analytically and experimentally obtained tool point FRFs in the x direction for the idle state.	144
Figure 7-2 Analytically and experimentally obtained tool point FRFs in the y direction for the idle state.	145
Figure 7-3 Analytically determined tool point FRFs in x direction for idle state, 6000 rpm and 7000 rpm spindle speeds.	146
Figure 7-4 Analytically determined tool point FRFs in y direction for idle state, 6000 rpm and 7000 rpm spindle speeds.	147
Figure 7-5 Analytically obtained stability diagrams for idle state, 6000 rpm spindle speed and chatter test results.	148
Figure 7-6 Analytically obtained stability diagrams for idle state, 7000 rpm spindle speed and chatter test results.	148
Figure 7-7 Analytically and experimentally obtained tool point FRFs in the x direction for the idle state.	152
Figure 7-8 Analytically and experimentally obtained tool point FRFs in the y direction for the idle state.	152

Figure 7-9 Stability diagrams predicted using the tool tip FRFs for idle state, 14000 rpm and 35000 rpm spindle speed (effects of operating speed on bearing dynamics are not considered).	153
Figure 7-10 Effect of translational stiffness values of rear bearing on tool point FRF.	154
Figure 7-11 Effect of rotational stiffness values of front bearing on tool point FRF.	155
Figure 7-12 Stability diagrams predicted using the tool tip FRFs for idle state and 8500 rpm spindle speed with bearing stiffness variation effect.....	156
Figure 7-13 Stability diagrams predicted using the tool tip FRFs for idle state and 12500 rpm spindle speed with bearing variation effect.....	157

LIST OF SYMBOLS

ϕ_x	Bending rotation angle about x-axis
ϕ_y	Bending rotation angle about y-axis
u_x	Transverse displacement about x axis
u_y	Transverse displacement about y axis
u_z	Axial displacement
ρ	density
I	Cross-sectional area moment of inertia
J	Polat moment of inertia
Ω	Rotational speed
E	Young's Modulus
A	Cross sectional area
G	Shear modulus
k	Shear coefficient
$M(x,t)$	Bending moment
$S(x,t)$	Shear force
$U_x(z)$	Transverse displacement eigenfunction
$\theta_y(z)$	Bending rotation eigenfunction
$q_r(t)$	Time domain modal coordinate of the r -th mode
T	Kinetic energy of the rotating Timoshenko beam
V	Potential energy of the rotating Timoshenko beam
W	Work done by the external force and moments
H_{mn}	Receptance function (Linear displacement at point m due to the unit harmonic force excitation at point n)
L_{mn}	Receptance function (Linear displacement at point m due to the unit harmonic moment excitation at point n)

N_{mn}	Receptance function (Angular displacement at point m due to the unit harmonic force excitation at point n)
P_{mn}	Receptance function (Angular displacement at point m due to the unit harmonic moment excitation at point n)
A_r	Coefficient of mass normalized r-th eigenfunction
$[D]$	Modification matrix
α	Receptance function
k_x	Translational stiffness
c_y	Translational damping
k_θ	Rotational stiffness
c_θ	Rotational damping
ω	excitation frequency
ω_n	natural frequency
ω_c	chatter frequency
ω_r	r-th natural frequency
$S_{xy}(f)$	cross power spectrum
S_{xx}	power spectral density functions
γ_{xy}	Coherence function
$H_1(f)$	Type 1 FRF estimator
$H_2(f)$	Type 2 FRF estimator
$H_3(f)$	Type 3 FRF estimator
K_t	Tangential force coefficient
K_r	Radial force coefficient

Abbreviations

FRF	Frequency Response Function
FEM	Finite Element Method
FEA	Finite Element Analysis

LDV Laser Doppler Vibrometer
EVP Eigen Value Problem

CHAPTER 1

INTRODUCTION

This introductory chapter aims at presenting the need of understanding chatter stability theory, machine tool modeling strategies and machine tool dynamics under operational conditions.

1.1 Chatter Stability and Machine Tool Dynamics

Chatter is a major problem causing poor surface finish, low material removal rate, machine tool failure, increased tool wear, excessive noise and increased cost for machining applications (Figure 1-1). Most important cause of chatter is the regenerative mechanism of the cutting operations and this regenerative mechanism can be explained with the cutting tool and workpiece interaction. As shown in Figure 1-2, cutting tool can be treated as a flexible element in two orthogonal directions, and during cutting operation cutting forces which are proportional to chip thickness excite cutting tool in radial and tangential directions. Therefore, cutting forces cause tool vibrations, and tool vibrations result in wavy profile on the workpiece surface. As shown in Figure 1-2, with the rotation of cutting tool, each cutting teeth removes wavy surface left from the previous teeth and creates a wavy surface again due to tool vibration. Depending on the phase difference between two successive waves, maximum chip thickness may exponentially grow while oscillating at a chatter frequency that is close to but not equal to dominant structural mode in the system [1]. Thus, chip with variable thickness is created during cutting operation and variable chip thickness cause variable cutting forces. This is a closed loop system since variable forces cause tool to vibrate, and vibrating tool results wavy surface, and again wavy surface results in variable cutting forces.

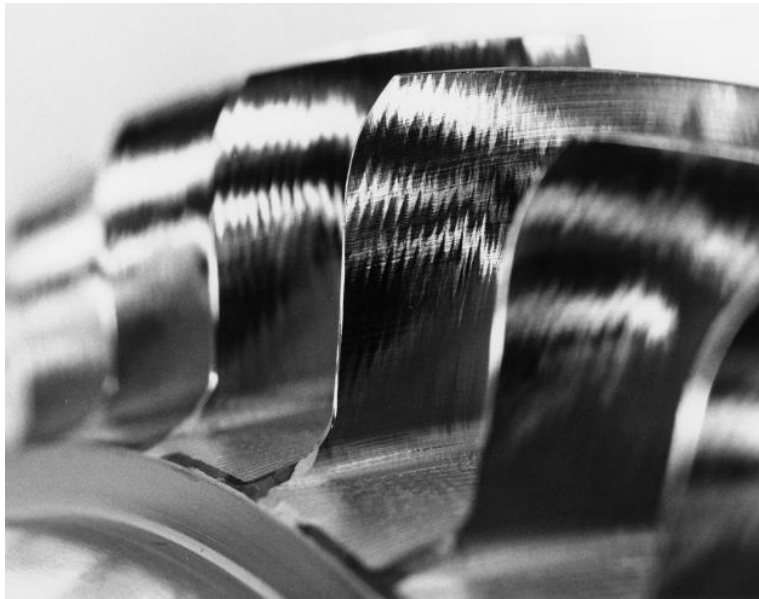


Figure 1-1 Turbine blade surface due to chatter.

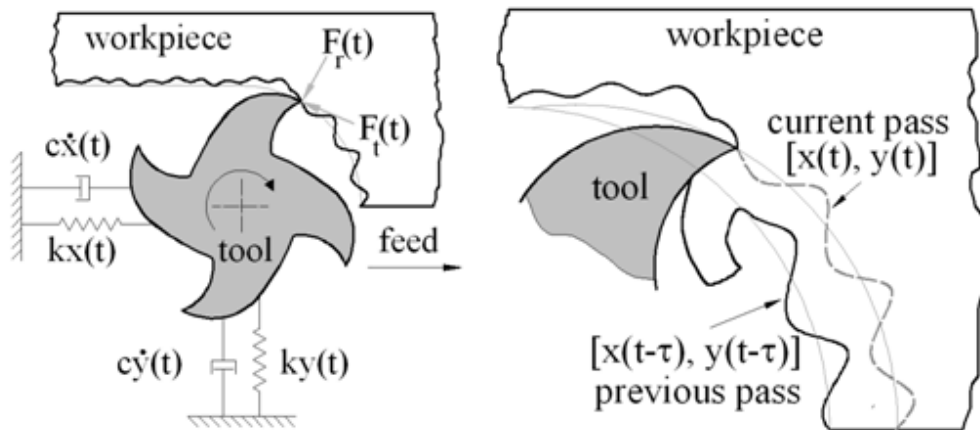


Figure 1-2 Cutting tool – workpiece interaction and chip thickness variation.

In order to avoid chatter, mechanisms of dynamic cutting process have been examined in detail for decades [1-5], and stability diagrams (Figure 1-3), which

provide stable regions in terms of the depth of cut and spindle speed combinations, have been developed [3-6]. Implementation of stability theory to production causes considerable increase in productivity. For instance, using stability diagram given in Figure 1-3, instead of performing cutting operation at 8000 rpm spindle speed with 1 mm axial depth of cut, machining can be performed at 12000 rpm spindle speed with 7 mm axial depth of cut which leads to 10 times faster production.

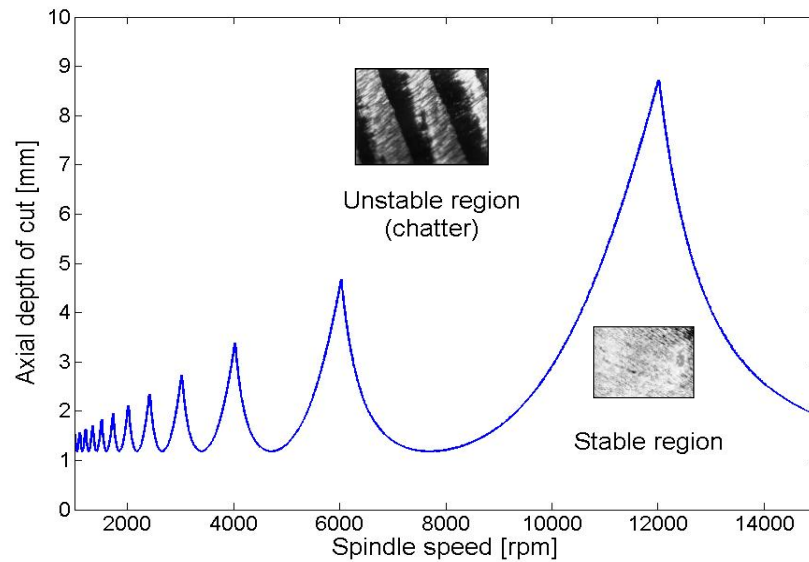


Figure 1-3 Stability diagram of the cutting operation.

In order to obtain stability diagrams, frequency response functions (FRF) at the tool tip are needed. In general, tool point FRF is obtained experimentally using impact testing (Figure 1-4). In experimental procedure, tool point FRF is obtained with exciting the machining center at the tool tip with an impact hammer which also measures the impact force, and measuring the response

with an accelerometer at the tool tip. Then, using spectrum of excitation and response measurements, tool point FRF is calculated.



Figure 1-4 Tool point FRF measurement using impact test [14].

As seen from Figure 1-4, impact tests require additional time before machining operations and in order to obtain stability diagrams, modal testing must be performed and tool point FRF should be determined for every combination of spindle, holder and tool, which is time consuming and may be costly, especially for production machines. These experimental limitations have lead researchers to investigate analytical methods to model machining centers consist of spindle, holder and tool subassemblies as shown in Figure 1-5 which would eliminate the dependency on experiments.

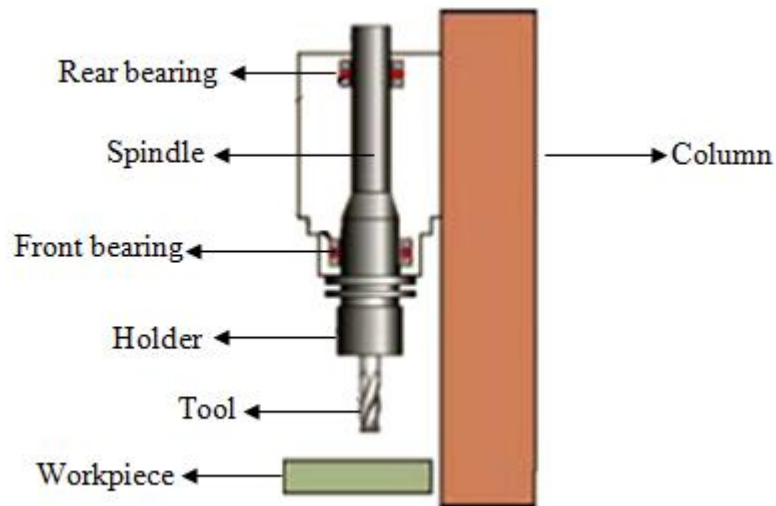


Figure 1-5 Machining center subassemblies.

In order to obtain tool point FRF analytically; Schmitz et al. [7-9] proposed a semi – analytical method which applies the receptance coupling technique to couple the experimentally obtained spindle – holder subassembly receptances with the analytically obtained tool receptances using the contact parameters at the holder tool interface. Schmitz’s semi - analytical method in determining the tool point FRF has been followed by several studies based on receptance coupling method [10-12]. In addition to semi –analytical models, Ertürk et al. [13] proposed an experimentally verified [13,14] analytical model for predicting the tool point FRF by combining the receptance coupling and structural modification techniques where all components of the spindle-holder-tool assembly were modeled analytically with the Timoshenko beam theory, and combined with the contact parameters at the spindle – holder and holder – tool interfaces as shown in Figure 1-6.

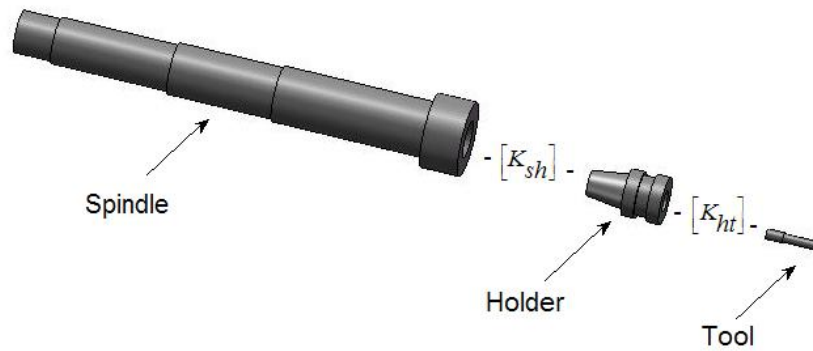


Figure 1-6 Modeling approach of spindle – holder – tool assembly.

However, during cutting operations, discrepancies between calculated stability diagrams and actual stability of the process are frequently observed as shown in Figure 1-7 [14]. One major contributor to these deviations is the changes in machine dynamics under cutting conditions. Because, during high speed cutting operations gyroscopic moments, centrifugal forces and temperature increase cause variations in bearing dynamics. In addition to variations in bearing dynamics, dynamic properties of the subassemblies (spindle, holder and tool) are also affected from gyroscopic moments. Thus tool point FRFs measured at idle state or calculated analytically for idle state of the machining center may lead to incorrect chatter predictions. Therefore, for high speed cutting operations, development of a modeling approach including rotational effects plays a crucial role in accurate prediction of the chatter stability.

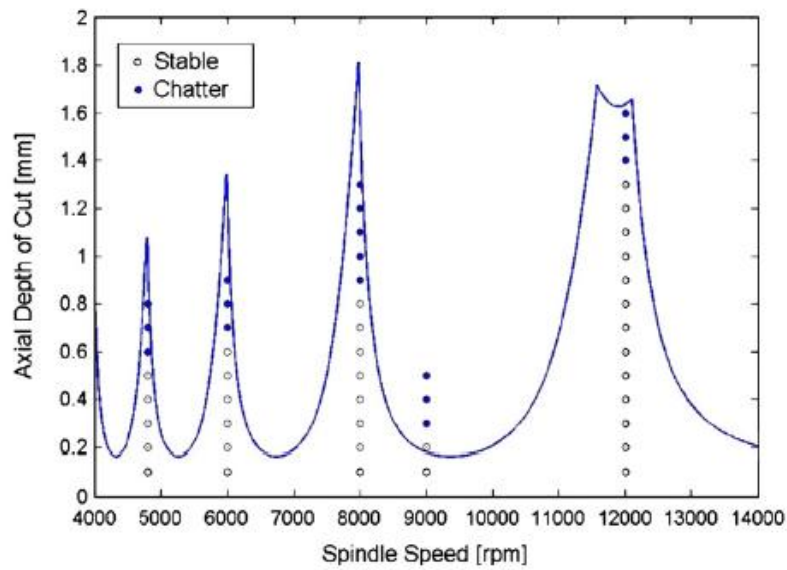


Figure 1-7 Analytically obtained stability diagram and chatter test results [14].

1.2 Literature Review

As shown in previous section in Figure 1-7, discrepancies between calculated stability diagrams and actual stability of the process are frequently observed and these deviations can be attributed to variations in the machining center dynamic properties which may vary due to gyroscopic moments, thermal expansions and centrifugal forces. These effects appear during cutting operation and cause significant changes on the system dynamics. Due to the gyroscopic effects, natural frequencies and corresponding modes of the system separate into backward and forward modes [15-17]. Also due to the gyroscopic effects, unlike non rotating systems, dynamic responses of the rotating system in two orthogonal planes are coupled. Thus, cross coupling effects should be considered in analytical modeling of rotating systems.

In addition to the system dynamics, bearing characteristics are also affected by the rotational effects. During high rotational speeds, centrifugal forces and

gyroscopic moments act on the balls of the bearings pressing the balls toward the outer race. This effect causes changes in the contact angles and kinematics of the balls as well as redistributing the contact loads in the bearing which leads to decreased stiffness [18]. On the contrary, damping of the ball bearings increases under the rotational effects [18]. In order to model bearing behavior under high rotational speeds, Stone [19] proposed a general theory which includes gyroscopic and centrifugal effects. Harris [20] also proposed a method that requires solution of nonlinear equations numerically, and showed variation of the bearing stiffness under high spindle speeds with different preloads.

Since there exists various effects that cause tool point FRF under operational conditions, for accurate prediction of tool point FRF, researchers developed models including rotational effects for the machine tool analysis [21-24]. However; in all this studies machine tool dynamics is modeled using FEM. In addition to gyroscopic and centrifugal effects, thermal expansions may also cause variations in the contact conditions of bearings, and thus affect dynamic properties of the bearings. In order to include thermal effects, thermo-mechanical models have also been proposed [25-27]. Therefore, for the accurate modeling of the spindle–holder–tool assemblies in the machining centers, these effects should be considered.

Similar to the machine tool dynamics researches, in the rotor dynamics research area, FEM became the main analysis tool in the last two decades [28-34]. In addition to the FEM, Frew and Scheffer [35] applied numerical methods based on modified Euler equations, and Chena et al. [36] applied pseudo mode shape method for rotor – bearing foundation identification and integrated the identified foundation dynamics to the FEM. However; in literature there exist limited numbers of studies that concentrate on the analytical modeling of rotor systems. For the continuous beam model of rotor systems, Lee et al. [37-39] proposed modal analysis solution based on non – self – adjoint system characteristics. Similarly, Wang and Kirkhope [40-41] proposed eigensolution and modal analysis for the undamped rotor systems and applied perturbation

analysis for damped cases. Parker and Sathe [42] proposed an exact solution for free and forced vibration of rotating disk spindle systems. In these analytical studies, rotors are considered uniform and modeled using Rayleigh beam model. However, for low slenderness ratios, shear deformation becomes important at high frequencies and Rayleigh beam model which includes rotary inertia effects but neglects shear deformation does not provide accurate results. Therefore, for accurate modeling of the system, Timoshenko beam model should be used.

Another problem in modeling of spindle – holder – tool assemblies is the multi segment characteristics of the system. For instance; in the classical eigensolution of an m -segment beam, EVP problem requires the solution of a characteristic equation expressed in terms of a $4m \times 4m$ matrix, where m is the number of segments of the rotor system which increases the size of the matrices. To overcome this complexity, Schmitz and Donaldson [7], and Erturk et al. [12] proposed receptance coupling procedure to determine end point FRFs of multi segment beams. However; their studies deal with non rotating shafts and neglect gyroscopic effects. For modeling of multi segment rotors Hong and Park [43] offers a method based on distributed transfer function synthesis (DTFS) which requires the use of Laplace transformations and construction of global matrix in the same manner as in FEM.

In addition to the modeling, there have been several experimental studies on the machine dynamics under cutting conditions. For that purpose, non-contact sensors such as Laser Doppler Vibrometer (LDV) can be used in measurement of rotating structures [44-49]. Tatara and Gren [50] used LDV to measure the response of machining centers. Similarly, Zaghbani and Songmene [51] used operational modal analysis in the determination of the dynamics of the milling machine during cutting. However, in these studies, FRFs could not be obtained due to the harmonic content of the cutting forces in milling operations. In order to overcome the harmonic content problem of the cutting forces, Opitz and Weck [52] proposed a spectral measurement method using a workpiece which

has a random surface profile. Based on the work of Opitz and Weck [52], Minis et al. [53] also used spectral measurement techniques in measuring dynamics of a lathe. In a recent study, Budak and Tunc [54], applied a new identification procedure for process damping identification. They identified process damping in low cutting speeds using chatter frequency and axial depth cut obtained through chatter tests.

1.3 Scope of Thesis

The aim of this thesis is to investigate the spindle – holder – tool assembly dynamics and to develop an analytical modeling approach for the machine tool dynamics under operational conditions. Since dynamic properties of high speed machines may vary due to gyroscopic moments, thermal expansions and centrifugal forces during cutting, tool point FRFs at the idle state of the machining center do not lead to accurate stability predictions. Therefore, developing such a method could make significant contribution to the accurate prediction of tool point FRFs, and thus to generation of stability diagrams especially for the high speed machining operations. In addition to the analytical modeling procedure, this thesis is also concentrated on the identification of the tool point FRF and bearing dynamics under operational conditions. Therefore, with the implementation of identified speed dependent bearing characteristics to the analytical model, stability of the cutting process can be predicted much more accurately.

The outcome of the thesis is believed to help increasing not only the accuracy of chatter stability predictions, but also better understanding of machine tool dynamics under operational conditions which is essential in selection of stable process conditions and machine tool design for increased productivity.

1.4 Outline of Thesis

Outline of the thesis is as follows:

In Chapter 2, theory of the proposed analytical modeling approach is presented. First, equation of motion for Timoshenko beam including gyroscopic effects is derived and eigensolution for rotating Timoshenko beam is obtained. After that, using the non self adjoint system characteristics, eigenvalue problem (EVP) of the rotating Timoshenko beam is solved for free – free end conditions and end point FRFs of a rotating Timoshenko beam is obtained. In addition to the analytical modeling of free – free beams, receptance coupling procedure for rotating multi segment beams is presented. Furthermore, bearing dynamics are included into the system by using a structural modification technique. Finally, the method proposed is verified by FEA results of a spindle – holder – tool assembly using ANSYS.

In Chapter 3, in order to investigate the variation of tool point FRF under operational conditions several analytical case studies are presented. In the case studies, gyroscopic effects and bearing stiffness variations that result in tool point FRF variations are examined for different spindle–holder–tool assemblies. In order to determine the gyroscopic effects on the tool point FRF, thus on the stability, the tool point FRF of a spindle – holder – tool assembly is calculated for various spindle speeds. In addition, effects of the bearing parameters are investigated for different spindle – holder – tool assemblies. Bearing stiffness variation effects are investigated first for relatively soft bearings and then for stiffer bearings.

In Chapter 4, various experimental identification approaches to identify the tool point FRFs during cutting operation are presented. First, tool point FRF identification is performed using the relation between actual cutting forces and response measured from the holder of the machining center. This approach is applied for cutting of a standard and specially designed workpiece separately.

Due to the harmonic content of the cutting forces and limitations in the measurement capability of dynamometers, tool point FRF is identified for limited ranges of frequency and spindle speed.

In Chapter 5, a new identification method is proposed for tool point FRF identification during cutting operations. In this identification method, experimentally determined chatter frequencies and corresponding axial depth of cuts are used for the tool point FRF identification. Using the identification method proposed, variations of the tool point FRF under cutting conditions are determined for different holder – tool combinations. In addition to identified tool point FRFs, stability diagrams are calculated using identified tool point FRFs and verified with the chatter test results.

In Chapter 6, procedure for bearing parameter identification both for idle state and rotating conditions is presented. First, bearing parameters are identified for the idle state and applying effect analysis, bearing parameters that affect the elastic mode and stability are determined. Then, using the chatter test results and the proposed analytical model, variations of the bearing stiffness values with respect to the spindle speed and cutting force are identified. Finally, actual stability of the cutting operation is calculated using analytically determined tool point FRFs.

In Chapter 7, verification of the proposed modeling approach is presented. For that purpose, experimentally identified spindle – holder interface parameters and speed dependent bearing dynamics are employed in the modeling of a different holder – tool combination. Thus tool point FRF of new assembly and stability diagrams is predicted without performing experiments. Finally performing chatter tests, it is experimentally verified that analytical modeling procedure and identification method proposed can successfully be used for predicting actual stability of the cutting operation without performing further experiments for each holder – tool combinations.

In Chapter 8, summary and conclusion of the thesis is given. Also, recommendations for future work are suggested.

CHAPTER 2

MATHEMATICAL MODELING

2.1 Modeling of the Rotating Timoshenko Beam

Consider a beam element with generalized coordinates as shown in Figure 2-1. Here u_z is the axial displacement, u_x and u_y are the lateral displacements and ϕ_x , ϕ_y , and ϕ_z are the rotations with respect to x, y and z axis, respectively.

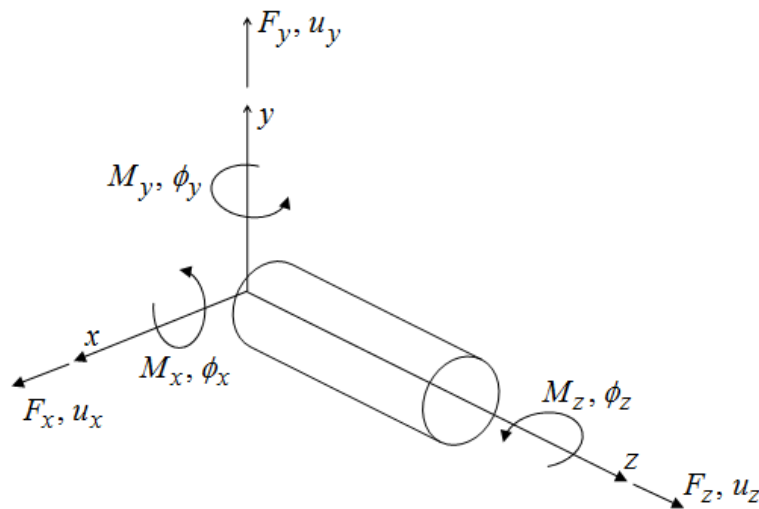


Figure 2-1 Rotating Timoshenko beam generalized coordinates

Equation of motion for a rotating Timoshenko beam can be obtained using Hamilton's principle as follows:

$$\delta \int_{t_1}^{t_2} (T - V + W) dt = 0 \quad (2.1)$$

In Equation (2.1), T and V are the kinetic and potential energies of the rotating beam, respectively. W is the work done by the external forces and moments.

Kinetic energy of the rotating Timoshenko beam element of length L can be written as follows:

$$\begin{aligned} T = & \int_0^L \frac{1}{2} \rho I \left(\left(\frac{\partial \phi_x}{\partial t} \right)^2 + \left(\frac{\partial \phi_y}{\partial t} \right)^2 \right) dz + \int_0^L \frac{1}{2} \rho A \left(\left(\frac{\partial u_x}{\partial t} \right)^2 + \left(\frac{\partial u_y}{\partial t} \right)^2 \right) dz \\ & + \int_0^L \frac{1}{2} J \rho \Omega^2 dz + 2 \int_0^L \Omega I \rho \left(\frac{\partial \phi_y}{\partial t} \right) \phi_x dz \end{aligned} \quad (2.2)$$

where ρ is the density, A is the cross sectional area, I is the area moment of inertia of the beam cross section about neutral axis, J is the polar moment of the beam about the neutral axis and Ω is the spin speed of the beam.

Also note that in Equation (2.2), first term is the kinetic energy due to the rotary inertia, second term is the translational kinetic energy and the last two terms are the kinetic energy due to the gyroscopic effects.

Potential energy of a rotating Timoshenko beam can be written as follows:

$$V = \int \frac{1}{2} E \varepsilon_{zz} dV + \int \frac{1}{2} kAG \gamma_{zx}^2 dV + \int \frac{1}{2} kAG \gamma_{yz}^2 dV \quad (2.3)$$

where E is Young's modulus, G is shear modulus and k is shear coefficient.

Displacements and strain-displacement relations can be written as follows:

$$u_z(x, y, z, t) = u'_z(z, t) + \phi_x y - \phi_y x \quad (2.4)$$

$$u_x(x, y, z, t) = u_x(z, t) \quad (2.5)$$

$$u_y(x, y, z, t) = u_y(z, t) \quad (2.6)$$

$$\varepsilon_{zz} = \frac{\partial u_z}{\partial z} = \frac{\partial u'_z}{\partial z} + \frac{\partial \phi_x}{\partial z} y - \frac{\partial \phi_y}{\partial z} x \quad (2.7)$$

$$\gamma_{zx} = \frac{\partial u_z}{\partial x} + \frac{\partial u_x}{\partial z} = -\phi_y + \frac{\partial u_x}{\partial z} \quad (2.8)$$

$$\gamma_{yz} = \frac{\partial u_y}{\partial z} + \frac{\partial u_z}{\partial y} = \phi_x + \frac{\partial u_y}{\partial z} \quad (2.9)$$

If the strain-displacement relations given by Equation(2.4)- (2.9) are substituted into the Equation(2.3), potential energy of the beam length of L can be written as follows:

$$\begin{aligned} V = & \int_0^L \frac{1}{2} EI \left[\left(\frac{\partial \phi_x}{\partial z} \right)^2 + \left(\frac{\partial \phi_y}{\partial z} \right)^2 \right] dz \\ & + \int_0^L \frac{1}{2} kAG \left[\left(\phi_x + \frac{\partial u_y}{\partial z} \right)^2 + \left(\phi_y - \frac{\partial u_x}{\partial z} \right)^2 \right] dz \\ & + \int_0^L \frac{1}{2} EA \left[\left(\frac{1}{2} \left(\frac{\partial u_x}{\partial z} \right)^2 \right)^2 + \left(\frac{1}{2} \left(\frac{\partial u_y}{\partial z} \right)^2 \right)^2 \right] dz \end{aligned} \quad (2.10)$$

If the variations of the kinetic and potential energy expressions are determined and substituted into Equation (2.1), the equation of motion can be obtained as follows:

$$\begin{aligned}
\delta \int_{t_1}^{t_2} (T - V + W) dt = & \int_{t_1}^{t_2} \int_0^L \left(\rho A \frac{\partial^2 u_x}{\partial t^2} - kAG \left(-\frac{\partial \phi_y}{\partial z} + \frac{\partial^2 u_x}{\partial z^2} \right) \right) \delta u_x \\
& + \int_{t_1}^{t_2} \int_0^L \left(\rho A \frac{\partial^2 u_y}{\partial t^2} - kAG \left(\frac{\partial \phi_x}{\partial z} + \frac{\partial^2 u_y}{\partial z^2} \right) \right) \delta u_y \\
& + \int_{t_1}^{t_2} \int_0^L \left(\rho I \frac{\partial^2 \phi_x}{\partial t^2} + 2\Omega I \rho \frac{\partial \phi_y}{\partial t} - EI \frac{\partial^2 \phi_x}{\partial z^2} + kAG \left(\phi_x + \frac{\partial u_y}{\partial z} \right) \right) \delta \phi_x dz dt \\
& + \int_{t_1}^{t_2} \int_0^L \left(\rho I \frac{\partial^2 \phi_y}{\partial t^2} - 2\Omega I \rho \frac{\partial \phi_x}{\partial t} - EI \frac{\partial^2 \phi_y}{\partial z^2} + kAG \left(\phi_y - \frac{\partial u_x}{\partial z} \right) \right) \delta \phi_y dz dt \\
& + \int_{t_1}^{t_2} \left(EI \frac{\partial \phi_x}{\partial z} \delta \phi_x \right)_{z=0}^{z=L} dt + \int_{t_1}^{t_2} \left(EI \frac{\partial \phi_y}{\partial z} \delta \phi_y \right)_{z=0}^{z=L} dt \\
& + \int_{t_1}^{t_2} \left(kAG \left(\frac{\partial u_y}{\partial z} + \phi_x \right) \delta u_y \right)_{z=0}^{z=L} + \int_{t_1}^{t_2} \left(kAG \left(\frac{\partial u_x}{\partial z} - \phi_y \right) \delta u_x \right)_{z=0}^{z=L} = 0
\end{aligned} \tag{2.11}$$

Since u_x , u_y , ϕ_x and ϕ_y are independent variables, four equations will be obtained for the equation of motion of a rotating Timoshenko beam.

$$\rho A \frac{\partial^2 u_x}{\partial t^2} - kAG \left(-\frac{\partial \phi_y}{\partial z} + \frac{\partial^2 u_x}{\partial z^2} \right) = 0 \tag{2.12}$$

$$\rho A \frac{\partial^2 u_y}{\partial t^2} - kAG \left(\frac{\partial \phi_x}{\partial z} + \frac{\partial^2 u_y}{\partial z^2} \right) = 0 \tag{2.13}$$

$$\rho I \frac{\partial^2 \phi_x}{\partial t^2} + 2\Omega I \rho \frac{\partial \phi_y}{\partial t} - EI \frac{\partial^2 \phi_x}{\partial z^2} + kAG \left(\phi_x + \frac{\partial u_y}{\partial z} \right) = 0 \tag{2.14}$$

$$\rho I \frac{\partial^2 \phi_y}{\partial t^2} - 2\Omega I \rho \frac{\partial \phi_x}{\partial t} - EI \frac{\partial^2 \phi_y}{\partial z^2} + kAG \left(\phi_y - \frac{\partial u_x}{\partial z} \right) = 0 \tag{2.15}$$

The boundary conditions of a rotating Timoshenko beam with free – free end conditions can be expressed as follows:

$$M_x(0,t) = \left(EI \frac{\partial \phi_x}{\partial z} \right)_{z=0} = 0 \quad M_y(0,t) = \left(EI \frac{\partial \phi_y}{\partial z} \right)_{z=0} = 0 \quad (2.16)$$

$$M_x(L,t) = \left(EI \frac{\partial \phi_x}{\partial z} \right)_{z=L} = 0 \quad M_y(L,t) = \left(EI \frac{\partial \phi_y}{\partial z} \right)_{z=L} = 0 \quad (2.17)$$

$$S_x(0,t) = \left(kAG \left(\frac{\partial u_y}{\partial z} + \phi_x \right) \right)_{z=0} = 0, \quad S_y(0,t) = \left(kAG \left(\frac{\partial u_x}{\partial z} - \phi_y \right) \right)_{z=0} = 0 \quad (2.18)$$

$$S_x(L,t) = \left(kAG \left(\frac{\partial u_y}{\partial z} + \phi_x \right) \right)_{z=L} = 0 \quad S_y(L,t) = \left(kAG \left(\frac{\partial u_x}{\partial z} - \phi_y \right) \right)_{z=L} = 0 \quad (2.19)$$

By eliminating the dynamic bending rotations ϕ_x and ϕ_y , the equations of motion of a rotating Timoshenko beam will take the following form

$$\begin{aligned} EI_x \frac{\partial^4 u_y}{\partial z^4} + \rho A \frac{\partial^2 u_y}{\partial t^2} - \rho I_y \left(1 + \frac{E}{kG} \right) \frac{\partial^4 u_y}{\partial z^2 \partial t^2} \\ + \frac{\rho^2 I}{kG} \frac{\partial^4 u_y}{\partial t^4} + 2\rho I_y \Omega \left(\frac{\partial^2}{\partial z^2} \left(\frac{\partial u_x}{\partial t} \right) - \frac{\rho}{kG} \frac{\partial^3 u_x}{\partial t^3} \right) = 0 \end{aligned} \quad (2.20)$$

$$\begin{aligned} EI_y \frac{\partial^4 u_x}{\partial z^4} + \rho A \frac{\partial^2 u_x}{\partial t^2} - \rho I_y \left(1 + \frac{E}{kG} \right) \frac{\partial^4 u_x}{\partial z^2 \partial t^2} \\ + \frac{\rho^2 I_y}{kG} \frac{\partial^4 u_x}{\partial t^4} - 2\rho I_y \Omega \left(\frac{\partial^2}{\partial z^2} \left(\frac{\partial u_y}{\partial t} \right) - \frac{\rho}{kG} \frac{\partial^3 u_y}{\partial t^3} \right) = 0 \end{aligned} \quad (2.21)$$

As seen from the Equation (2.20) and Equation (2.21), due to the gyroscopic effects, motion in two orthogonal planes are coupled. Thus classical solution methods cannot be applied for the solution of a rotating Timoshenko beam.

For the solution of a rotating Timoshenko beam, harmonic vibration can be assumed and separation of variables can be applied such that

$$u_x(z,t) = U_x(z)e^{i\omega t} \quad u_y(z,t) = U_y(z)e^{i\omega t} \quad (2.22)$$

$$\phi_y(z,t) = \theta_y(z)e^{i\omega t} \quad \phi_x(z,t) = \theta_x(z)e^{i\omega t} \quad (2.23)$$

Note that for the free vibration analysis of the beam element, since the element is symmetric it is known that the mode shapes of the beam in two orthogonal planes will be related with each other by the following relations [17]

$$U_x^f(z) = iU_y^f(z) \quad U_x^b(z) = -iU_y^b(z) \quad (2.24)$$

where the relations given by the Equation (2.24) correspond to the forward and backward modes respectively.

If the expression given by the Equation (2.22) - (2.24) are substituted into Equation (2.20), differential equations representing motions in two orthogonal planes can be decoupled and the equation of motion can be written as an ordinary differential equation for the backward motion as

$$EI \frac{d^4 U_y^b}{dz^4} + \left[\left(\rho I + \frac{E\rho I}{kG} \right) \omega^2 - 2\rho I \Omega \omega \right] \frac{d^2 U_y^b}{dz^2} + \left[\frac{\rho^2 I}{kG} \omega^4 - 2 \frac{\rho^2 I}{kG} \Omega \omega^3 - \rho A \omega^2 \right] U_y^b = 0 \quad (2.25)$$

Similarly, for the forward motion, decoupled equation of motion can be written as

$$EI \frac{d^4 U_y^f}{dz^4} + \left[\left(\rho I + \frac{E \rho I}{kG} \right) \omega^2 + 2 \rho I \Omega \omega \right] \frac{d^2 U_y^f}{dz^2} + \left[\frac{\rho^2 I}{kG} \omega^4 + 2 \frac{\rho^2 I}{kG} \Omega \omega^3 - \rho A \omega^2 \right] U_y^f = 0 \quad (2.26)$$

2.2 Free Vibration Solution for Rotating Timoshenko Beam

The eigensolution for rotating Timoshenko beam can be obtained by using the solution procedure given by Aristizabal-Ochoa [55] for non-rotating Timoshenko beam. For free-free end conditions, characteristic equation of rotating Timoshenko beam for backward motion can be written as

$$\begin{vmatrix} D_{11} & D_{12} \\ D_{21} & D_{22} \end{vmatrix} = D_{11} D_{22} - D_{12} D_{21} = 0 \quad (2.27)$$

where

$$D_{11} = (\alpha - \lambda) \cos(\alpha L) + (\lambda - \alpha) \cosh(\beta L) \quad (2.28)$$

$$D_{12} = (\lambda - \alpha) \sin(\alpha L) + \frac{\lambda \alpha}{\delta \beta} (\beta - \delta) \sinh(\beta L) \quad (2.29)$$

$$D_{21} = \delta \beta \frac{\lambda - \alpha}{\beta - \delta} \sinh(\beta L) - \lambda \alpha \sin(\alpha L) \quad (2.30)$$

$$D_{22} = \lambda \alpha (\cosh(\beta L) - \cos(\alpha L)) \quad (2.31)$$

$$\lambda = \frac{\alpha^2 - K}{\alpha} \quad \delta = \frac{\beta^2 + K}{\beta} \quad K = \frac{\rho A \omega^2}{kAG} \quad (2.32)$$

$$\alpha = \sqrt{\eta + \varepsilon} \quad \beta = \sqrt{-\eta + \varepsilon} \quad (2.33)$$

$$\eta = \frac{b}{2} \quad \varepsilon = \frac{\sqrt{b^2 - 4d}}{2} \quad (2.34)$$

$$b = \frac{\left[\left(\rho I + \frac{E \rho I}{kG} \right) \omega^2 - 2 \rho I \Omega \omega \right]}{EI}, \quad d = \frac{\left[\frac{\rho^2 I}{kG} \omega^4 - 2 \frac{\rho^2 I}{kG} \Omega \omega^3 - \rho A \omega^2 \right]}{EI} \quad (2.35)$$

As can be seen from Equation (2.35), rotating Timoshenko beam model has additional speed dependent terms, compared to the non-rotating case. Thus by using the characteristic equation given by Equation (2.27), natural frequencies of each elastic mode and corresponding frequency numbers α_r and β_r can be determined. Finally, the eigenfunction expressions for the dynamic transverse deflection and bending rotation can be obtained as follows:

$$U_y^b(z) = A_r (C_1 \sin(\alpha_r z) + C_2 \cos(\alpha_r z) + C_3 \sinh(\beta_r z) + C_4 \cosh(\beta_r z)) \quad (2.36)$$

$$\theta_x^b(z) = A_r \left[\lambda_r (C_1 \cos(\alpha_r z) - C_2 \sin(\alpha_r z)) \right] + A_r \left[\delta_r (C_3 \cosh(\beta_r z) + C_4 \sinh(\beta_r z)) \right] \quad (2.37)$$

where

$$C_1 = C_1, \quad C_2 = -C_1 \frac{D_{11}}{D_{12}}, \quad C_3 = C_1 \frac{\alpha_r - \lambda_r}{\delta_r - \beta_r}, \quad C_4 = -C_1 \frac{\alpha_r \lambda_r}{\delta_r \beta_r} \frac{D_{11}}{D_{12}} \quad (2.38)$$

For forward motion, the free vibration solution can be obtained in a similar way. The only difference will be in the speed dependent terms expressed by Equation (2.35). For forward motion b and d will be expressed as:

$$b = \frac{\left[\left(\rho I + \frac{E \rho I}{kG} \right) \omega^2 + 2 \rho I \Omega \omega \right]}{EI} \quad d = \frac{\left[\frac{\rho^2 I}{kG} \omega^4 + 2 \frac{\rho^2 I}{kG} \Omega \omega^3 - \rho A \omega^2 \right]}{EI} \quad (2.39)$$

Also note that the constant A_r can be obtained by the normalization of the eigenfunctions using biorthonormality condition which will be discussed in Section 2.3.

2.3 Forced Vibration Response of Rotating Timoshenko Beam

To obtain the forced response of a rotating Timoshenko beam to an external force applied on the beam at location $z = z_n$ in y direction, Equations (2.12) - (2.15) can be expressed in the following form

$$[M]\{\ddot{q}\} + [G]\{\dot{q}\} + [K]\{q\} = \{F(t)\} \quad (2.40)$$

where M , G , and K are defined as follows:

$$[M] = \begin{bmatrix} \rho A & 0 & 0 & 0 \\ 0 & \rho I & 0 & 0 \\ 0 & 0 & \rho A & 0 \\ 0 & 0 & 0 & \rho I \end{bmatrix}, \quad [G] = \begin{bmatrix} 0 & 0 & 0 & 0 \\ 0 & 0 & 0 & 2\rho I \Omega \\ 0 & 0 & 0 & 0 \\ 0 & -2\rho I \Omega & 0 & 0 \end{bmatrix} \quad (2.41)$$

$$[K] = \begin{bmatrix} -kAG \frac{\partial^2}{\partial z^2} & -kAG \frac{\partial}{\partial z} & 0 & 0 \\ kAG \frac{\partial}{\partial z} & kAG - EI \frac{\partial^2}{\partial z^2} & 0 & 0 \\ 0 & 0 & -kAG \frac{\partial^2}{\partial z^2} & -kAG \frac{\partial}{\partial z} \\ 0 & 0 & kAG \frac{\partial}{\partial z} & kAG - EI \frac{\partial^2}{\partial z^2} \end{bmatrix} \quad (2.42)$$

$$\{q\} = \begin{Bmatrix} u_y \\ \phi_x \\ u_x \\ \phi_y \end{Bmatrix} \quad \{Q(t)\} = \begin{Bmatrix} F_y(t)\delta(z-z_n) \\ 0 \\ 0 \\ 0 \end{Bmatrix} \quad (2.43)$$

Note that, due to the gyroscopic effects, the system is non – self adjoint. Therefore, in order to obtain forced response of a rotating Timoshenko beam, equation of motion should be represented in state space as

$$\begin{bmatrix} 0 & M \\ M & G \end{bmatrix} \begin{Bmatrix} \dot{w} \\ w \end{Bmatrix} = \begin{bmatrix} M & 0 \\ 0 & -K \end{bmatrix} \begin{Bmatrix} w \\ w \end{Bmatrix} + \{Q(t)\} \quad (2.44)$$

where

$$\{w\} = \begin{Bmatrix} \dot{q} \\ q \end{Bmatrix} \quad \{Q(t)\} = \begin{Bmatrix} 0 \\ \{F(t)\} \end{Bmatrix} \quad (2.45)$$

Equation (2.44) can also be written as:

$$[C] \begin{Bmatrix} \dot{w} \\ w \end{Bmatrix} = [D] \begin{Bmatrix} w \\ w \end{Bmatrix} + \{Q(t)\} \quad (2.46)$$

Note that in Equation (2.46), $[D]$ is self adjoint and $[C]$ is non – self adjoint, therefore system will have left eigenvectors and their adjoint right eigenvectors. Thus, Eigen Value Problem (EVP) of rotating Timoshenko beam for left and right eigenvectors can be written as follows:

$$\lambda_r^l [C] \{\Phi_r^l(z)\} = [D] \{\Phi_r^l(z)\}, \quad l = b, f \quad (2.47)$$

$$\bar{\lambda}_s^l [\bar{C}] \{\Psi_s^l(z)\} = [\bar{D}] \{\Psi_s^l(z)\}, \quad l = b, f \quad (2.48)$$

where

$$\{\Phi_r^l(z)\}^T = \{\hat{U}_{y_r}^l \quad \hat{\theta}_{x_r}^l \quad \hat{U}_{x_r}^l \quad \hat{\theta}_{y_r}^l \quad U_{y_r}^l \quad \theta_{x_r}^l \quad U_{x_r}^l \quad \theta_{y_r}^l\}, l = b, f \quad (2.49)$$

$$\{\Psi_s(z)\}^T = \{a\hat{U}_{y_r}^l \quad a\hat{\theta}_{x_r}^l \quad a\hat{U}_{x_r}^l \quad a\hat{\theta}_{y_r}^l \quad aU_{y_r}^l \quad a\theta_{x_r}^l \quad aU_{x_r}^l \quad a\theta_{y_r}^l\}, l = b, f \quad (2.50)$$

In Equation (2.48) bar denotes complex conjugate, and in Equations (2.49) - (2.50) superscript a denotes adjoint and superscripts b and f denote the backward and forward modes, respectively.

For non – self adjoint systems, left eigenvectors and complex conjugate of their adjoint right eigenvectors are related with a constant K_r , which is a pure imaginary number [27].

$$a\bar{\phi}_{x_r}^l = K_r \phi_{x_r}^l \quad a\bar{u}_{y_r}^l = K_r u_{y_r}^l \quad (2.51)$$

Eigenvectors can be simplified using the relation given below:

$$\hat{u}_{y_r}^l = \lambda_r^l u_{y_r}^l \quad \hat{\phi}_{x_r}^l = \lambda_r^l \phi_{x_r}^l \quad (2.52)$$

For the non self adjoint EVP, left and right eigenvectors are biorthonormal and biorthonormality can be defined using the inner product operator as

$$\langle C\Phi_r, \Psi_s \rangle = \delta_{rs} \quad \langle D\Phi_r, \Psi_s \rangle = \lambda_r \delta_{rs} \quad (2.53)$$

In Equation (2.53) $\langle \cdot, \cdot \rangle$ is the inner product operator and defined as follows:

$$\{a\} = \{a_1 \quad a_2\}^T, \quad \{b\} = \{b_1 \quad b_2\}^T \quad (2.54)$$

$$\langle a, b \rangle = \langle a_1, b_1 \rangle + \langle a_2, b_2 \rangle = \int_0^L \bar{b}_1 a_1 dz + \int_0^L \bar{b}_2 a_2 dz \quad (2.55)$$

where bar denotes complex conjugate.

To determine the forced response of the system, backward and forward modes can be treated separately. Thus if we apply the biorthonormality, the constant A_r in the eigenfunction expressions of backward and forward modes can be determined. For backward modes the constant A_r can be determined as follows:

$$A_r^2 = \frac{1}{K_r \lambda_r C_r - K_r E_r} \quad (2.56)$$

where

$$C_r = \int_0^L \left[\left(2\rho A (U_{y_r}^b)^2 \right) + \left(2\rho I (\theta_{x_r}^b)^2 \right) + \left(2\rho A (U_{x_r}^b)^2 \right) + \left(2\rho I (\theta_{y_r}^b)^2 \right) \right] dz \quad (2.57)$$

$$E_r = \int_0^L \left(i2\rho I \Omega (\theta_{x_r}^b)^2 + i2\rho I \Omega (\theta_{y_r}^b)^2 \right) dz \quad (2.58)$$

Similarly, A_r in the eigenfunction expressions of forward modes can be determined as follows:

$$A_r^2 = \frac{1}{K_r \lambda_r C_r + K_r E_r} \quad (2.59)$$

where

$$C_r = \int_0^L \left[\left(2\rho A (U_{y_r}^f)^2 \right) + \left(2\rho I (\theta_{x_r}^f)^2 \right) + \left(2\rho A (U_{x_r}^f)^2 \right) + \left(2\rho I (\theta_{y_r}^f)^2 \right) \right] dz \quad (2.60)$$

$$E_r = \int_0^L \left(i2\rho I \Omega (\theta_{x_r}^f)^2 + i2\rho I \Omega (\theta_{y_r}^f)^2 \right) dz \quad (2.61)$$

Response of the system to an externally applied excitation can be expressed by using the expansion theorem as follows:

$$w(z,t) = \sum_{l=b,f} \sum_r \Phi_r^l(z) q_r^l(t) \quad (2.62)$$

If the expression given by Equation (2.62) is substituted into Equation (2.46) and biorthonormality is applied, Equation (2.46) reduces to:

$$\dot{q}_r^l(t) = q^l(t)\lambda_r + P_r^l(t) \quad (2.63)$$

where,

$$P_r^l(t) = \left\langle \{Q(t)\}, \{\Psi_s^l\} \right\rangle = \int_0^L \{\bar{\Psi}_s^l\} \{Q(t)\} dz \quad (2.64)$$

Thus, solution in terms of modal coordinates can be obtained as:

$$q_r^l(t) = \frac{P_r^l(t)}{i\omega - \lambda_r^l} \quad (2.65)$$

Using the solution in terms of modal coordinates, given by Equation (2.65), the time response of the system to an applied excitation can be determined. For

instance, response of the system to an applied force in y direction at the location $z = z_n$ can be obtained as follows:

$$u_y(z, t) = \sum_{l=f, b} \sum_{r=-\infty}^{\infty} \frac{U_{y_r}{}^l(z) {}^a\bar{U}_{y_r}{}^l(z = z_n) F_y(t)}{i\omega - \lambda_r^l} \quad (2.66)$$

Since in the state space, the order of the EVP is doubled, eigenvalues and corresponding eigenvectors will be in the form of complex conjugates. Thus, the transverse response of the system to the applied force $F_y(t)$ can be written as follows:

$$\begin{aligned} u_y(z, t) &= \sum_{l=b, f} \sum_{r=-\infty}^{\infty} \frac{U_{y_r}{}^l(z) {}^a\bar{U}_{y_r}{}^l(z = z_n) F_y(t)}{i\omega - \lambda_r^l} \\ &= \sum_{l=b, f} \sum_{r=0}^{\infty} \left(\frac{U_{y_r}{}^l(z) {}^a\bar{U}_{y_r}{}^l(z_n) F_y(t)}{i\omega - \lambda_r^l} + \frac{\bar{U}_{y_r}{}^l(z) {}^a\bar{U}_{y_r}{}^l(z_n) F_y(t)}{i\omega - \bar{\lambda}_r^l} \right) \\ &= \sum_{l=b, f} \sum_{r=0}^{\infty} \left(\frac{2i\omega_r U_{y_r}{}^l(z) U_{y_r}{}^l(z = z_n) F_y(t)}{-\omega^2 + (\omega_r^l)^2} \right) \end{aligned} \quad (2.67)$$

For rotating Timoshenko beam, the receptance functions in y-z plane can be defined as follows:

$$H_{iy, jy} = \frac{(u_y)^j}{F_y^i}, \quad N_{iy, jx} = \frac{(\phi_x)^j}{F_y^i}, \quad L_{ix, jy} = \frac{(u_y)^j}{M_x^i}, \quad P_{ix, jx} = \frac{(\phi_x)^j}{M_x^i} \quad (2.68)$$

Note that structural damping can be included into the model by adding modal damping terms to the denominator in Equation (2.67) [17], and then point and cross receptance functions in y-z plane can be obtained as

$$H_{iy,jy}(\omega) = \sum_{l=b,f} \sum_{r=0}^{\infty} \left(2i\omega_r^l \frac{U_{y_r}{}^l(z_j)U_{y_r}{}^l(z_i)}{-\omega^2 + (\omega_r^l)^2 (1+i\gamma)} \right) \quad (2.69)$$

$$N_{iy,jx}(\omega) = \sum_{l=b,f} \sum_{r=0}^{\infty} \left(2i\omega_r^l \frac{\theta_{x_r}{}^l(z_j)U_{y_r}{}^l(z_i)}{-\omega^2 + (\omega_r^l)^2 (1+i\gamma)} \right) \quad (2.70)$$

$$L_{ix,jy}(\omega) = \sum_{l=b,f} \sum_{r=0}^{\infty} \left(2i\omega_r^l \frac{U_{y_r}{}^l(z_j)\theta_{x_r}{}^l(z_i)}{-\omega^2 + (\omega_r^l)^2 (1+i\gamma)} \right) \quad (2.71)$$

$$P_{ix,jx}(\omega) = \sum_{l=b,f} \sum_{r=0}^{\infty} \left(2i\omega_r^l \frac{\theta_{x_r}{}^l(z_j)\theta_{x_r}{}^l(z_i)}{-\omega^2 + (\omega_r^l)^2 (1+i\gamma)} \right) \quad (2.72)$$

Note that U_{y_r} and θ_{x_r} in Equations (2.69) –(2.72) are the normalized backward and forward eigenfunctions obtained using biorthonormality condition.

Since the beam has free-free end conditions, there exist two rigid body modes in each orthogonal plane where beam can translate or rotate without any elastic deformation. Thus the summation term in Equations (2.69) - (2.72) start from zero, including the rigid body mode contributions. Translational and rotational rigid body modes can be expressed as

$$U_y^{trans} = A^{trans} \quad (2.73)$$

$$U_y^{rot} = A^{rot} \left(\frac{x}{2} - L \right) \quad (2.74)$$

$$\theta_x^{trans} = 0 \quad (2.75)$$

$$\theta_x^{rot} = A^{rot} \quad (2.76)$$

Here, A^{trans} and A^{rot} are constants and by applying biorthonormality they can be determined as

$$A^{trans} = \sqrt{\frac{1}{i\omega_r C^{trans} - E^{trans}}} \quad (2.77)$$

$$A^{rot} = \sqrt{\frac{1}{i\omega_r C^{rot} - E^{rot}}} \quad (2.78)$$

where

$$C^{trans} = 4\rho AL, \quad E^{trans} = 0 \quad (2.79)$$

$$C^{rot} = \int_0^L \left[2\rho A (U_y^{rot})^2 + 2\rho A (U_x^{rot})^2 \right] dz \quad (2.80)$$

$$E^{rot} = \int_0^L \left(i2\rho I \Omega (\theta_x^{rot})^2 + i2\rho I \Omega (\theta_y^{rot})^2 \right) dz \quad (2.81)$$

Taking the rigid body terms outside the summation sign in Equations (2.69) - (2.72) and using the expressions of rigid body mode eigenfunctions given by Equations (2.73) -(2.76), point and cross receptance functions in y-z plane can be expressed as

$$H_{iy, jy}(\omega) = -\frac{1}{\rho AL \omega^2} + \sum_{l=b, f} \sum_{r=1}^{\infty} \left(2i\omega_r^l \frac{U_{y_r}^l(z_j) U_{y_r}^l(z_i)}{-\omega^2 + (\omega_r^l)^2 (1+i\gamma)} \right) \quad (2.82)$$

$$N_{iy,jx}(\omega) = \sum_{l=b,f} \sum_{r=1}^{\infty} \left(2i\omega_r^l \frac{\theta_{x_r}^l(z_j)U_{y_r}^l(z_i)}{-\omega^2 + (\omega_r^l)^2(1+i\gamma)} \right) \quad (2.83)$$

$$L_{ix,jy}(\omega) = \sum_{l=b,f} \sum_{r=1}^{\infty} \left(2i\omega_r^l \frac{U_{y_r}^l(z_j)\theta_{x_r}^l(z_i)}{-\omega^2 + (\omega_r^l)^2(1+i\gamma)} \right) \quad (2.84)$$

$$P_{ix,jx}(\omega) = \sum_{l=b,f} \sum_{r=1}^{\infty} \left(2i\omega_r^l \frac{\theta_{x_r}^l(z_j)\theta_{x_r}^l(z_i)}{-\omega^2 + (\omega_r^l)^2(1+i\gamma)} \right) \quad (2.85)$$

In addition to the point and cross FRFs in each orthogonal plane, due to the gyroscopic effects, there exist cross coupling between the orthogonal planes. Therefore; for the prediction of the complete dynamics of the rotating Timoshenko beam, cross FRFs between the orthogonal planes should be considered as well. These FRFs can be determined by using the same approach presented above, but unlike the FRFs given by Equations (2.82) -(2.85), in the FRF expressions for cross coupling terms, eigenfunctions of the two orthogonal planes will appear in equations. However; using the relations given by Equation (2.24), cross FRFs between the two orthogonal planes can be expressed by the eigenfunctions of each plane as follows:

$$H_{ix,jy}(\omega) = \sum_0^{\infty} \left(2\omega \frac{U_{y_r}^b(z_i)U_{y_r}^b(z_j)}{-\omega^2 + (\omega_r^b)^2(1+i\gamma)} \right) + \sum_0^{\infty} \left(-2\omega \frac{U_{y_r}^f(z_i)U_{y_r}^f(z_j)}{-\omega^2 + (\omega_r^f)^2(1+i\gamma)} \right) \quad (2.86)$$

$$N_{iy,jy}(\omega) = \sum_0^{\infty} \left(2\omega \frac{\theta_{x_r}^b(z_j)U_{y_r}^b(z_i)}{-\omega^2 + (\omega_r^b)^2(1+i\gamma)} \right) + \sum_0^{\infty} \left(-2\omega \frac{\theta_{x_r}^f(z_j)U_{y_r}^f(z_i)}{-\omega^2 + (\omega_r^f)^2(1+i\gamma)} \right) \quad (2.87)$$

$$L_{ix,jx}(\omega) = \sum_0^{\infty} \left(-2\omega \frac{U_{y_r}{}^b(z_j)\theta_{x_r}{}^b(z_i)}{-\omega^2 + (\omega_r{}^b)^2(1+i\gamma)} \right) + \sum_0^{\infty} \left(2\omega \frac{U_{y_r}{}^f(z_j)\theta_{x_r}{}^f(z_i)}{-\omega^2 + (\omega_r{}^f)^2(1+i\gamma)} \right) \quad (2.88)$$

$$P_{ix,jy}(\omega) = \sum_0^{\infty} \left(2\omega \frac{\theta_{x_r}{}^b(z_j)\theta_{x_r}{}^b(z_i)}{-\omega^2 + (\omega_r{}^b)^2(1+i\gamma)} \right) + \sum_0^{\infty} \left(-2\omega \frac{\theta_{x_r}{}^f(z_j)\theta_{x_r}{}^f(z_i)}{-\omega^2 + (\omega_r{}^f)^2(1+i\gamma)} \right) \quad (2.89)$$

2.4 FRFs of Multi Segment Beams by Receptance Coupling

In this study the end point FRFs of a multi segment shaft are calculated by using receptance coupling method, rather than classical approaches in which matrix sizes are increased by assembling the individual matrices.

Graphical representation of receptance coupling of two beam segments is shown in Figure 2-2.

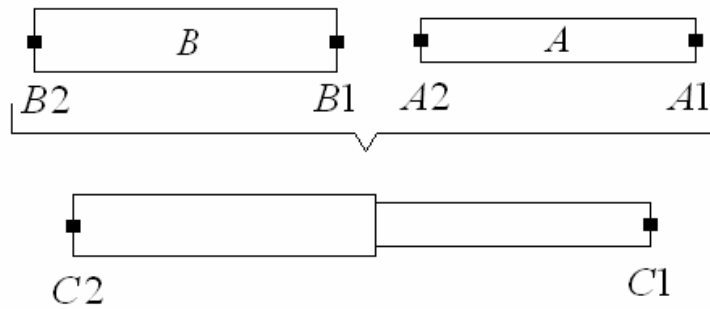


Figure 2-2 Receptance coupling of two beams.

In order to apply receptance coupling to a rotating Timoshenko beam, unlike in non – rotating case, cross FRFs between two orthogonal planes should be considered as well. Thus based on the FRF definitions given by Equation (2.68), and considering the response of the rotating Timoshenko beam at A1 end to applied force and moment excitations at the same point, receptance matrix can be defined as follows:

$$\begin{Bmatrix} u_{A1x} \\ \theta_{A1y} \\ u_{A1y} \\ \theta_{A1x} \end{Bmatrix} = \begin{bmatrix} H_{A1x,A1x} & L_{A1y,A1x} & H_{A1y,A1x} & L_{A1x,A1x} \\ N_{A1x,A1y} & P_{A1y,A1y} & N_{A1y,A1y} & P_{A1x,A1y} \\ H_{A1x,A1y} & L_{A1y,A1y} & H_{A1y,A1y} & L_{A1x,A1y} \\ N_{A1x,A1x} & P_{A1y,A1x} & N_{A1y,A1x} & P_{A1x,A1x} \end{bmatrix} \begin{Bmatrix} f_{A1x} \\ M_{A1y} \\ f_{A1y} \\ M_{A1x} \end{Bmatrix} \quad (2.90)$$

In Equation (2.90), subscripts indicate the location and direction of the excitation or response. For instance, in $H_{A1y,A1x}$ the second subscript $A1x$ indicates that the force is applied at A1 location in x-direction and the first subscript $A1y$ indicates the response considered is at A1 location in y direction.

Using the response and excitation relations given in Equation(2.90), receptance matrices for the subassemblies A and B can be written as

$$[A] = \begin{bmatrix} [A_{11}] & [A_{12}] \\ [A_{21}] & [A_{22}] \end{bmatrix} [B] = \begin{bmatrix} [B_{11}] & [B_{12}] \\ [B_{21}] & [B_{22}] \end{bmatrix} \quad (2.91)$$

where

$$[A_{11}] = \begin{bmatrix} H_{A1x,A1x} & L_{A1y,A1x} & H_{A1y,A1x} & L_{A1x,A1x} \\ N_{A1x,A1y} & P_{A1y,A1y} & N_{A1y,A1y} & P_{A1x,A1y} \\ H_{A1x,A1y} & L_{A1y,A1y} & H_{A1y,A1y} & L_{A1x,A1y} \\ N_{A1x,A1x} & P_{A1y,A1x} & N_{A1y,A1x} & P_{A1x,A1x} \end{bmatrix} \quad (2.92)$$

$$[A_{12}] = \begin{bmatrix} H_{A1x,A2x} & L_{A1y,A2x} & H_{A1y,A2x} & L_{A1x,A2x} \\ N_{A1x,A2y} & P_{A1y,A2y} & N_{A1y,A2y} & P_{A1x,A2y} \\ H_{A1x,A2y} & L_{A1y,A2y} & H_{A1y,A2y} & L_{A1x,A2y} \\ N_{A1x,A2x} & P_{A1y,A2x} & N_{A1y,A2x} & P_{A1x,A2x} \end{bmatrix} \quad (2.93)$$

$$[A_{22}] = \begin{bmatrix} H_{A2x,A2x} & L_{A2y,A2x} & H_{A2y,A2x} & L_{A2x,A2x} \\ N_{A2x,A2y} & P_{A2y,A2y} & N_{A2y,A2y} & P_{A2x,A2y} \\ H_{A2x,A2y} & L_{A2y,A2y} & H_{A2y,A2y} & L_{A2x,A2y} \\ N_{A2x,A2x} & P_{A2y,A2x} & N_{A2y,A2x} & P_{A2x,A2x} \end{bmatrix} \quad (2.94)$$

Using the compatibility and continuity conditions at the connection points of subassemblies A and B, receptance coupling procedure can be applied and FRFs of the coupled structure C can be obtained as follows:

$$[C_{11}] = [A_{11}] - [A_{12}] \left([A_{22}] + [B_{11}] \right)^{-1} [A_{21}] \quad (2.95)$$

$$[C_{12}] = [A_{12}] \left([A_{22}] + [B_{11}] \right)^{-1} [B_{12}] \quad (2.96)$$

$$[C_{11}] = [B_{21}] \left([A_{22}] + [B_{11}] \right)^{-1} [A_{21}] \quad (2.97)$$

$$[C_{22}] = [B_{22}] - [B_{21}] \left([A_{22}] + [B_{11}] \right)^{-1} [B_{12}] \quad (2.98)$$

2.5 Including Bearing Dynamics

In this study, the bearing dynamics is included into the system dynamics by using the structural modification method suggested by Özgüven [56]. In this method, the receptance matrix of a modified system is obtained from the receptance matrix of the original system and the modification matrix. Bearing

dynamics can be added to the left end of the rotor shaft as shown in Figure 2-3 and the remaining shaft segments can be coupled to the modified system with the receptance coupling procedure given in Section 2.4.

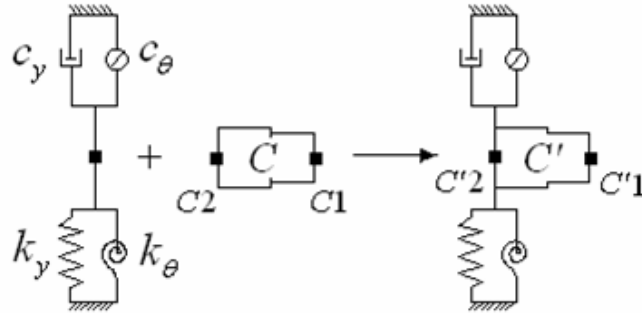


Figure 2-3 Including bearing dynamics to the rotor segment by structural modification.

In Figure 2-3 k_y is the translational stiffness, c_y is the translational damping, k_θ is the rotational stiffness and c_θ is the rotational damping of the bearing.

The receptance matrix of the unmodified system (shown in Figure 2-3 as part C), and the modification matrix representing dynamic stiffness matrix of the bearing can be written in partitioned form as follows:

$$[\alpha_C] = \begin{bmatrix} [H_{C1C1}] & [H_{C1C2}] & [L_{C1C1}] & [L_{C1C2}] \\ [H_{C2C1}] & [H_{C2C2}] & [L_{C2C1}] & [L_{C2C2}] \\ [N_{C1C1}] & [N_{C1C2}] & [P_{C1C1}] & [P_{C1C2}] \\ [N_{C2C1}] & [N_{C2C2}] & [P_{C2C1}] & [P_{C2C2}] \end{bmatrix} \quad (2.99)$$

where

$$[H_{C1C1}] = \begin{bmatrix} H_{C1x,C1x} & H_{C1y,C1x} \\ H_{C1x,C1y} & H_{C1y,C1y} \end{bmatrix} \quad (2.100)$$

and

$$[D] = \begin{bmatrix} 0 & 0 & 0 & 0 & 0 & 0 & 0 & 0 \\ 0 & 0 & 0 & 0 & 0 & 0 & 0 & 0 \\ 0 & 0 & (k_x + i\omega c_y) & 0 & 0 & 0 & 0 & 0 \\ 0 & 0 & 0 & (k_y + i\omega c_x) & 0 & 0 & 0 & 0 \\ 0 & 0 & 0 & 0 & 0 & 0 & 0 & 0 \\ 0 & 0 & 0 & 0 & 0 & 0 & 0 & 0 \\ 0 & 0 & 0 & 0 & 0 & 0 & (k_{\theta_y} + i\omega c_{\theta_y}) & 0 \\ 0 & 0 & 0 & 0 & 0 & 0 & 0 & (k_{\theta_x} + i\omega c_{\theta_x}) \end{bmatrix} \quad (2.101)$$

Then by using the structural modification method suggested by Ozguven [56], the receptance matrix of the modified system represented as C' can be obtained as

$$[\alpha_{C'}] = [[I] + [\alpha_C][D]]^{-1} [\alpha_C] \quad (2.102)$$

However, as the nonzero part of the modifying matrix is smaller than the total dof, the size of the matrix that needs to be inverted can be reduced by partitioning the matrices [56] so that

$$[\alpha_{C'}^{11}] = [[I] + [\alpha_C^{11}][D^{11}]]^{-1} [\alpha_C^{11}] \quad (2.103)$$

$$[\alpha_{C'}^{12}]^T = [\alpha_{C'}^{21}] = [\alpha_C^{21}][I] - [D^{11}][\alpha_C^{11}] \quad (2.104)$$

$$[\alpha_{C'}^{22}] = [\alpha_C^{22}] - [\alpha_C^{21}] [D^{11}] [\alpha_C^{21}] \quad (2.105)$$

where $[D^{11}]$ is the submatrix of the modification matrix, and it can be represented as:

$$[D] = \begin{bmatrix} [D^{11}] & [0] \\ [0] & [0] \end{bmatrix} \quad (2.106)$$

$$[D^{11}] = \begin{bmatrix} (k_x + i\omega c_x) & 0 & 0 & 0 \\ 0 & (k_y + i\omega c_y) & 0 & 0 \\ 0 & 0 & (k_{\theta_y} + i\omega c_{\theta_y}) & 0 \\ 0 & 0 & 0 & (k_{\theta_x} + i\omega c_{\theta_x}) \end{bmatrix} \quad (2.107)$$

Note that to be able to partition $[D]$ as given in Equation (2.106), it will be necessary to renumber the dofs.

2.6 Elastic Coupling of Subassembly Dynamics

As shown in Section 2.4, end point FRFs of subassemblies (spindle, holder and tool) can be obtained by rigidly coupling sub segments. However, in order to couple subassemblies (spindle, holder and tool), contact parameters at spindle – holder and holder – tool interfaces should be included in receptance coupling procedure as shown in Figure 2-4.

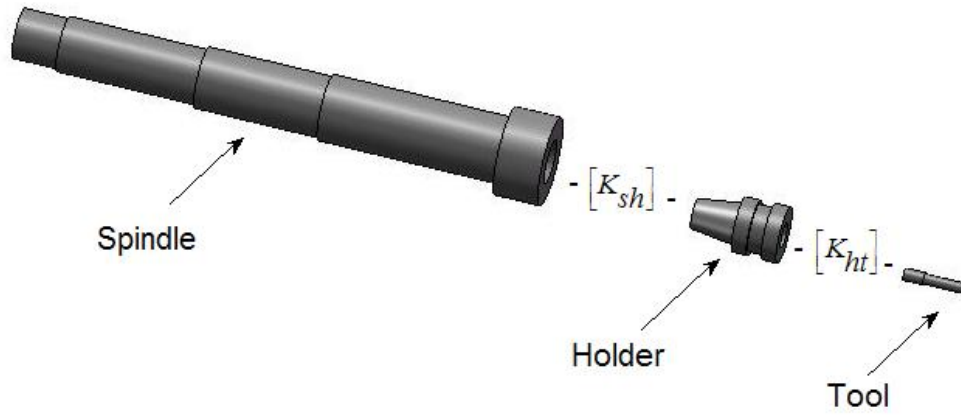


Figure 2-4 Subassemblies (Spindle, holder and tool) and contact parameters at spindle – holder and holder – tool interfaces.

For instance, end point receptances of the spindle-holder subassembly can be obtained through the elastic coupling of the spindle (S) and the holder (H) FRFs as follows [12]:

$$[SH_{11}] = [H_{11}] - [H_{12}] \left[[H_{22}] + [K_{sh}]^{-1} + [S_{11}] \right]^{-1} [H_{21}] \quad (2.108)$$

$$[SH_{12}] = [H_{12}] \left[[H_{22}] + [K_{sh}]^{-1} + [S_{11}] \right]^{-1} [S_{12}] \quad (2.109)$$

$$[SH_{21}] = [S_{21}] \left[[H_{22}] + [K_{sh}]^{-1} + [S_{11}] \right]^{-1} [H_{21}] \quad (2.110)$$

$$[SH_{22}] = [S_{22}] - [S_{21}] \left[[H_{22}] + [K_{sh}]^{-1} + [S_{11}] \right]^{-1} [S_{12}] \quad (2.111)$$

where SH represents spindle – holder assembly and $[K_{sh}]$ is complex stiffness matrix at spindle – holder interface and it can be represented as:

$$[K_{sh}] = \begin{bmatrix} k_x^{sh} + i\omega c_x^{sh} & 0 & 0 & 0 \\ 0 & k_{\theta_y}^{sh} + i\omega c_{\theta_y}^{sh} & 0 & 0 \\ 0 & 0 & k_y^{sh} + i\omega c_y^{sh} & 0 \\ 0 & 0 & 0 & k_{\theta_x}^{sh} + i\omega c_{\theta_x}^{sh} \end{bmatrix} \quad (2.112)$$

Similarly, the point receptance matrix of the assembly at the tool tip is obtained as follows:

$$[SHT_{11}] = [T_{11}] - [T_{12}] \left[[T_{22}] + [K_{ht}]^{-1} + [SH_{11}] \right]^{-1} [T_{21}] \quad (2.113)$$

where SHT represents spindle – holder - tool assembly and $[K_{ht}]$ is complex stiffness matrix at holder - tool interface.

2.7 Numerical Case Studies

In this section a numerical case study is presented to verify the analytical model and the solution approach, as well as to demonstrate the effect of including gyroscopic moments on machine tool dynamics.

2.7.1 Verification of the Model

First, in order to verify the accuracy and computational efficiency of the proposed analytical modeling approach, a multi segment spindle – holder – tool assembly with asymmetric bearings (Figure 2-5) is modeled and analyzed with ANSYS, as well as with the proposed approach. For the ANSYS model, beam element BEAM 188 which is based on Timoshenko beam theory is used for the rotor segments, and asymmetric front and rear bearings are modeled using COMBIN 214 element. Frequency increment in the FRF calculation is selected as 0.5 Hz in both ANSYS and in the analytical modeling approach.

Bearing properties are given in Table 2-1 and geometry of the spindle, holder and tool are given in Table 2-2 - Table 2-4, respectively. Material properties of the assembly are taken as follows; mass density $\rho=7860 \text{ kg/m}^3$, Young's modulus $E=200 \text{ GPa}$, Poisson's ratio $\nu=0.3$ and structural damping ratio $\gamma = 0.06$. In Figure 2-5, superscripts f and r correspond to the front and rear bearings, respectively.

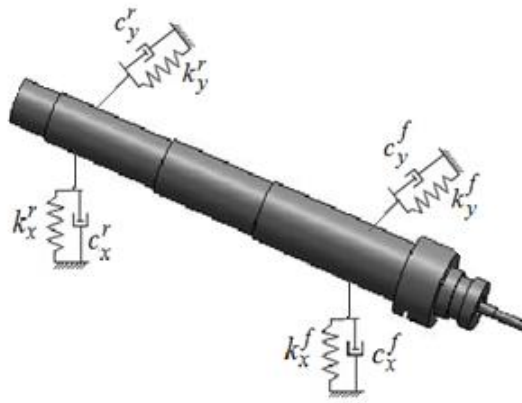


Figure 2-5 Multi-segment rotor (spindle – holder – tool assembly) supported by asymmetric bearings.

Table 2-1 Front and rear bearing properties.

	Front Bearing	Rear Bearing
k_x (N/m)	5.5×10^7	5.5×10^7
k_y (N/m)	7.5×10^7	7.5×10^7
c_x (N.s/m)	10	10
c_y (N.s/m)	10	10

Table 2-2 Spindle dimensions.

Segment number	1	2	3	4	5	6	7	8	9	10
Length (mm)	25	115	57	13	20	230	30	33	57.5	6.5
Outer Diameter (mm)	65	100	120	110	100	90	70	60	55	50

Table 2-3 Holder dimensions

Segment number	1	2
Length (mm)	25	110
Outer Diameter (mm)	70	55

Table 2-4 Tool dimensions

Segment number	1	2
Length (mm)	45	55
Outer Diameter (mm)	18	22
Inner Diameter (mm)	0	0

In order to check the accuracy of the proposed analytical model, end point FRFs of the assembly are calculated for the x-z and y-z planes with both ANSYS and the proposed model for 40 000 rpm spindle speed. In addition to the point FRFs, the cross FRFs of the assembly between two orthogonal planes are also calculated. The results are given in Figure 2-6 to Figure 2-8.

As seen from Figure 2-6 to Figure 2-8, the analytical model proposed predicts the dynamics of the system accurately. The maximum frequency difference

between the resonance frequencies calculated with ANSYS and the analytical model developed occurs in the sixth mode, and the difference is only 0.9 %. For the remaining modes in the frequency range of interest, differences are less than 0.1%. In addition to its high accuracy, the proposed analytical approach is computationally very efficient as well. The time required for ANSYS solution is 1500 seconds whereas using the proposed analytical model the end point FRF of the same assembly can be determined in 102 seconds.

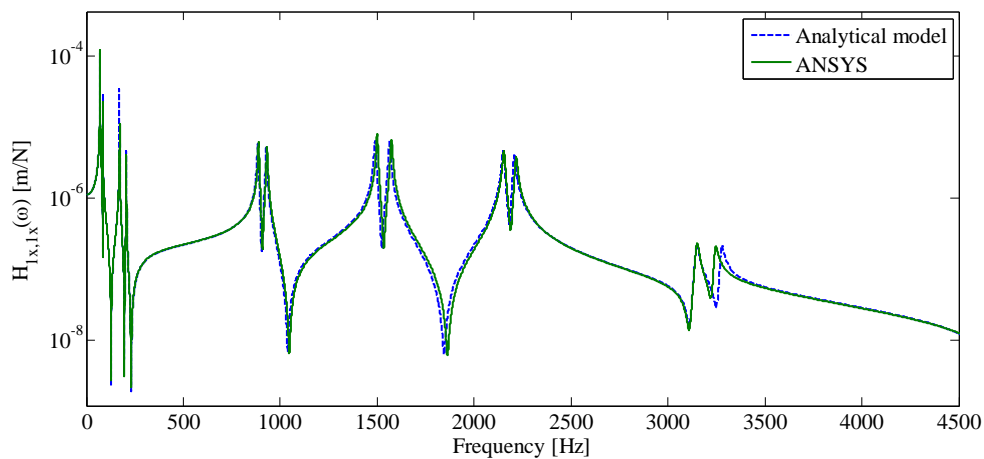


Figure 2-6 Tool point FRF in the x-z plane calculated using ANSYS and the analytical model.

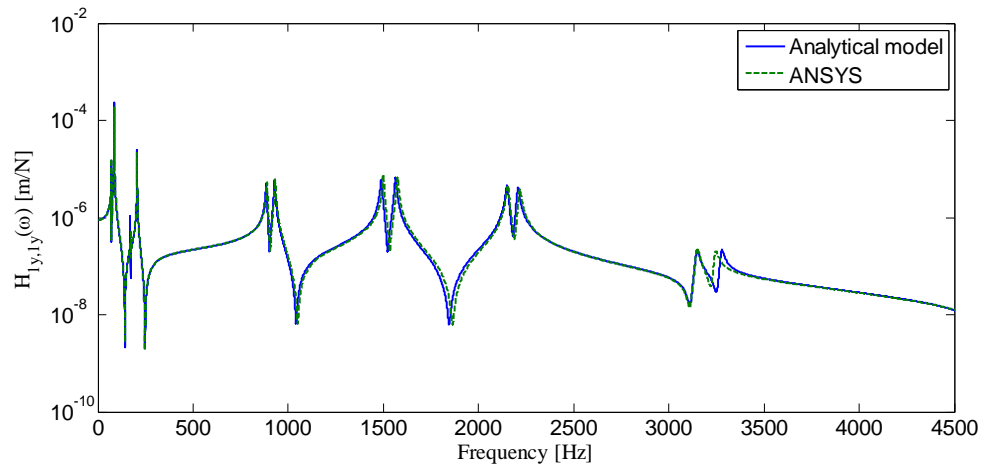


Figure 2-7 Tool point FRF in the y-z plane calculated using ANSYS and analytical model.

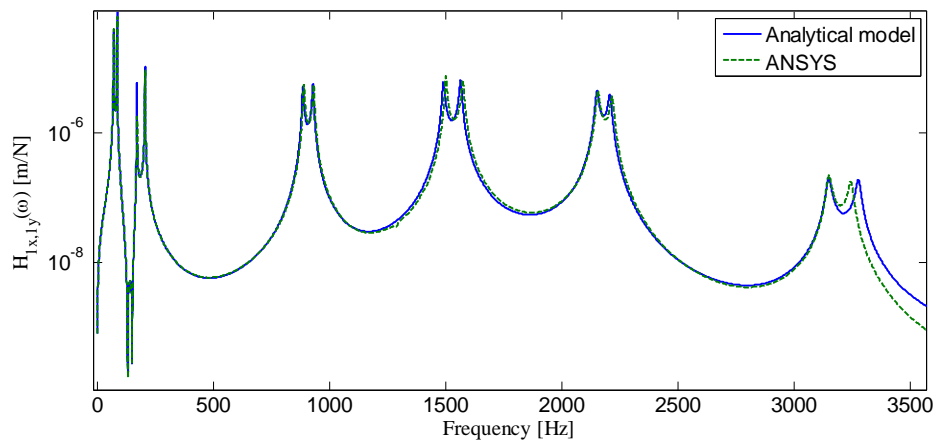


Figure 2-8 Cross FRFs between the two orthogonal planes obtained with ANSYS and analytical model.

In addition to FRFs given in Figure 2-6 to Figure 2-8, in order to investigate the changes in tool point FRF under rotating conditions, tool point FRF of the same spindle – holder – tool assembly is calculated at idle state. The tool point FRF given in Figure 2-6 is compared with the tool point FRF at 40000 rpm spindle speed in Figure 2-9. As seen from Figure 2-9, gyroscopic moments cause separation of idle modes into backward and forward modes.

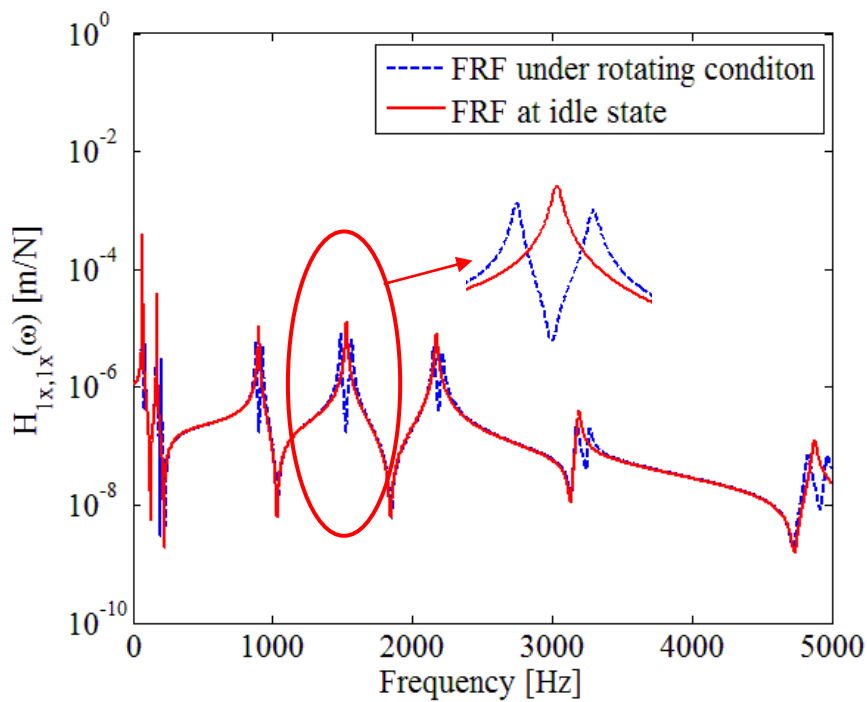


Figure 2-9 Tool point FRF in the x-z plane calculated by the analytical model for the idle state and for 40000 rpm spindle speed

2.7.2 Computational Efficiency of the Method

In this section the computational efficiency of the proposed approach is demonstrated for the case study considered. In engineering applications where modifications exist, FEM should be reconstructed and the dynamics of the whole system should be analyzed for each case. However, in the proposed approach, receptances of the unmodified part of system can be stored and the system dynamics can be determined by analyzing the modified part of the system only. For example, in machine tool applications, the spindle remains the same in the analyses but different tool holders and cutting tools are clamped to the spindle for different cutting operation. In order to demonstrate the advantage of the proposed approach, the same case study is used and the spindle – holder – tool assembly given in Table 2-2 - Table 2-3 is reanalyzed by using a different tool whose properties are given in Table 2-5. Tool point FRFs are calculated both with ANSYS and the proposed analytical model. Note that in the analytical model, only the receptances of the tool segments are recalculated and these receptances are coupled with the previously determined spindle – holder subassembly receptances. Therefore; while the determination of the modified system dynamics with ANSYS takes 1500 seconds, proposed method requires only 21 seconds for the computation of the end point FRFs of the modified system.

Table 2-5 Tool dimensions

Segment number	1	2
Length (mm)	40	57
Outer Diameter (mm)	10	12
Inner Diameter (mm)	0	0

CHAPTER 3

EFFECT ANALYSIS OF GYROSCOPIC MOMENTS AND SPEED DEPENDENT BEARING STIFFNESS VARIATIONS ON TOOL POINT FRF AND STABILITY

In this section, several cases are presented in order to investigate the variation of tool point FRF under operational conditions. In the case studies, two main effects that result in tool point FRF variations are examined for different spindle–holder–tool assemblies. First, variations of tool point FRF due to gyroscopic effects are examined. Second, effects of bearing stiffness variation due to rotation of the system on the tool point FRFs are investigated. Finally, combined effects of gyroscopic moments and bearing stiffness variations on the tool point FRFs are examined. In addition to the tool point FRFs, variations of stability diagrams are also investigated for the case studies.

3.1 Case Study 1

In order to investigate the effects of gyroscopic moments, spindle–holder–tool assembly is first modeled for non-rotating case and then for spindle speed of 25000 rpm. Geometry of the spindle, holder and tool are given in Table 3-1 to Table 3-3 respectively. Dynamic properties of the interface and bearings are also given in

Table 3-4. Material properties of the spindle–holder–tool assembly are taken as: Mass density $\rho = 7860 \text{ kg/m}^3$, Young's modulus $E = 200 \text{ GPa}$, Poisson's ratio $\nu = 0.3$ and material loss factor is assumed to be $\gamma = 0.003$.

For the interface parameters at the spindle – holder and holder – tool connection, identified parameters given in the study of Ertürk et.al [12] are

used. Also for the bearing properties, numerical values given in the reference [12] are used.

Table 3-1 Spindle dimensions for case study 1

Segment number	1	2	3	4	5	6	7	8	9	10
Length (mm)	26	26	26	38	100	66	75	30	40	40
Outer Diameter (mm)	66	66	66	66	76	70	62	58	58	58
Inner Diameter (mm)	54	48	40	32	32	32	32	32	32	32

Table 3-2 Tool Dimensions for case study 1

Segment number	1	2
Length (mm)	45	55
Outer Diameter (mm)	18	22
Inner Diameter (mm)	0	0

Table 3-3 Holder Dimensions for case study 1

Segment number	1	2	3	4	5	6
Length (mm)	22	129	24	26	26	26
Outer Diameter (mm)	72	60	70	54	48	40
Inner Diameter (mm)	16	16	16	16	16	16

Table 3-4 Dynamic properties of the bearings and interfaces for case study 1

	Translational Stiffness (N/m)	Rotational Stiffness (N.m/rad)	Translational Damping (N.s/m)	Rotational Damping (N.m.s/rad)
Spindle – holder interface	5×10^7	1.5×10^6	10	-
Holder – tool interface	2×10^7	1.5×10^6	10	-
Front Bearing	7.5×10^5	-	10	-
Rear Bearings	2.5×10^6	-	10	-

In order to study the effects of gyroscopic moment on the tool point FRF of the spindle – holder – tool assembly, tool point FRF is calculated at 25 000 rpm spindle speed and also at idle conditions. The results are shown in Figure 3-1.

As seen from Figure 3-1, gyroscopic effects cause separation of idle modes into backward and forward modes as expected, and the amount of separation between backward and forward modes increases with spindle speed. Also note that, in order to investigate only the effects of the gyroscopic moments, for the rotating case bearing properties are not updated according to the spindle speed but they are used as given in

Table 3-4. Thus the only reason for the differences between the FRFs given in Figure 3-1 will be the gyroscopic effects.

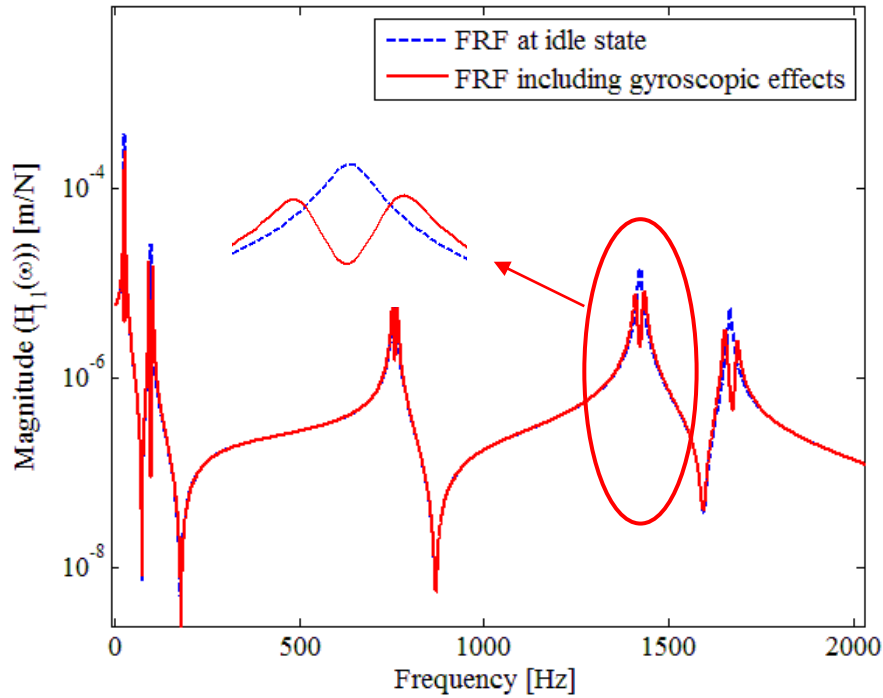


Figure 3-1 Comparison of the tool point FRFs calculated by using the analytical model for the idle state and for 25000 rpm spindle speed.

Although the effect of gyroscopic moment on frequency response may not be much, its further effects may be more important in stability analysis. In order to investigate the effects of gyroscopic moments on stability of the cutting process, stability limits of the cutting process are calculated using FRFs in operating and idle conditions by using the analytical milling chatter stability model proposed by Budak and Altintas [5]. During the stability calculation workpiece is taken as an aluminum alloy, and the radial depth of cut is taken as 3 mm. The cutting force coefficients are taken as $K_t=625$ MPa and $K_r=100$ MPa [24].

The effect of gyroscopic moments on the stability diagram is shown in Figure 3-2 which demonstrates that rotational effects may increase stability limits of the cutting operation so that an unstable point on the diagram may actually be stable.

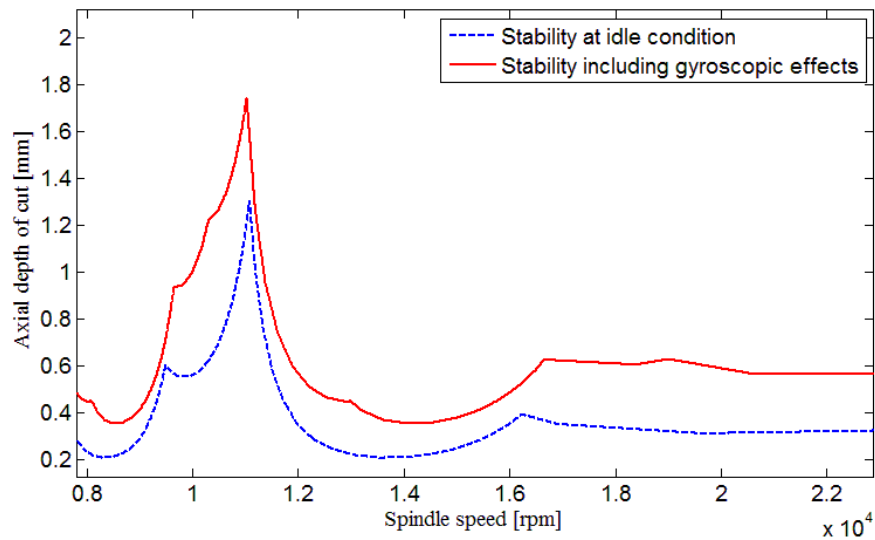


Figure 3-2 Stability diagrams predicted using the tool tip FRFs for the idle state and 25 000 rpm spindle speed.

Note that stability diagram given in Figure 3-2 is for 25000 rpm spindle speed. The tool point FRFs are also calculated for spindle speeds 9000 rpm, 15000 rpm and 35000 rpm and corresponding stability limits are determined. The change in the stability limits for different spindle speeds are tabulated in Table 3-5.

Table 3-5 Variations in the stability limits for different spindle speeds

Spindle Speed [rpm]	Maximum axial depth of cut using (mm)		Difference (%)
	Using FRFs at idle state	Using FRFs for rotating spindle	
9000	0.27	0.3	10
15000	0.23	0.3	23
25000	0.27	0.46	41
35000	0.2	0.38	47

As can be seen from Table 3-5, if gyroscopic moment is not considered and FRFs of the idle state were used, the stability limits predicted would be significantly underpredicted.

During high rotational speeds, centrifugal forces and gyroscopic forces act on the balls of the bearings pressing the balls toward the outer race. This effect causes changes in the contact angles and kinematics of the balls as well as redistributing the contact loads in the bearing which leads to decreased stiffness [18]. Thermal expansions may also cause variations in the contact conditions, and thus affect dynamic properties of the bearings. Thus, in addition to the gyroscopic effects on the spindle–holder–tool assembly dynamics, bearing stiffness variation due to rotational speed should be considered for accurate prediction of the tool point FRF.

In order to investigate the effects of bearing stiffness variation due to rotational speed on tool point FRF thus, on stability, tool point FRF is calculated for the idle state with the bearing parameters given in Table 3-4. In addition to the idle FRF, tool point FRF is computed for 25000 rpm spindle speed with the bearing stiffness values updated according to rotational speed as given in Table 3-6.

Bearing stiffness values are updated based on the study of Altintas and Cao [21]. Obtained tool point FRFs are given in Figure 3-3.

Table 3-6 Updated bearing parameters for case study 1

	Translational Stiffness (N/m)	Rotational Stiffness (N.m/rad)	Translational Damping (N.s/m)	Rotational Damping (N.m.s/rad)
Front Bearing	4.5×10^5	-	10	10
Rear Bearing	1.5×10^6	-	10	10

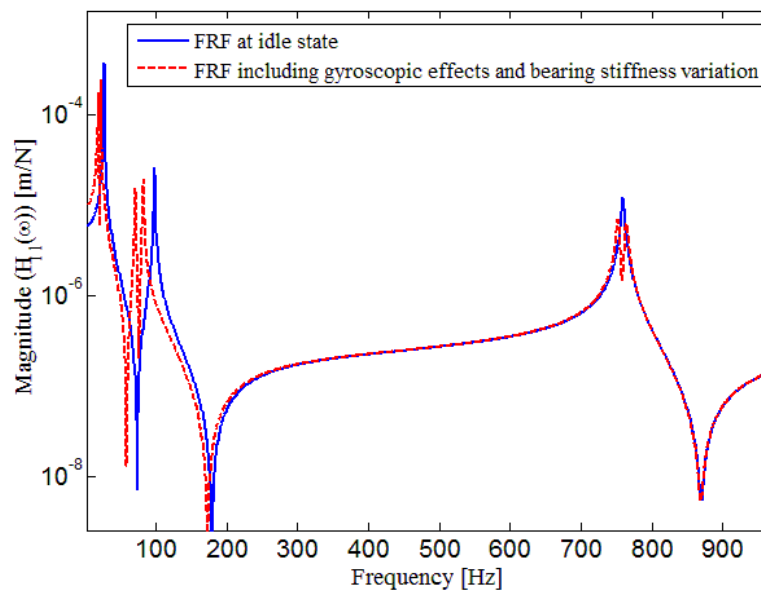


Figure 3-3 Tool point FRF calculated by the analytical model for the idle state and for 25000 rpm spindle speed rotating condition.

As seen from Figure 3-3, the variation of the bearing properties causes significant changes in the spindle rigid body modes. On the contrary, tool modes are not affected by the bearing stiffness variations as expected.

Similar to the gyroscopic moment effect analysis, to demonstrate the effects of the bearing stiffness variations due to rotational speed on chatter stability, stability diagrams are generated using the FRFs given in Figure 3-1 and Figure 3-3 with the same cutting parameters. Obtained stability diagrams are given in Figure 3-4.

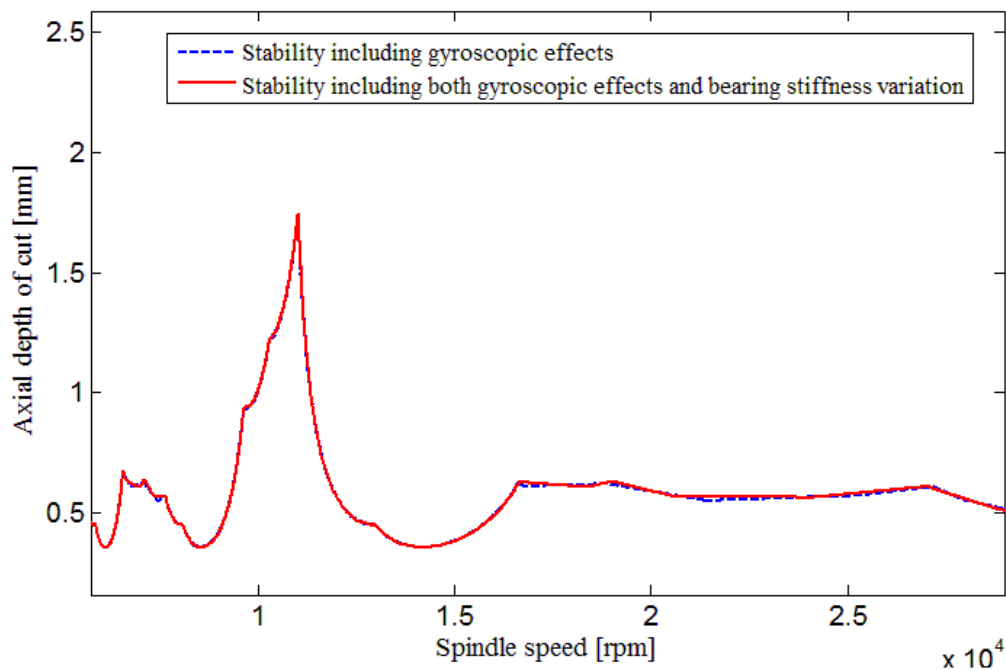


Figure 3-4 Stability diagrams predicted using the tool tip FRFs for 25 000 rpm spindle speed with and without bearing stiffness variation effect.

As seen from Figure 3-4, even with a considerable change in the tool point FRF, stability diagrams are not affected. This is due to the dominant characteristics of the tool modes since the stability is governed by the dominant tool mode in this case. Thus deviations between the actual stability of the process and stability predicted using idle FRF are due to the gyroscopic moments. Consequently, it can be said that the changes in bearing stiffness properties due to rotational speed do not affect stability diagram for the case studied.

3.2 Case Study 2

It is a well known phenomenon that stiffness characteristics of bearings are highly depend on the preload applied, and with increasing preload bearing stiffness values increase. Also Erturk et al. [14] showed that for the highly stiff bearings, variations in the bearing stiffness values affect the elastic modes in tool point FRF. Therefore; spindle – holder – tool assembly given in Table 3-1 - Table 3-3 is modeled for 25000 rpm spindle speed and idle state. Unlike previous case, tool point FRF of the spindle–holder–tool assembly is obtained with stiffer bearings. For the stiffer bearing case, bearing stiffness values are taken as given in Table 3-7 for the front and rear bearings. Also note that the order of the magnitude of the bearing stiffness values is kept at 10^6 N/m.

Calculated tool point FRFs for idle state and at rotating conditions are shown in Figure 3-5. Also note that, during the calculation of tool point FRFs given in Figure 3-5, the same bearing parameters are used. Thus variations between these FRFs can be attributed to the gyroscopic effects only.

Table 3-7 Dynamic properties of the bearings at the idle state

	Translational Stiffness (N/m)	Rotational Stiffness (N.m/rad)	Translational Damping (N.s/m)	Rotational Damping (N.m.s/rad)
Front Bearings	5.5×10^6	-	100	10
Rear Bearings	5.5×10^6	-	100	10

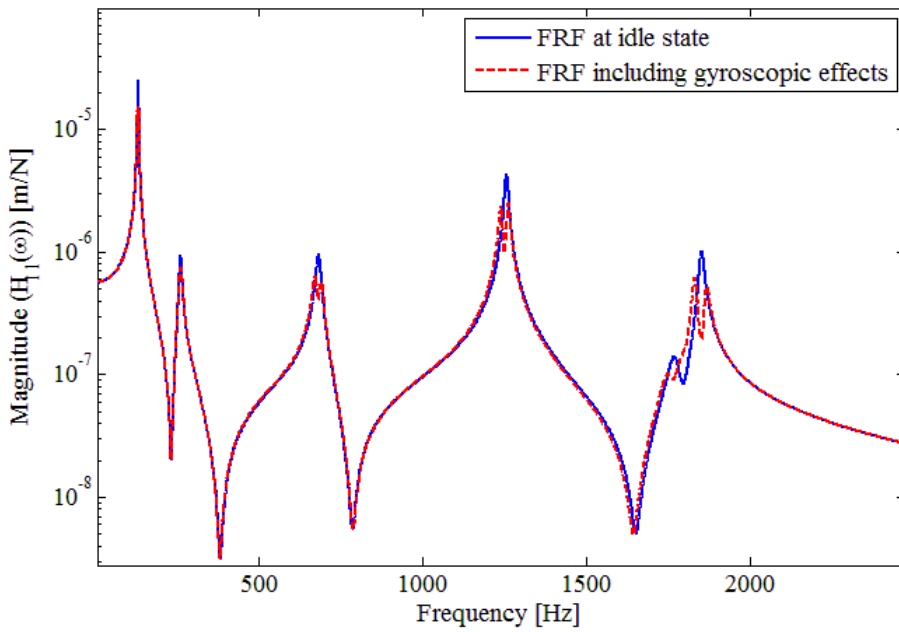


Figure 3-5 Tool point FRF calculated by the analytical model for the idle state and for 25000 rpm spindle speed rotating condition.

As seen from Figure 3-5, gyroscopic effects cause separation of the modes similar to the previous case. In addition to the tool point FRF variation, to investigate the effects of gyroscopic moments on the stability of the cutting process, stability limits of the cutting process are calculated using FRFs in operating and idle conditions. The stability calculation is made for a workpiece made of aluminum alloy, and radial depth of cut of 3 mm is used. The cutting force coefficients are taken as $K_t=625$ MPa and $K_r=100$ MPa [6]. Calculated stability diagrams are given in Figure 3-6.

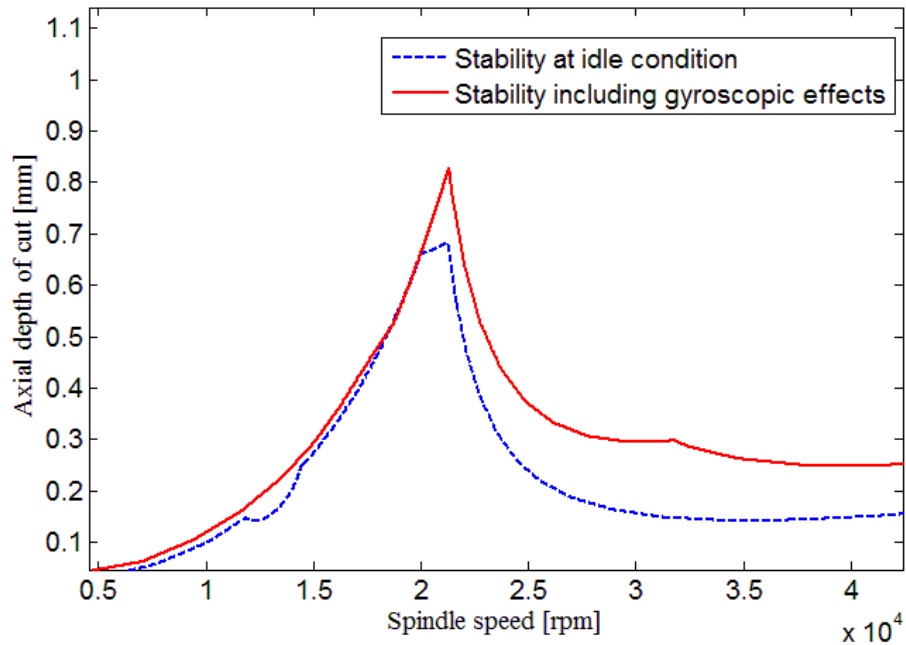


Figure 3-6 Stability diagrams predicted using the tool tip FRFs for idle state and 25 000 rpm spindle speed without bearing stiffness variation effect.

As seen from Figure 3-6, similar to case 1, gyroscopic effects cause increase in stability limits of the cutting process and it should be kept in mind that stability diagram given in Figure 3-6 is calculated using tool point FRF for 25000 rpm spindle speed. Thus, stability diagram given in Figure 3-6 is valid for cutting operation at 25000 rpm spindle speed. For higher spindle speeds, tool point FRF thus stability limit should be recalculated for the corresponding spindle speed. As shown in previous case, with the increasing spindle speed, deviations in the stability limit will be much more.

In addition to gyroscopic effects, in order to investigate the effect of bearing stiffness variations due to rotational speed on stability of the cutting process, tool point FRF of the spindle – holder – tool assembly is calculated for idle and rotating conditions. For the idle condition, tool point FRF is calculated with the bearing parameters given in Table 3-7 and for the rotating conditions, tool point FRF is calculated for 25000 rpm spindle speed with the bearing properties updated according to rotational speed as given in Table 3-8. Obtained tool point FRFs are given in Figure 3-7.

Table 3-8 Updated bearing parameters according to rotational speed

	Translational Stiffness (N/m)	Rotational Stiffness (N.m/rad)	Translational Damping (N.s/m)	Rotational Damping (N.m.s/rad)
Front Bearings	2.5×10^6	-	100	10
Rear Bearings	2.5×10^6	-	100	10

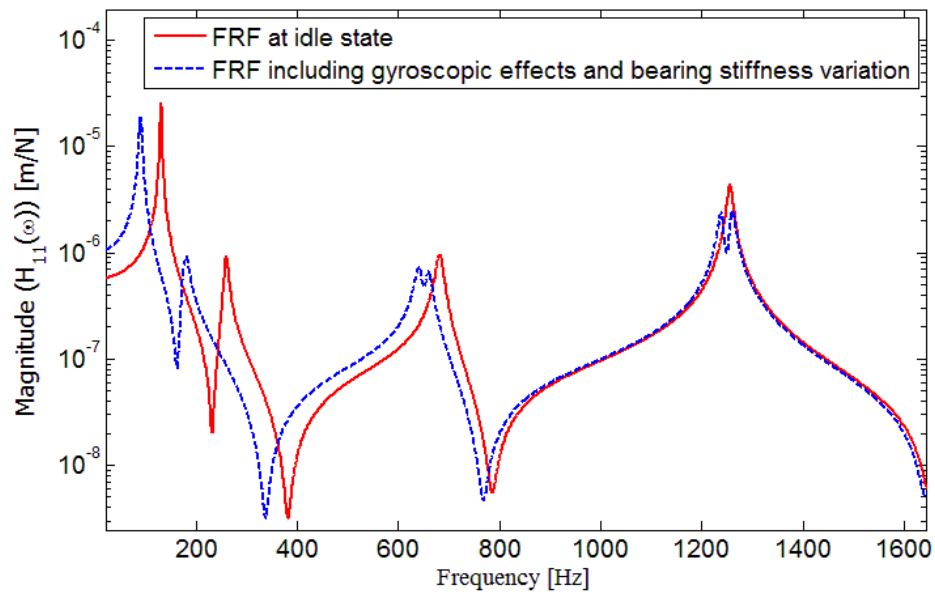


Figure 3-7 Tool point FRF calculated by the analytical model for the idle state and for 25000 rpm spindle speed rotating condition with bearing stiffness variation.

As seen from Figure 3-7, variation of the bearing stiffness affects the spindle rigid body modes and spindle elastic mode simultaneously. Also tool mode located at 1300 Hz does not affected by the bearing stiffness variation.

Finally, to demonstrate the effects of bearing stiffness variations due to rotational speed on chatter stability prediction, stability diagrams are generated for idle and rotating conditions with the same cutting parameters used in the previous case. Obtained stability diagrams are given in Figure 3-8. Note that to demonstrate the effect of gyroscopic moments and bearing stiffness variations due to rotational speed on stability, stability diagram is determined for two different rotating conditions as given in Figure 3-8. For the first rotating condition, only the gyroscopic effects are included and bearing parameters are not updated according to rotational speed. In the second rotating condition,

both gyroscopic effects and bearing stiffness variation due to rotational speed are included in tool point FRF calculation.

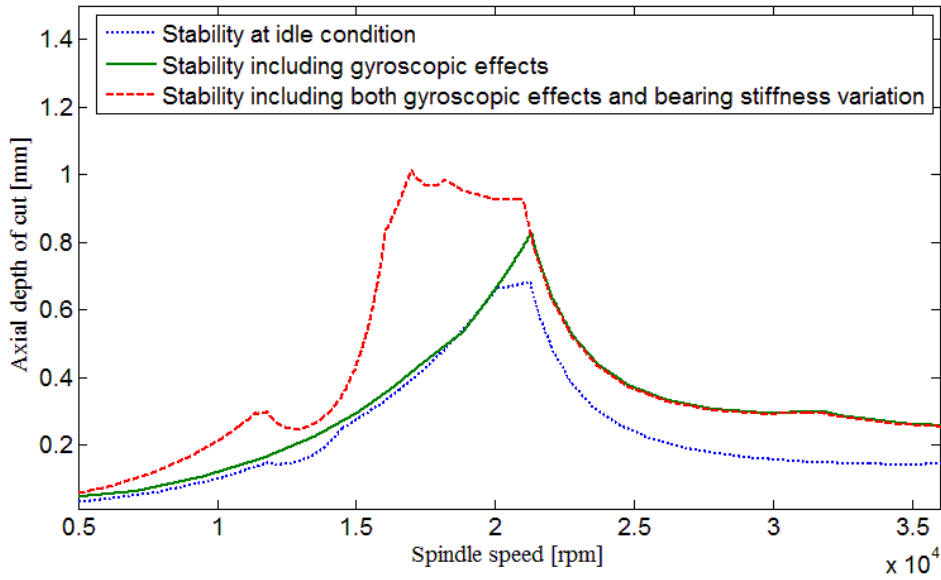


Figure 3-8 Stability diagrams predicted using the tool tip FRFs for idle state and for 25 000 rpm spindle speed with and without bearing stiffness variation effect.

As seen from Figure 3-8, compared to gyroscopic effects, bearing stiffness variation causes considerable change on stability diagrams. Especially, in stability lobe, deviations due to the bearing stiffness variations become crucial. Thus, it can be concluded that based on the tool mode dominant characteristics and bearing dynamics, bearing stiffness variation may cause considerable variations on the stability of the process.

3.3 Case Study 3

In case study 1 and case study 2, effects of the gyroscopic moments and bearing stiffness variations are examined. In these case studies, bearing stiffness values are taken in the order of magnitude of $10^5 - 10^6$ N/m based on the study of Erturk et al. [14] and in case study 2, it is shown that when stiffer bearings are used, in addition to the spindle rigid body modes, spindle elastic modes are also affected by stiffness variations of bearings which will lead to considerable variations in the stability diagrams of the cutting operation. In the work of Altintas Cao [21], speed dependent bearing characteristics are presented and in these studies, bearing stiffness values are given in the order of magnitude of 10^8 N/m. Thus, in this case study, effects of the rotating conditions on stability diagrams are examined for spindle – holder – tool assembly with much more stiff bearings given in literature. For that purpose, tool point FRF is determined for idle and 15000 rpm spindle speed conditions. The spindle and holder given in previous cases are used. The clamped tool dimensions are given in Table 3-9. Bearing parameters used for the idle and rotating cases are given in Table 3-10 and Table 3-11, respectively. The calculated tool point FRFs are shown in Figure 3-9.

Table 3-9 Tool dimensions for case study 3

Segment number	1	2
Length (mm)	40	25
Outer Diameter (mm)	12	14
Inner Diameter (mm)	0	0

Note that to demonstrate the effects of the gyroscopic moments and bearing stiffness variations separately, two different rotating tool point FRFs are given in Figure 3-9. In the first rotating tool point FRF only the gyroscopic moments are included and bearing stiffness values are not updated according to the rotational speed. In obtaining the second rotating tool point FRF, both gyroscopic effects and bearing stiffness variations are considered.

Table 3-10 Dynamic properties of the bearings at the idle state for case study 3

	Translational Stiffness (N/m)	Rotational Stiffness (N.m/rad)	Translational Damping (N.s/m)	Rotational Damping (N.m.s/rad)
Front Bearings	2×10^8	-	100	10
Rear Bearings	2×10^8	-	100	10

Table 3-11 Updated bearing parameters according to rotational speed for case study 3

	Translational Stiffness (N/m)	Rotational Stiffness (N.m/rad)	Translational Damping (N.s/m)	Rotational Damping (N.m.s/rad)
Front Bearing	0.5×10^8	-	100	10
Rear Bearings	0.5×10^8	-	100	10

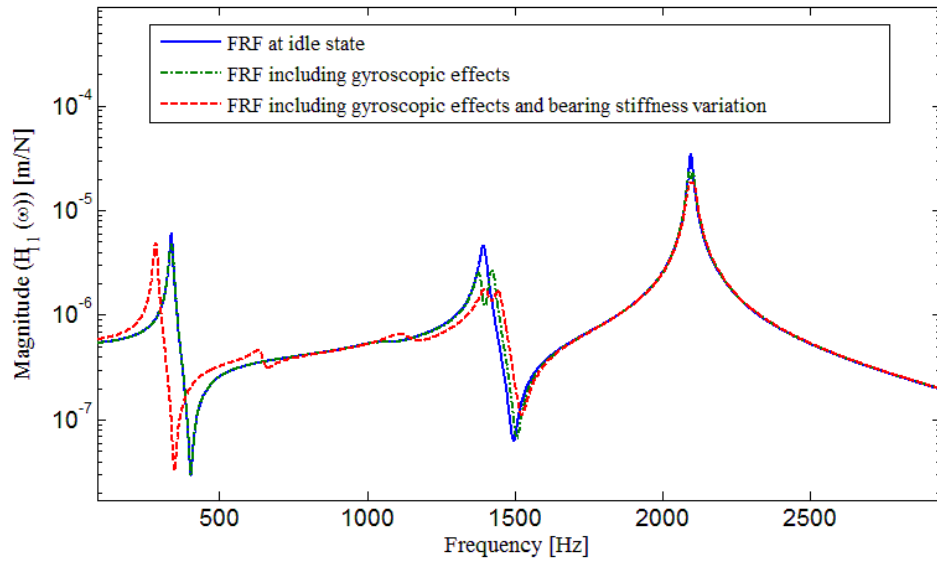


Figure 3-9 Tool point FRF calculated by the analytical model for the idle state and for 15000 rpm spindle speed rotating condition with and without bearing stiffness variation.

As seen from Figure 3-9, similar to the case study 2, gyroscopic effects cause separation of the modes, and variation of the bearing stiffness values causes variation on the elastic modes. Tool mode located at 2100 Hz is not affected by the bearing stiffness variation.

Finally, to demonstrate the effects of the bearing stiffness variations due to rotational speed on chatter stability prediction, stability diagrams are generated for idle and rotating conditions for the machining of an aluminum alloy workpiece with 3 mm radial depth of cut. The cutting force coefficients are taken as $K_t=625$ MPa and $K_r=100$ MPa. Obtained stability diagrams are given in Figure 3-10.

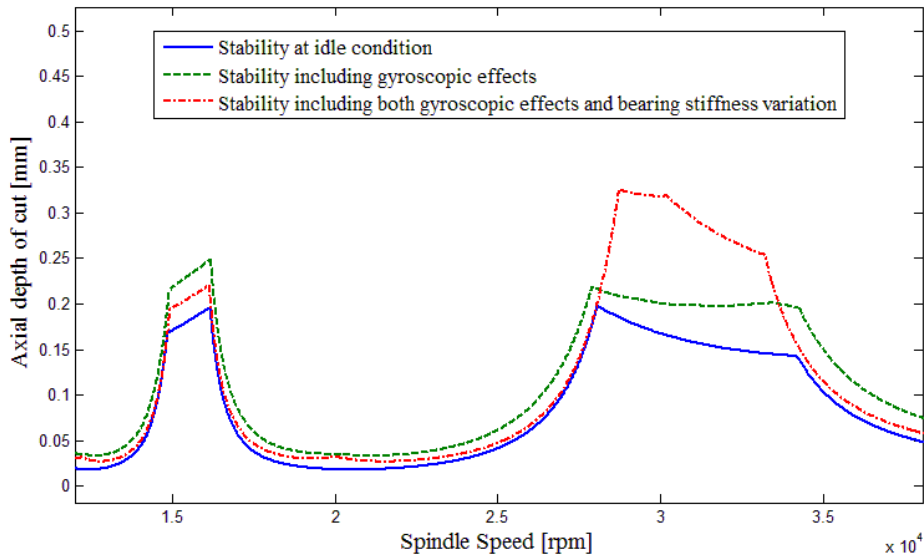


Figure 3-10 Stability diagrams predicted using the tool tip FRFs for idle state and for 15 000 rpm spindle speed with and without bearing stiffness variation effect.

As seen from Figure 3-10, similar to the results given in Figure 3-8, compared to the gyroscopic effects, bearing stiffness variation causes considerable change in stability diagrams. Thus, it can be concluded that idle FRFs may cause under prediction of the stability.

3.4 Case Study 4

In addition to the results given in Section 3.3, to examine cases where the tool mode is dominant and spindle is supported on stiff bearings as given in Table 3-10, tool overhang length is increased as shown in Table 3-12. Similar to the previous case studies, tool point FRF is calculated for idle state and for 15000 rpm spindle speed with and without bearing stiffness variation. For the idle and

rotating conditions bearing parameters given Table 3-10 and Table 3-11 are used respectively. Obtained tool point FRFs are given in Figure 3-11.

Table 3-12 Tool Dimensions for case study 4

Segment number	1	2
Length (mm)	40	55
Outer Diameter (mm)	12	14
Inner Diameter (mm)	0	0

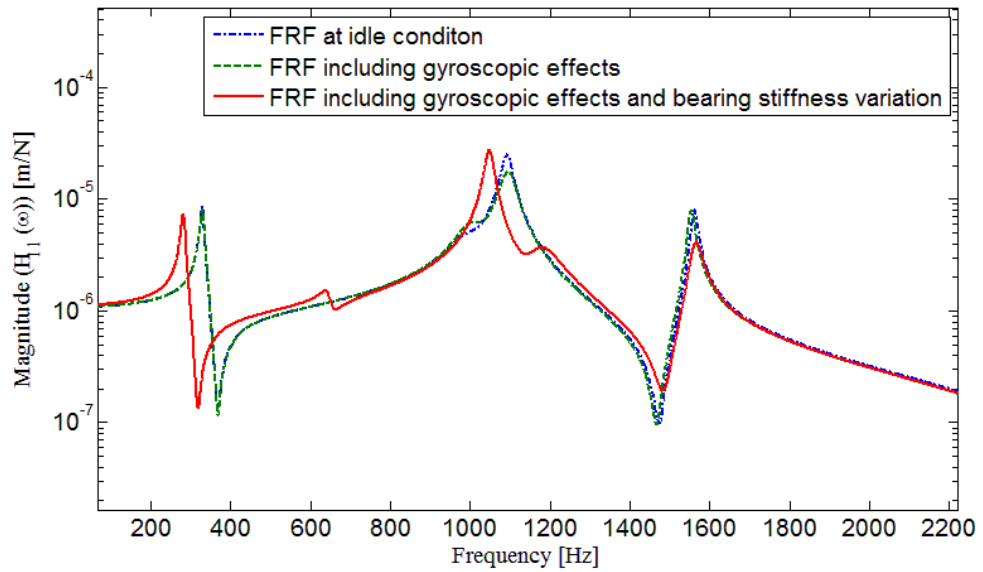


Figure 3-11 Tool point FRF calculated by the analytical model for the idle state and for 15000 rpm spindle speed rotating condition with and without bearing stiffness variation.

As seen from Figure 3-11, for 15000 rpm spindle speed there exist slight change in the tool point FRF due to the gyroscopic effects. However; due to bearing stiffness variations, unlike previous cases, tool mode is also affected. Finally, in order to investigate the effect of the gyroscopic moments and bearing stiffness variations on stability, stability diagrams are calculated using the same cutting conditions used in the previous case studies. Calculated stability diagrams are given in Figure 3-12.

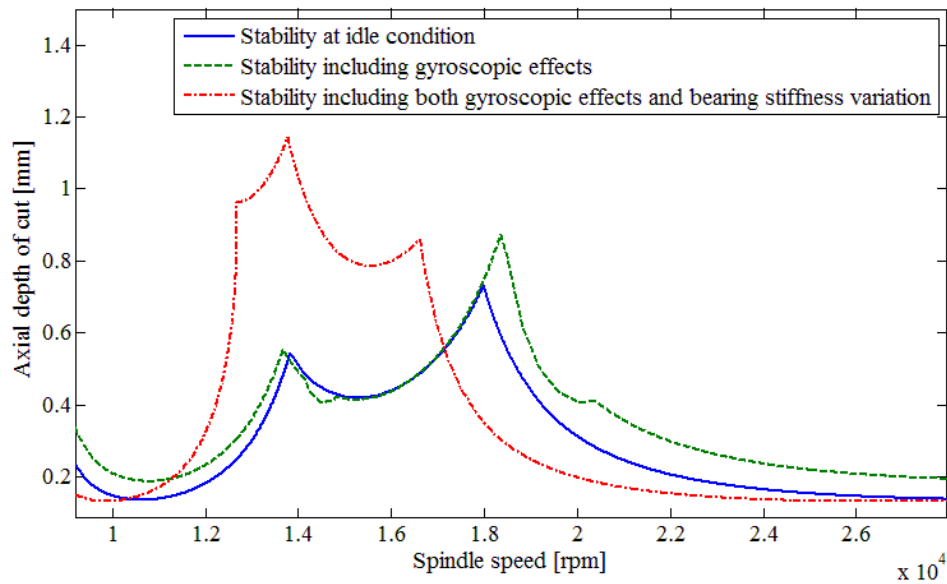


Figure 3-12 Stability diagrams predicted using the tool tip FRFs for idle state and for 15 000 rpm spindle speed with and without bearing stiffness variation effect.

As seen from Figure 3-12, unlike previous cases, stability lobe is shifted to the left due to the bearing stiffness variations so that an unstable point on the diagram obtained using idle FRF is actually stable and on the contrary stable point is actually unstable.

In this chapter using the analytical model proposed, variations of tool point FRF under operational conditions are studied for different spindle – holder – tool assemblies. In the case studies, two main effects that result in tool point FRF variations are examined. First, dynamic variations of the assembly due to the gyroscopic effects are investigated. Second, the effects of bearing stiffness variation due to rotational speed on the tool point FRFs thus on stability diagrams are investigated. It is observed that gyroscopic moments cause separation of each mode in tool point FRF into backward and forward modes. It is also observed that this separation causes increase in stability limit of the cutting operation for relatively high spindle speeds. Case studies showed that effect of bearing stiffness variations on tool point FRF depends on bearing stiffness characteristics and relative stiffness of the tool with respect to whole assembly. As shown in case study 1, when relatively soft bearings are used in the machining center, bearing stiffness variations have negligible effect on tool point FRF. However; for stiffer bearing case, variations of the bearing stiffness values affect first elastic mode of the spindle which might lead to considerable deviations in stability of the cutting operations depending on the relative stiffness of the tool with respect to spindle. In case studies, it is observed that when tool point FRF is dominated by tool mode, bearing stiffness variations do not affect tool point FRF, and therefore the stability of the cutting operation is not affected by bearing stiffness variations. On the contrary, when relatively thick tool is clamped to machining center and stability is determined by spindle modes, bearing stiffness variations cause considerable deviations in stability diagrams.

CHAPTER 4

EXPERIMENTAL IDENTIFICATION OF THE TOOL POINT FRF

The approach proposed in this chapter aims to determine in process system FRF using the relation between cutting forces that excite the system and response of the system measured simultaneously during cutting operation. For that purpose two different strategies are applied. First, identification is performed for conventional cutting operation. Then, identification is performed for the machining of a specially designed workpiece.

4.1 Spectral Density Measurement

In dynamic systems, system FRF can be obtained by the input-output relationship. In literature there exist different types of estimators which are suitable for different types of systems and conditions [57] – [59]. In real life applications, determination of the system FRF is highly dependent on the accurate estimation of the noise exist in the measurement of input and output signals. For instance, for the system given in Figure 4-1, $x(t)$ and $y(t)$ are the input and output signals, respectively. $x_m(t)$ and $y_m(t)$ are the measured input and output signals of the system, respectively, and $n_x(t)$ and $n_y(t)$ represent the noises in the measured signals.

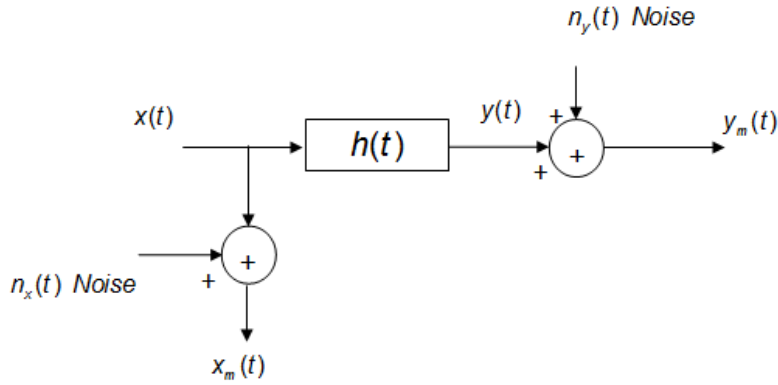


Figure 4-1 The effects of the measurement noise on both input and output.

In order to determine the system FRF, noise levels in the input and output signals should be examined carefully. In cases where there exist noise only in the output signal, H_1 estimator gives accurate estimates of the system FRF where H_1 can be represented as follows [59]:

$$H_1(f) = \frac{S_{x_m y_m}(f)}{S_{x_m x_m}(f)} \quad (4.1)$$

In Equation (4.1), $S_{x_m y_m}$ is the cross power spectrum between input and output signals and $S_{x_m x_m}$ is the power spectral density function of the input signal. Also note that, since there does not exist noise in the input signal measurement, $x_m(t) = x(t)$.

Also, when there exist noise only in the input signal measurement, system FRF can be obtained by the estimator given as follows:

$$H_2(f) = \frac{S_{y_m y_m}(f)}{S_{y_m x_m}(f)} \quad (4.2)$$

Note that, since there does not exist noise in the output signal measurement, $y_m(t) = y(t)$.

Finally, when there exist noises both in the input and the output signal measurements as shown in Fig. 1, system FRF can be determined by the estimator H_3 defined as follows [59]:

$$H_3(f) = \frac{S_{y_m y_m}(f) - \kappa(f) S_{x_m x_m}(f)}{2S_{y_m x_m}(f)} + \frac{\sqrt{\left[S_{x_m x_m}(f) \kappa(f) - S_{y_m y_m}(f) \right]^2 + 4 \left| S_{x_m y_m}(f) \right|^2 \kappa(f)}}{2S_{y_m x_m}(f)} \quad (4.3)$$

where $\kappa(f)$ is the ratio of the spectra of the measurement noises in the input and output signals, as defined below

$$\kappa(f) = \frac{n_x(f)}{n_y(f)} \quad (4.4)$$

In real applications, it is difficult to determine the noise ratio of the input and output signals. In such cases, it can be assumed that the ratio of the spectra of the measurement noises is unity ($\kappa(f) = 1$) [59].

In system identification, in addition to the correct estimator choice, another important criterion is the consistency of the input and output signals. In cases where there are additional inputs to the system that cannot be estimated or when there is a nonlinear relation between the input and output signals, applied FRF estimators will not give correct results. At that point, coherence function between the input and output signals can provide valuable information about the accuracy of the identification process. For a linear time invariant system coherence function between input and output signals can be defined as follows:

$$\gamma_{xy}^2 = \frac{|S_{xy}(f)|^2}{S_{xx}(f)S_{yy}(f)} \quad (4.5)$$

where $S_{xy}(f)$ is the cross power spectrum between input and output signal. Similarly, S_{xx} and S_{yy} are power spectral density functions of the input and output signals, respectively. Generally, coherence functions greater than 0.75 can be taken as acceptable in the system identification processes.

4.2 Mass Loading Effect of Accelerometers on Tool Point FRF

In machine tool studies accelerometers are commonly used to obtain tool point FRFs experimentally. Although mass of a typical accelerometer used in these measurements is extremely small compared with the spindle and the cutting tool, it can have a significant effect on the FRF measurement [60,61]. As given in study of Orkun et al. [60,61], even a 2.5 gram accelerometer may cause considerable variations on tool point FRF. Mass loading effect of accelerometers can be eliminated by using non contact measurement devices. In addition, mass loading effects of accelerometers can be compensated using structural modification techniques.

When tool point FRF of a spindle – holder – tool assembly is obtained using accelerometer, mass loading effect can be compensated and tool point FRF can be obtained accurately as follows [60,61]:

$$\left[SHT_{11}^m \right] = \left[[I] + \left[SHT_{11}^{um} \right] \times [D] \right]^{-1} \times \left[\left[SHT_{11}^{um} \right] \right] \quad (4.6)$$

where, $[I]$ is the identity matrix, $[D]$ is the modification matrix and superscript m refer to the modified and um refer to unmodified properties of the system.

Since modification requires only mass of the accelerometer, the modification matrix is given by

$$[D] = (-\omega^2 M) \quad (4.7)$$

where M is mass of the accelerometer and ω is the excitation frequency.

Using the modification matrix given in Equation (4.7), Equation (4.6) will take the form

$$SHT_{11}^m = \frac{SHT_{11}^{um}}{1 + SHT_{11}^{um} \times (-\omega^2 M)} \quad (4.8)$$

Using the modification method, the mass effect of the accelerometer can be eliminated from the FRFs measured with accelerometer, and accurate tool point FRFs can be obtained as studied in detail in [60,61].

4.3 Standard Cutting

In order to determine the system dynamics during machining, the response of the system to cutting forces can be used. For this purpose, cutting forces can be measured and used as an input to the system and the response of the system to them can be measured using a laser sensor, and finally the system FRF can be obtained by using the input-output relation between cutting forces and vibration measurements.

In order to identify variations of machining center dynamics under operational conditions, a 25 mm diameter end mill with 50 mm overhang length and 1-tooth is clamped to machining center. Since spindle part of the milling machine used in the experiments (a 5-axis high speed DMG Evo 50 machining center) is placed inside a casing, response measurements are taken from the rotating

holder part. First, the milling machine is excited at the tool tip by an instrumented impact hammer and the response of the system is measured at the tool holder with a laser vibrometer for the idle state of the spindle. Obtained cross FRF (G_{12}) is given in Figure 4-2. Here, subscript 1 represents the response point which is on the holder, and subscript 2 represents the excitation point which is the tool tip.

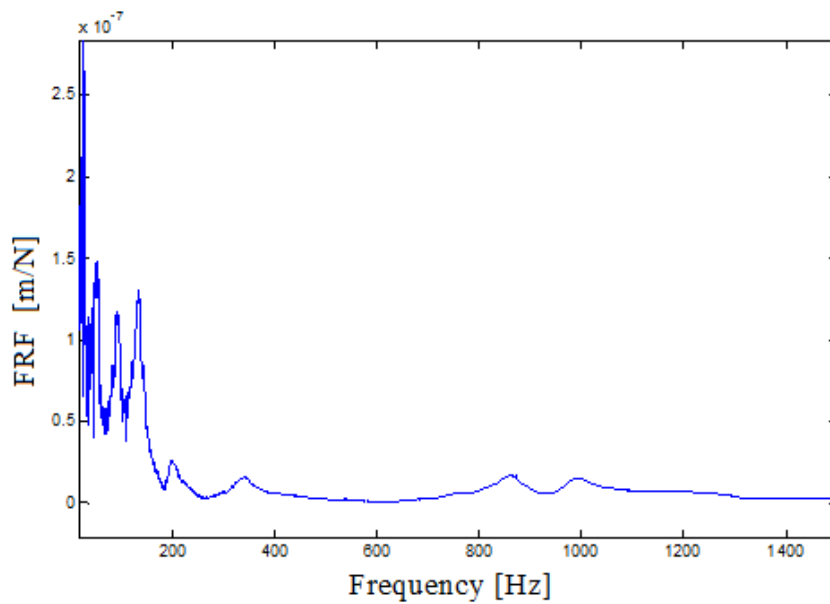


Figure 4-2 Tool point–holder cross FRF (G_{12}).

In order to obtain tool point – holder cross FRF during machining operation, cutting operation was performed on an aluminum alloy in down milling mode using 1 mm axial depth of cut, 12.5 mm radial immersion and 2025 rpm spindle speed. During the cutting operation, cutting forces are measured with a Kistler table type dynamometer which is directly attached to the workpiece and the response of the system is measured at the holder by using a laser

vibrometer. Frequency spectrum of the measured cutting force in the x-direction and frequency spectrum of the laser vibrometer measurement are given in Figure 4-3 and Figure 4-4, respectively.

As seen from Figure 4-3 and Figure 4-4, main problem in this approach is the harmonic characteristics of the cutting forces. Since the cutting forces excite the system mainly at the tooth passing frequency and at its higher harmonics, system responds to the cutting force excitation at the same frequencies. For example, for the cutting operation with 1 tooth and 2025 rpm spindle speed, tooth passing frequency is 33.75 Hz and its higher harmonics are 67 Hz, 101 Hz and 134 Hz. Therefore, it is not possible to obtain FRF of the system in a certain frequency band. Instead, specific points of the FRF for the given cutting operation are obtained.

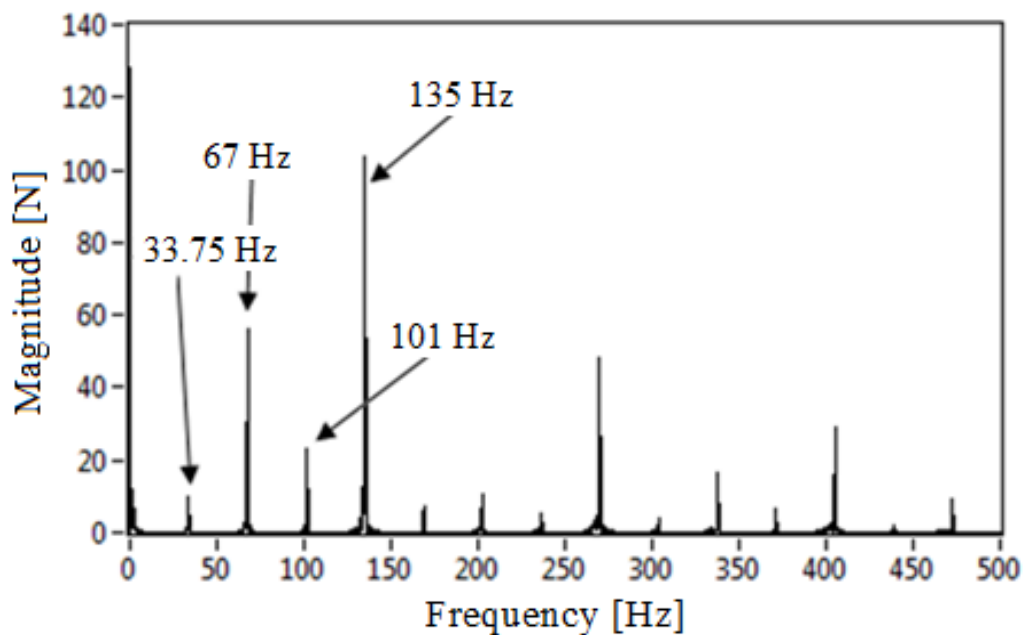


Figure 4-3 Spectrum of the cutting force in the x-direction with respect to the spindle axis.

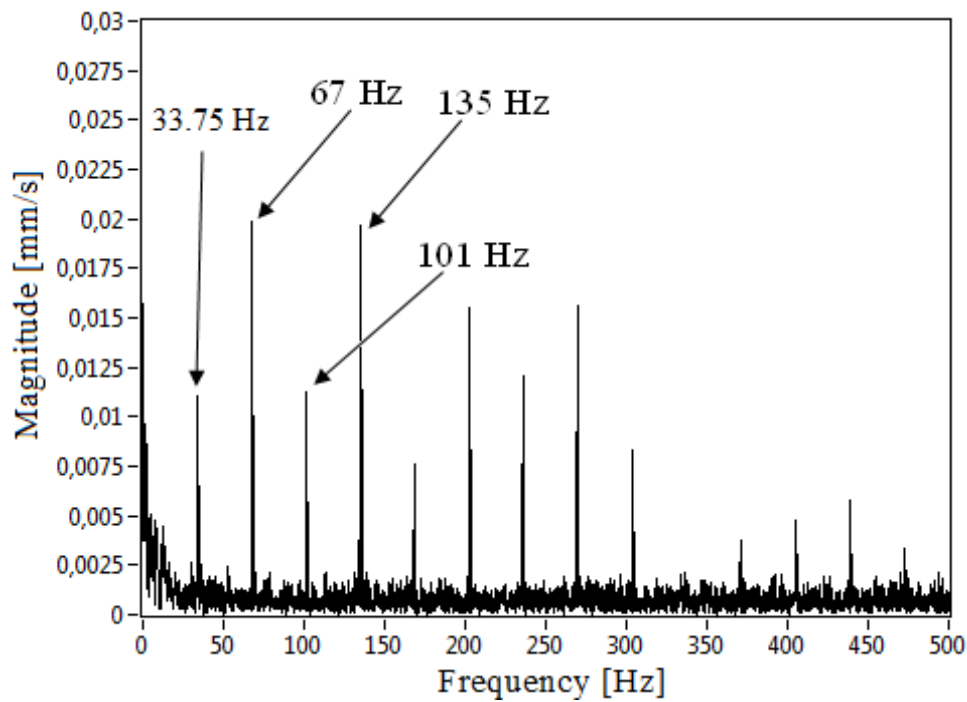


Figure 4-4 Frequency spectrum of the laser vibrometer measurement.

In order to overcome harmonic content problem of the cutting operation and obtain FRF for each frequency in the interested band, it is assumed that the system dynamics is not affected significantly from the relatively small spindle speed variations. Based on this assumption, the system is excited around each mode using the pre-determined spindle speeds. For example, the required spindle speeds in order to excite the spindle modes located at 91Hz and 134 Hz are given in Table 4-1 for the tool having 4 cutting edges.

As seen from Table 4-1, system can be excited in the frequency band of 85 Hz – 145 Hz by changing spindle speeds. Also note that to be able to excite the spindle effectively, relatively large radial and axial depth of cuts are chosen for the cutting operations.

Table 4-1 Spindle speeds and corresponding tooth passing frequencies for the tool with 4 cutting edges

Radial immersion (%)	Spindle speed (rpm)	Tooth passing frequency (Hz)
30	1275	85
30	1305	87
30	1350	90
30	1380	92
30	1425	95
30	1455	97
30	1575	105
30	1650	110
30	1875	125
30	1905	127
30	1950	130
30	1980	132
30	2025	135
30	2055	137
30	2100	140
30	2175	145

In addition to spindle speeds given in Table 4-1, system can be excited at the same frequencies with higher spindle speeds by changing the number of cutting edges of the tool. For that purpose, pre-determined spindle speeds and corresponding tooth passing frequencies for end mill with 1 cutting edge are given in Table 4-2.

Table 4-2 Spindle speeds and corresponding tooth passing frequencies for the tool with 1 cutting edge

Radial immersion (%)	Spindle speed (rpm)	Tooth passing frequency (Hz)
30	5100	85
30	5400	90
30	5700	95
30	6000	100
30	6600	110
30	7500	125
30	7200	120
30	7620	127
30	7800	130
30	8100	135
30	8220	137
30	8400	140

In order to determine the tool point – holder cross FRF, cutting tests were performed on a 5 – axis machining center using spindle speeds given in Table 4-1 and Table 4-2 where a 25 mm diameter end mill with 50 mm overhang was attached to the holder. Cutting was performed using 1 mm axial depth of cut, 30% radial immersion, where feed was chosen as 0.25 mm/revolution. During the cutting operation, cutting forces were measured with a Kistler table type dynamometer which is directly attached to the workpiece and the response of the system was measured by a laser vibrometer at the holder. Measurement points on the milling machine are shown in Figure 4-5 where point 1 and 2 represent the response and force measurement points, respectively.

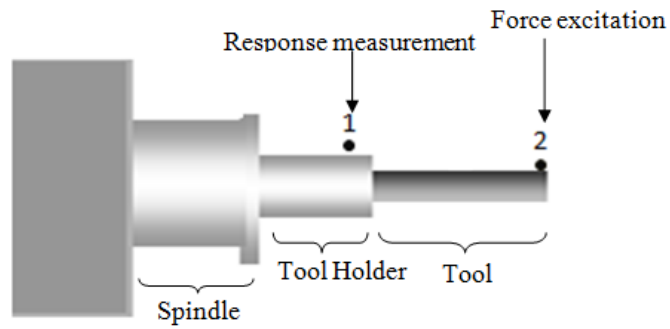


Figure 4-5 Measurement locations for the cutting forces and response on the machining center.

Assuming that the system dynamics is not affected significantly by relatively small spindle speed variations, as mentioned earlier, force and response measurements FRFs given in Figure 4-6 can be taken as tool point – holder cross FRFs of the system.

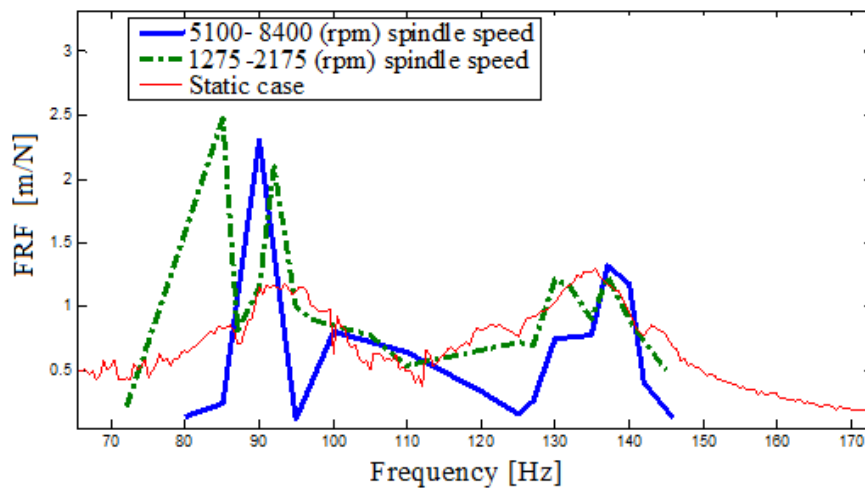


Figure 4-6 Tool point – holder cross FRFs for static case and during cutting operation.

As can be seen from Figure 4-6, during cutting significant changes in the FRFs are observed. This is more pronounced at the first spindle mode located at 90 Hz, which is shifted to the lower frequencies during cutting operation. For the second mode located at 135 Hz, no significant change is observed compared to the first mode. But it should be kept in mind that FRFs given in Figure 4-6 are obtained by using the assumption that system dynamics is not affected from relatively small spindle speed variations.

4.4 Cutting with Specially Designed Workpiece

Rather than exciting the system with harmonic cutting forces as shown in Figure 4-3 and Figure 4-4, exciting the system with random forces can provide much more valuable information for the determination of the spindle FRF. In order to excite the system with random cutting forces, specially designed workpiece can be used [52]. For that purpose, a workpiece having randomly distributed channels with random thicknesses is prepared as shown in Figure 4-7.

Cutting operation is performed on the same 5-axis machining center where 25 mm diameter end mill with 50 mm overhang length is attached to the holder. Cutting was performed with 1 mm axial depth of cut, 30% radial depth of cut and 500 rpm spindle speed. During the machining operation, cutting forces were measured with a dynamometer which is directly connected to the workpiece and response of the system is measured at the tool holder of the system with a laser vibrometer.

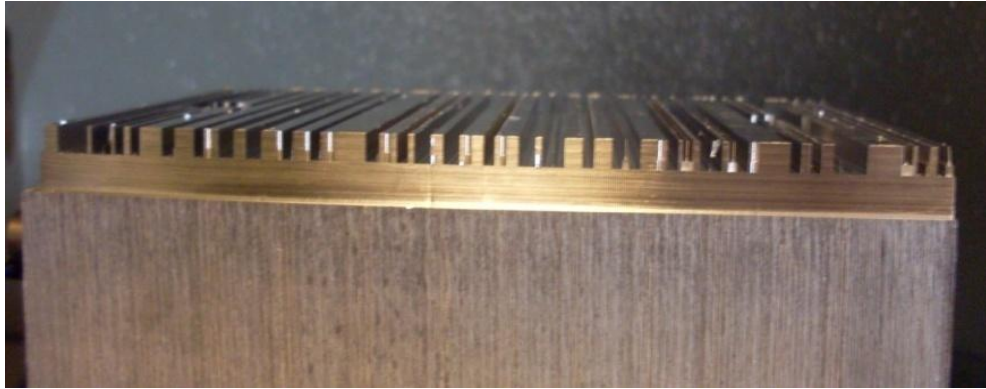


Figure 4-7 Workpiece with random surface profile.

During the determination of the tool point – holder cross FRF, H3 estimator is used due to the feedback characteristics of the cutting operation. Coherence function between the cutting force in the x direction with respect to the spindle axis and vibrometer measurement is shown in Figure 4-8.

As seen from Figure 4-8, for low frequencies around the interested spindle modes, which are located between 70 Hz and 140 Hz, coherence function is around 0.6-0.8 which decreases with frequency. Especially for frequencies larger than 800 Hz, coherence is close to 0. This high frequency behavior of the identification process is an expected result due to the limited measurement capacity of the dynamometer.

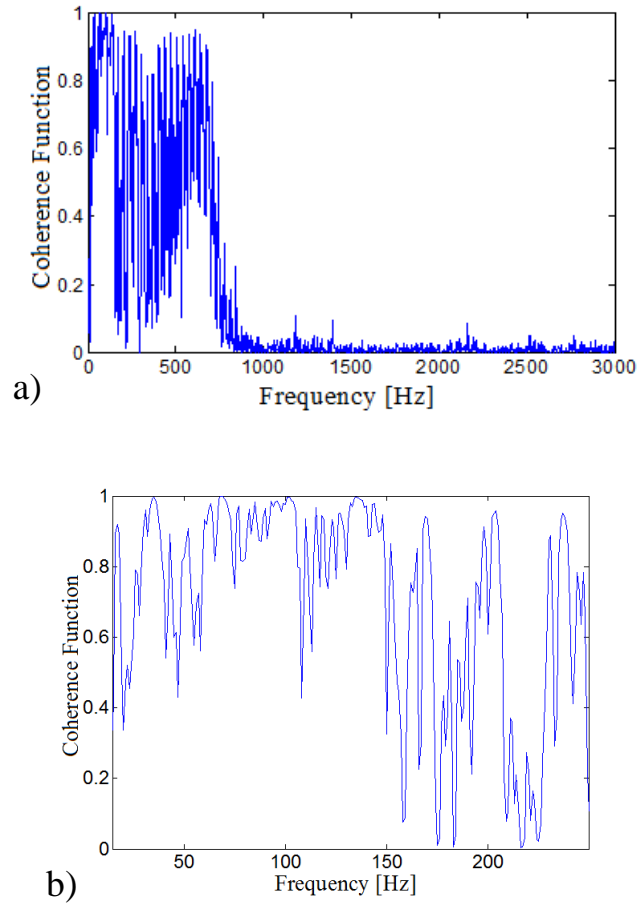


Figure 4-8 Coherence function between the cutting force in the x direction with respect to the spindle axis and vibrometer measurement.

The tool point – spindle cross FRF obtained by using H3 estimator is given in Figure 4-9. As it can be seen from this figure as well, similar changes are observed in the spindle FRF for the three different spindle speeds considered. For the spindle mode located at 100 Hz, there is a decrease in the stiffness. For the second mode located in 140-160 Hz frequency band, in addition to the decrease in the stiffness, damping values are increased. These results are consistent with the expected bearing stiffness and damping changes under rotating conditions as stated in [18] since bearing properties affect mainly the spindle modes [14].

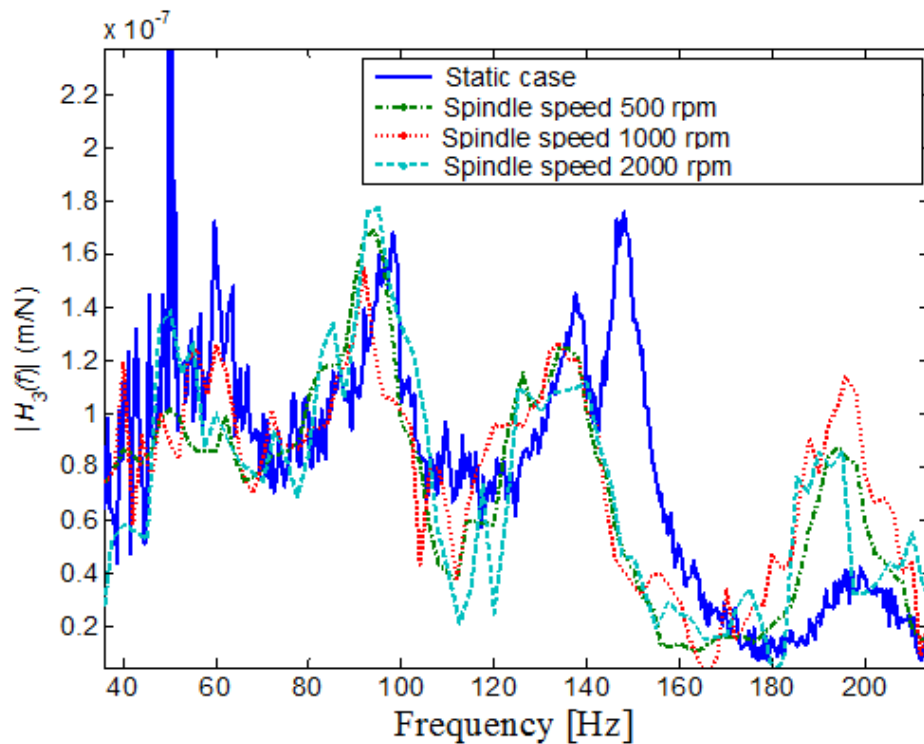


Figure 4-9 Tool point – holder cross FRFs for static case and during cutting operation at spindle speeds 500 rpm, 1000 rpm and 2000 rpm.

In order to overcome the harmonic content problem of the cutting forces, specially designed workpiece which has randomly distributed channels on the upper surface is used during operation. In this approach, system FRF is obtained for each spindle speed uniquely. However; due to the measurement capability of the dynamometer, tool point FRF is determined for lower frequencies and elastic modes that determine the stability could not be identified. Also due to the noise problems at high spindle speeds, tool point FRFs could not be identified above 2000 rpm spindle speed.

CHAPTER 5

INVERSE STABILITY SOLUTION FOR IN PROCESS TOOL POINT FRF IDENTIFICATION

In this chapter, a new identification method called inverse stability solution is proposed for the in process FRF determination. For that purpose, actual chatter frequency and axial depth of cut at limit are employed in the identification method suggested. Proposed method is applied on a real machining center for two different holder – tool combinations and verified with chatter test results.

5.1 Mathematical Formulation

In the stability theory, axial depth of cut at limit and chatter frequency can be determined as follows [5]:

$$a_{\text{lim}} = -\frac{2\pi\Lambda_R}{NK_t} (1 + \kappa^2) \quad (5.1)$$

$$\omega_c T = \cos^{-1} \left(\frac{\kappa^2 - 1}{\kappa^2 + 1} \right) \quad (5.2)$$

where

$$\Lambda = (\Lambda_R + \Lambda_I i) = -\frac{1}{2a_0} \left(a_1 \pm \sqrt{a_1^2 - 4a_0} \right) \quad (5.3)$$

$$a_0 = G_{xx} G_{yy} (\alpha_{xx} \alpha_{yy} - \alpha_{xy} \alpha_{yx}) \quad (5.4)$$

$$a_1 = \alpha_{xx}G_{xx} + \alpha_{yy}G_{yy} \quad (5.5)$$

$$\alpha_{xx} = \frac{1}{2}[\cos 2\phi - 2K_r\phi + K_r \sin 2\phi]_{\phi_{st}}^{\phi_{ex}} \quad (5.6)$$

$$\alpha_{xy} = \frac{1}{2}[-\sin 2\phi - \phi + K_r \cos 2\phi]_{\phi_{st}}^{\phi_{ex}} \quad (5.7)$$

$$\alpha_{yx} = \frac{1}{2}[-\sin 2\phi + 2\phi + K_r \cos 2\phi]_{\phi_{st}}^{\phi_{ex}} \quad (5.8)$$

$$\alpha_{yy} = \frac{1}{2}[-\cos 2\phi - 2K_r\phi - K_r \sin 2\phi]_{\phi_{st}}^{\phi_{ex}} \quad (5.9)$$

$$\kappa = \frac{\Lambda_I}{\Lambda_R} \quad (5.10)$$

where G_{xx} and G_{yy} are the tool point FRFs in the x and y directions respectively, N is the number of cutting teeth, K_t is the cutting force coefficient, ϕ_{st} and ϕ_{ex} are start and exit angle of cutting tooth, T is tooth period.

Note that, tool point FRFs can be expressed using modal parameters as follows:

$$G_{xx} = \sum_{r=1}^n \frac{1 - \frac{\omega_c}{\omega_n^r} + 2\xi^r \left(\frac{\omega_c}{\omega_n^r}\right)^2}{k_r \left(\left(1 - \left(\frac{\omega_c}{\omega_n^r}\right)^2\right)^2 + \left(2\xi^r \left(\frac{\omega_c}{\omega_n^r}\right)\right)^2 \right)} i \quad (5.11)$$

where ξ^r is damping ratio of the r^{th} mode in x direction, ω_n^r is natural frequency of the r^{th} mode in x direction and ω_c is chatter frequency.

Analytical definitions of chatter frequency and corresponding axial depth of cut given by Equation (5.1) and Equation (5.2) can be used for the identification of tool point FRF with the experimentally obtained chatter frequency and axial depth of cut as follows:

$$a_{\text{lim}}^{\text{analytical}} = a_{\text{lim}}^{\text{experimental}} \quad (5.12)$$

$$\omega_c^{\text{analytical}} = \omega_c^{\text{experimental}} \quad (5.13)$$

As can be seen from Equation (5.11), each tool point FRF in two orthogonal planes contains 3 unknowns for each mode which are modal stiffness, natural frequency and damping. However; equating experimentally and analytically obtained chatter frequency and axial depth of cut 2 equations can be obtained as shown in Equation (5.12) and Equation (5.13).

At this point characteristics of the stability theory can be used for simplification of the solution procedure. First, it is well known that depending on the dominant characteristics of the spindle – holder – tool assembly modes in the tool point FRF, different regions of the stability diagram is determined by different modes. Thus instead of using summation term in tool point FRF, each mode can be identified using different regions of stability diagram.

In addition to the stability behavior, it can be assumed that modal mass of each mode remains same. Using this assumption modal stiffness and damping in each orthogonal plane can be treated as unknowns. Thus, identification procedure requires the determination of 4 unknowns. At this point, two different approaches can be applied. First, chatter test results at a certain

spindle speed can be used and 4 unknown can be determined using optimization techniques since each chatter test provides 2 equations as shown in Equation (5.12) and Equation (5.13).

Alternatively, chatter test results for two different spindle speeds can be used and 4 unknowns can be solved using 4 nonlinear sets of equations. For the second alternative, it can be assumed that variations of the tool point FRF can be neglected by small spindle speed variations. For instance, for the identification of the system dynamics, chatter test results at 7400 rpm and 7500 rpm can be used based on this assumption. In addition, by adding one more chatter test results at a different spindle, 6 unknowns in two orthogonal planes can also be solved using least square error method.

As a summary, for the identification purpose first, tool point FRFs should be obtained using impact test and stability diagrams should be determined using the stability theory proposed by Budak and Altıntaş [5]. Based on the characteristics of stability diagrams, modes that effect the stability of the cutting operation can be directly determined from calculated stability diagrams and chatter frequencies. Then modal parameters of the tool point FRF should be determined using modal identification. Finally, keeping the modal stiffness and damping of the dominant mode as unknown, chatter frequency and axial depth of cut can be determined analytically. In order to identify unknown modal parameters, required equations can be obtained through chatter tests. At a certain spindle speed, actual values of the chatter frequency and axial depth of cut can be obtained. Thus, using the analytically and experimentally obtained chatter frequency and axial depth of cut, unknown modal parameters can be identified using Equation (5.12) and Equation (5.13). Proposed solution procedure is also given in Figure 5-1.

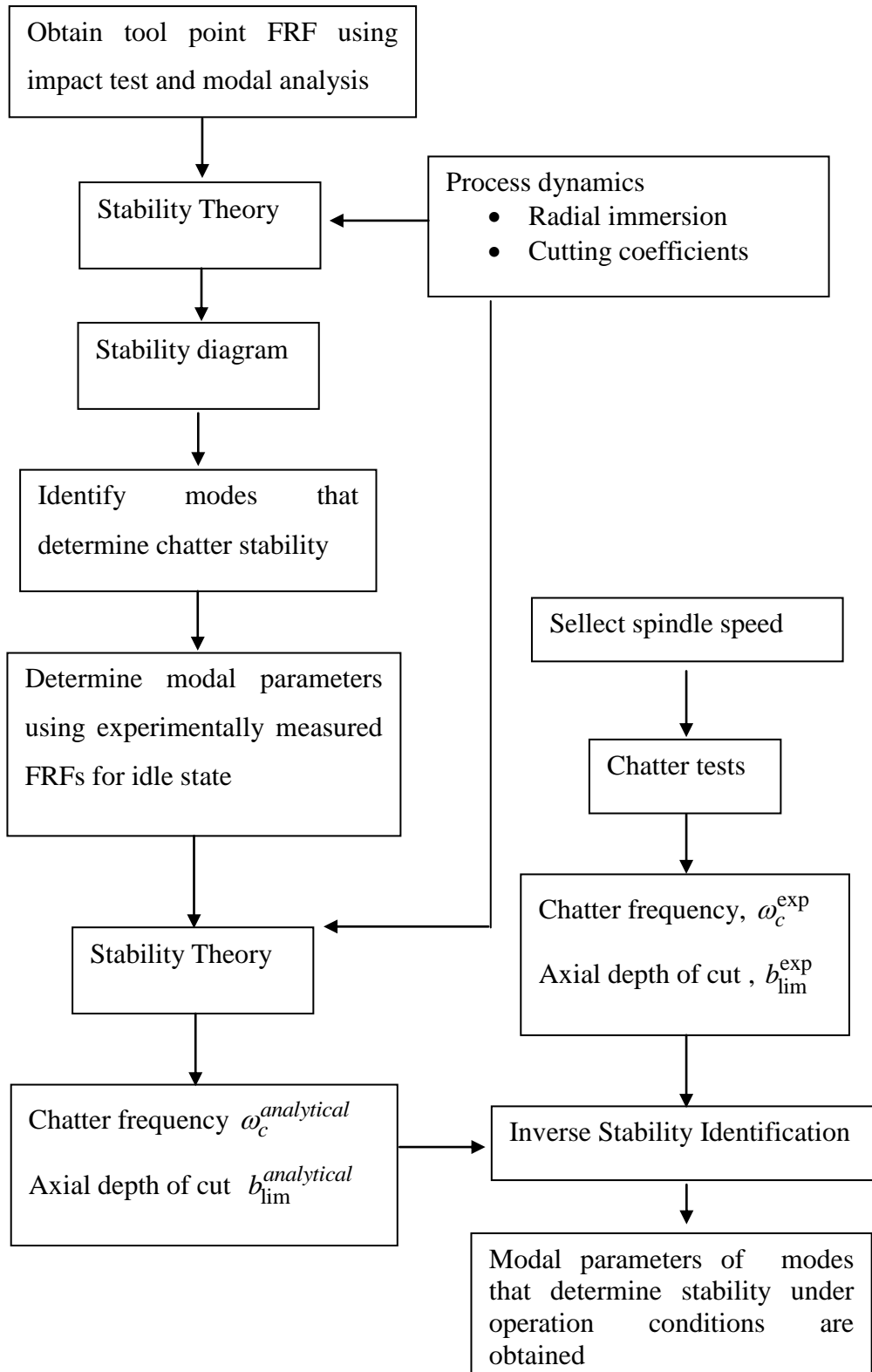


Figure 5-1 Inverse stability solution procedure

5.2 Application on real machining center

In this section, proposed inverse stability solution procedure is applied on a real machining center for various holder and tool geometries. First, tool point FRFs are obtained using impact testing for the idle state of the machining center. Using the impact test results, predicted stability diagrams of the cutting processes are obtained with the stability model of Budak and Altintas [5]. Then chatter tests are performed for various spindle speeds where chatter frequency and axial depth of cut at the stability limits are determined. Finally, using the chatter test results, variations in the tool point FRFs are determined with the proposed solution procedure.

5.2.1 Case Study 1

It is a well phenomenon that during high speed cutting operations, gyroscopic moments cause separation in assembly modes into backward and forward modes. In addition to structural variations, due to gyroscopic moments and centrifugal forces, bearing stiffness values decrease. Also as shown in Chapter 3, variations in the spindle modes cause variations in the stability of the process in cases where the tool mode is not dominant in determining the stability in the frequency range of interest. Thus, to investigate the variations of tool point FRF during cutting operation and to be able to identify the variations of the spindle modes, relatively rigid end mill whose diameter is 25 mm with 40 mm gauge length and 4 teeth is clamped to the machining center. Geometry of the holder and tool are given in Table 5-1 and Table 5-2 respectively.

Table 5-1 Holder dimensions

Segment number	1	2	3	4	5	6
Length (mm)	26	58	17	15	40	30
Outer Diameter (mm)	63	50	45	60	45	30
Inner Diameter (mm)	25	25	15	15	15	15

Table 5-2 Tool Dimensions

Segment number	1	2
Length (mm)	40	60
Outer Diameter (mm)	23	25
Inner Diameter (mm)	0	0

First, the tool point FRFs in x and y directions are obtained by impact testing for the idle state of the machining center. Obtained tool point FRFs in x and y directions are given in Figure 5-2 and Figure 5-3 respectively.

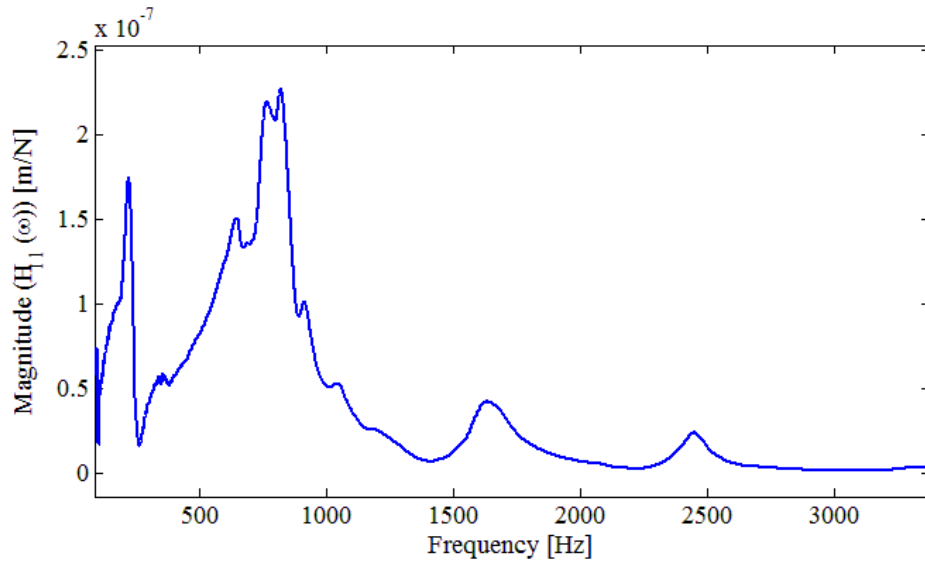


Figure 5-2 Tool point FRF in the x – direction at the idle state.

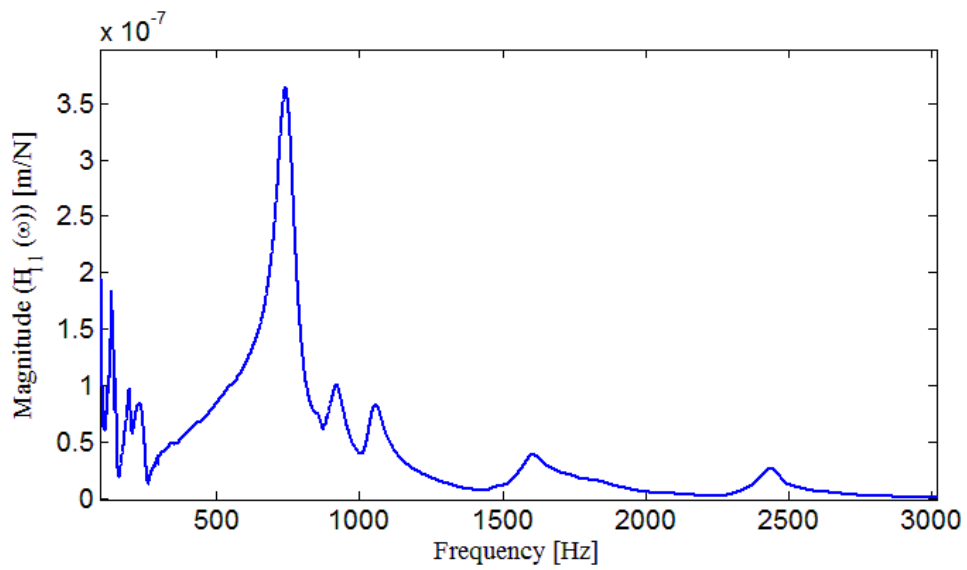


Figure 5-3 Tool point FRF in the y – direction at the idle state.

In addition to the tool point FRFs given in Figure 5-2 and Figure 5-3, modal parameters of the tool point FRFs are identified using modal identification techniques and given in Table 5-3 and Table 5-4 respectively. Also calculated tool point FRFs using modal parameters for x and y directions are given and also compared with experimental ones in Figure 5-4 and Figure 5-5, respectively.

Table 5-3 Modal parameters of the tool point FRF in x-direction

Mode number	Natural frequency (Hz)	Modal stiffness (N/m)	Damping ratio (%)
1 st mode	225	7.7×10^7	4.25
2 nd mode	660	8.31×10^7	7.88
3 th mode	800	3×10^8	7.79
4 th mode	1632	2.6×10^8	4.37

Table 5-4 Modal parameters of the tool point FRF in y-direction

Mode number	Natural frequency (Hz)	Modal stiffness (N/m)	Damping ratio (%)
1 st mode	241	1.46×10^8	5.56
2 nd mode	744	3.37×10^7	4.11
3 th mode	907	1.97×10^8	3.63
4 th mode	1046	3.54×10^8	2.18

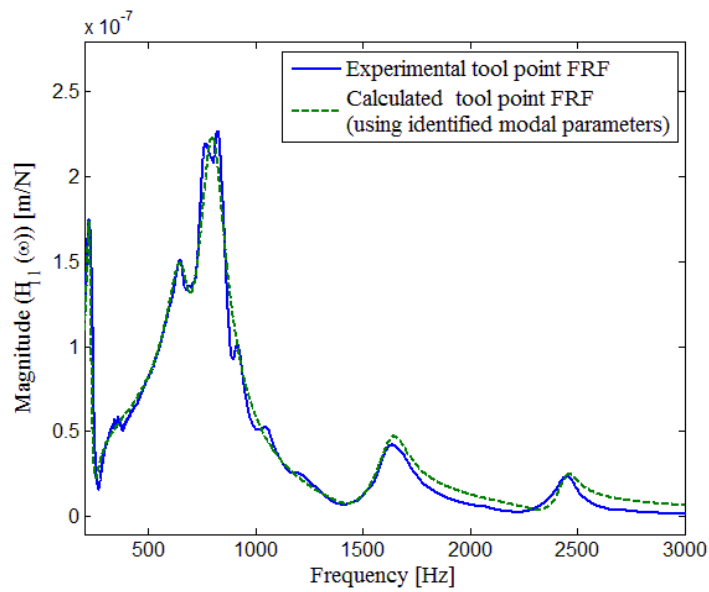


Figure 5-4 Comparison of tool point FRF in x direction obtained using modal testing with that calculated using identified modal values.

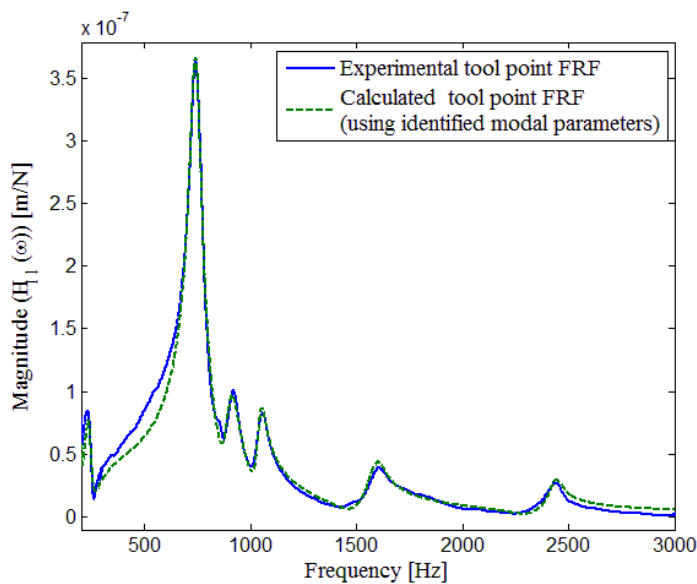


Figure 5-5 Comparison of tool point FRF in y direction obtained using modal testing with that calculated using identified modal values.

In order to determine the variations of the tool point FRF under cutting conditions, chatter tests are performed on Deckel Maho 5 axis machining center with the holder – tool combination whose dimensions are given in Table 5-1 and Table 5-2. Cutting is performed on 7075 aluminum workpiece with 100% radial immersion and 0.1 mm/tooth feed. During the chatter tests, at certain spindle speeds, axial depth of cut is increased incrementally and sound is measured with a microphone. Finally, using the spectrum of the sound information and observations on the workpiece surface, chatter frequency and corresponding axial depth of cut are determined. Machining center and experimental setup are shown in Figure 5-6.



Figure 5-6 Experimental setup.

For instance, for 14000 rpm spindle speed, for the stable cutting condition frequency spectrum of the microphone measurement is shown in Figure 5-7. As seen from Figure 5-7, dominant frequency components are located at 466 Hz and 935 Hz which are second harmonics of the spindle rotational frequency and tooth passing frequency, respectively.

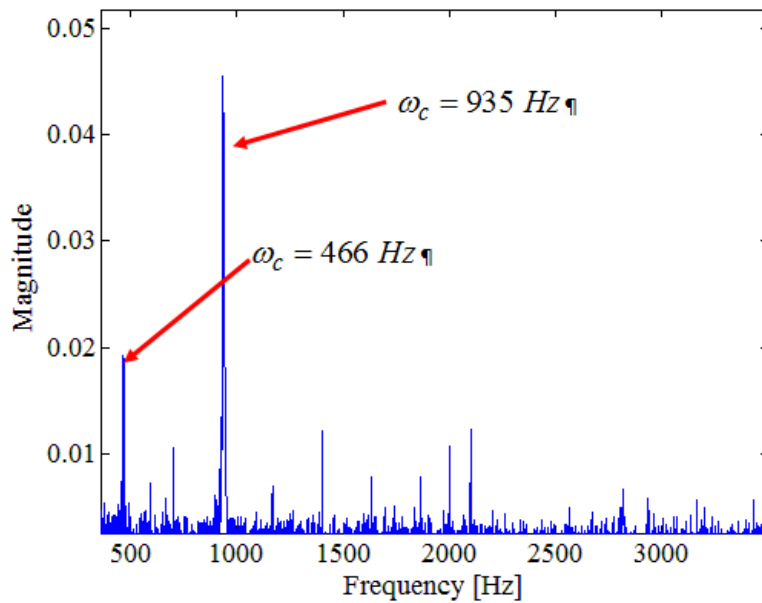


Figure 5-7 Frequency spectrum of microphone measurement of the stable cutting operation at 14000 rpm spindle speed.

In addition to stable cutting measurements, at the instant that chatter occurred, frequency spectrum of the microphone measurement is given in Figure 5-8. In addition to microphone measurements, workpiece surface obtained after the stable and unstable cutting operations are given in Figure 5-9 . As seen from Figure 5-8, dominant frequency component is at 616 Hz which is not a tooth

passing frequency or one of its higher harmonics. Also as shown in Figure 5-9, chatter marks appears on the workpiece surface in unstable cutting operations.

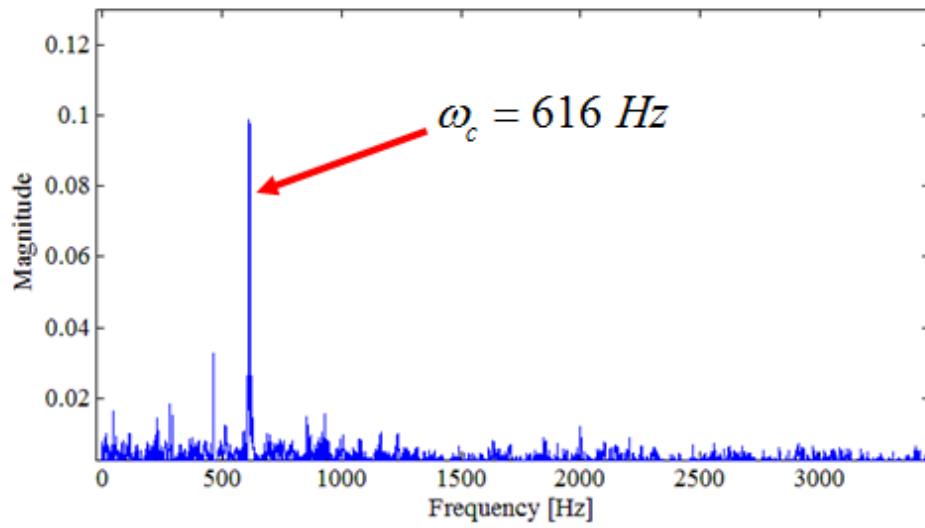


Figure 5-8 Frequency spectrum of microphone measurement of the unstable cutting operation at 14000 rpm spindle speed.

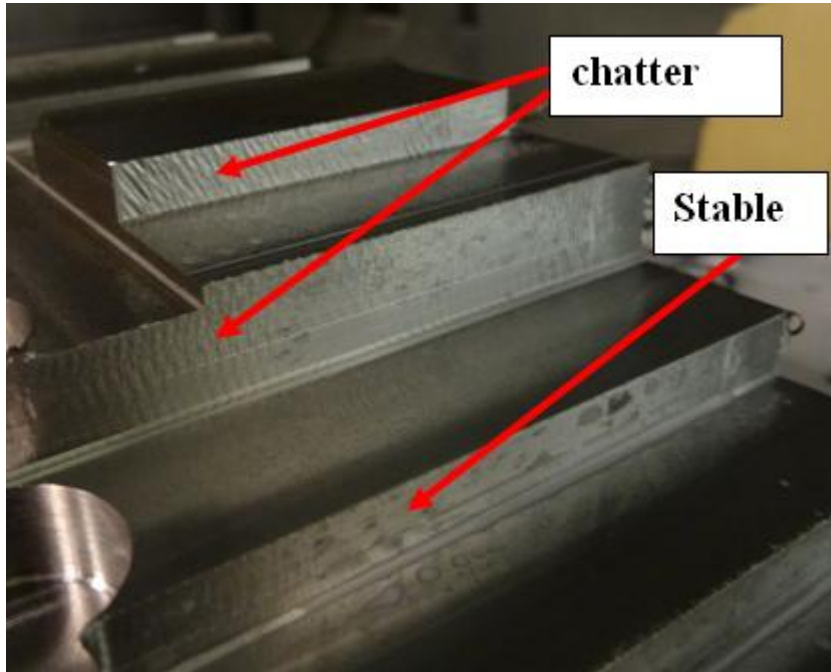


Figure 5-9 Workpiece surface after stable and unstable cutting operations.

In addition to the 14000 rpm spindle speed, chatter tests are performed at various other spindle speeds and obtained results are given in Figure 5-10 with the predicted stability diagram which is obtained using the tool point FRF for idle state of the machining center. Also chatter frequencies and corresponding axial depth of cuts at the limit are given in Table 5-5 with the predicted chatter frequencies and axial depth of cuts using idle state FRFs.

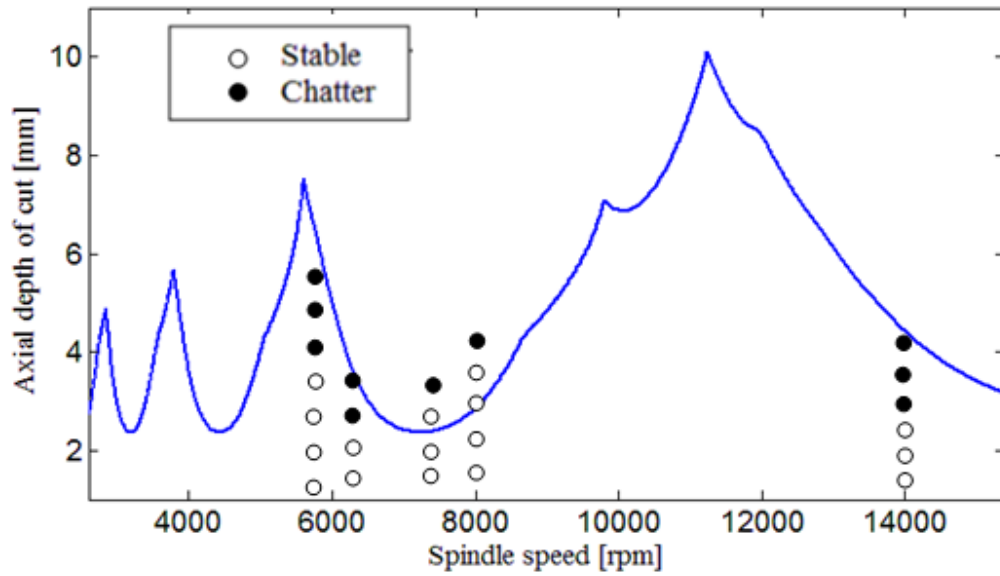


Figure 5-10 Stability diagrams obtained for idle state and chatter test results.

Table 5-5 Predicted and actual values of the chatter frequency and axial depth of cut.

Spindle Speed (rpm)	Cutting speed (mm/s)	Predicted a_{lim} (mm)	Predicted chatter frequency ω_c (Hz)	Actual a_{lim} (mm)	Actual chatter frequency ω_c (Hz)
6200	8115	4	727.5	2.65	694
6300	8247	3.6	732	2.6	697
7400	9686	2.39	762	2.8	727
7500	9818	2.42	764.4	3.1	728
14000	18300	4.45	722.8	3	616

As seen from Figure 5-10 and Table 5-5, considerable amount of discrepancies are observed between the predicted and actual stability of the cutting operation. Due to the relatively high speeds, these discrepancies cannot be due to the process damping effect [35].

In order to identify the tool point FRF, first, modes in x and y directions that effect stability are determined. As given in Table 5-5, predicted chatter frequencies are between 720 Hz and 765 Hz. Thus it can be concluded that 3rd mode in x direction and 2nd mode in y direction are dominant modes and chatter would occur due to these modes. Therefore, modal stiffness and damping of these modes are taken as unknown parameters and remaining modal parameters are kept constant. Then, using the cutting process parameters and stability theory chatter frequency and axial depth of cut are calculated analytically at spindle speeds given in Table 5-5. Finally equating analytically and experimentally obtained chatter frequencies and corresponding axial depth of cuts, unknown modal parameters are obtained using proposed solution procedure. Results of these calculations are given in Table 5-6 and Table 5-7. Note that, for the identification procedure, it is assumed that variations in the tool point FRF for an increment of 100 rpm spindle speed can be neglected. Thus, in order to determine both natural frequency and damping ratio, two sets of chatter test results differ from each other by 100 rpm spindle speed are used simultaneously in the identification procedure.

Table 5-6 Identified modal parameters in x direction at various spindle speeds

	Spindle speed 0 rpm	Spindle speed 6200 rpm – 6300 rpm	Spindle speed 7400 rpm – 7500 rpm	Spindle speed 13900 rpm – 14000 rpm
Natural frequency (Hz)	800	797	793	782
Damping (%)	7.79	5.1	8	8.8

Table 5-7 Identified modal parameters in y direction at various spindle speeds

	Spindle speed 0 rpm	Spindle speed 6200 rpm – 6300 rpm	Spindle speed 7400 rpm – 7500 rpm	Spindle speed 13900 rpm – 14000 rpm
Natural frequency (Hz)	744	672	642	611
Damping (%)	4.11	7.6	3.9	5.7

As seen from the identification results given in Table 5-6 and Table 5-7, the dominant mode shows a speed dependent behavior and with increasing spindle speed, the shift in the dominant mode increases.

In addition to the identification results, dominant mode of tool point FRF is recalculated for the 7400 rpm – 7500 rpm spindle speed range using the identification results and obtained tool point FRFs in x and y directions are given with the tool point FRFs of the idle state in Figure 5-11 and Figure 5-12 respectively.

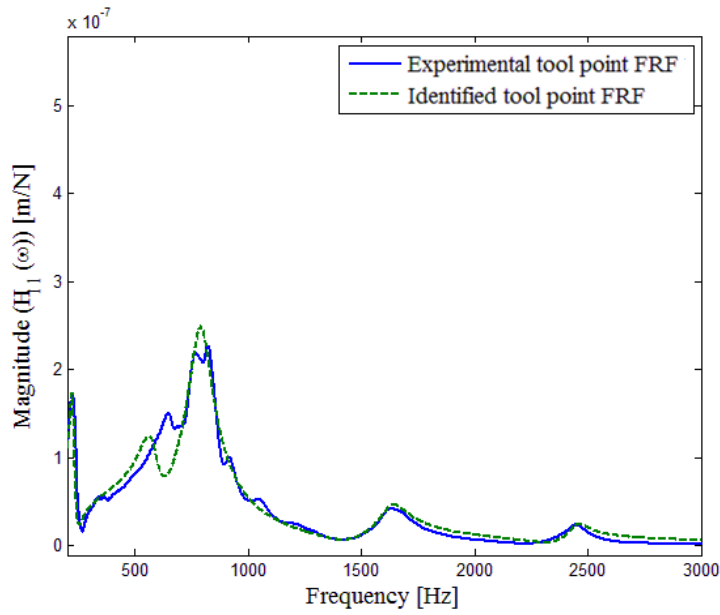


Figure 5-11 Idle condition tool point FRF and calculated tool point FRF using identified parameters for 7400-7500 rpm spindle speed in x direction.

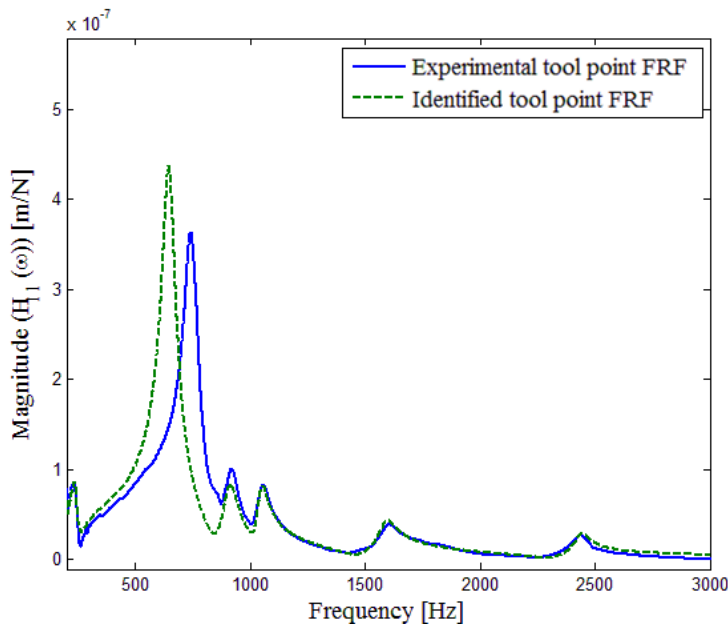


Figure 5-12 Idle condition tool point FRF and calculated tool point FRF using identified parameters for 7400-7500 rpm spindle speed in y direction.

In order to check the accuracy of the identification procedure, stability diagrams are recalculated using the identified tool point FRFs under operational conditions. Obtained stability diagrams are given with the stability diagrams obtained for the idle state and chatter test results in Figure 5-13 - Figure 5-15. Note that, recalculated stability diagrams using the identified tool point FRFs under operational conditions are called modified stability.

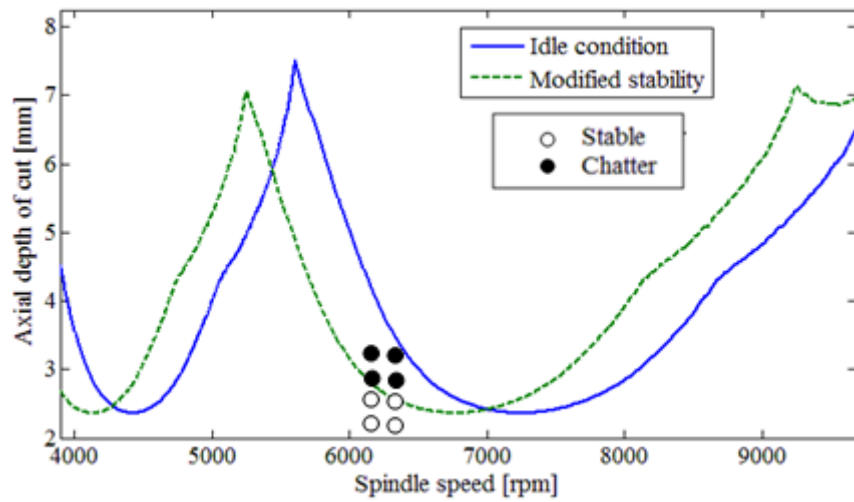


Figure 5-13 Stability diagrams obtained for idle state and 6300 rpm – 6400 rpm spindle speeds.

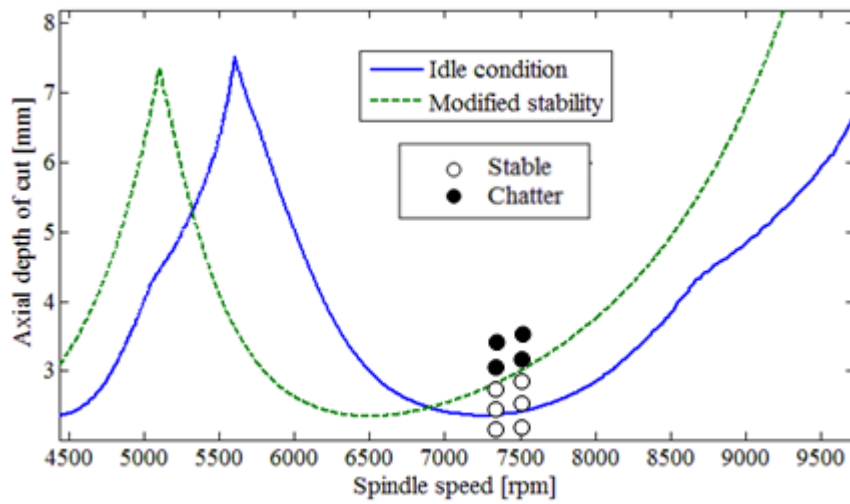


Figure 5-14 Stability diagrams obtained for idle state and 7400 rpm – 7500 rpm spindle speeds.

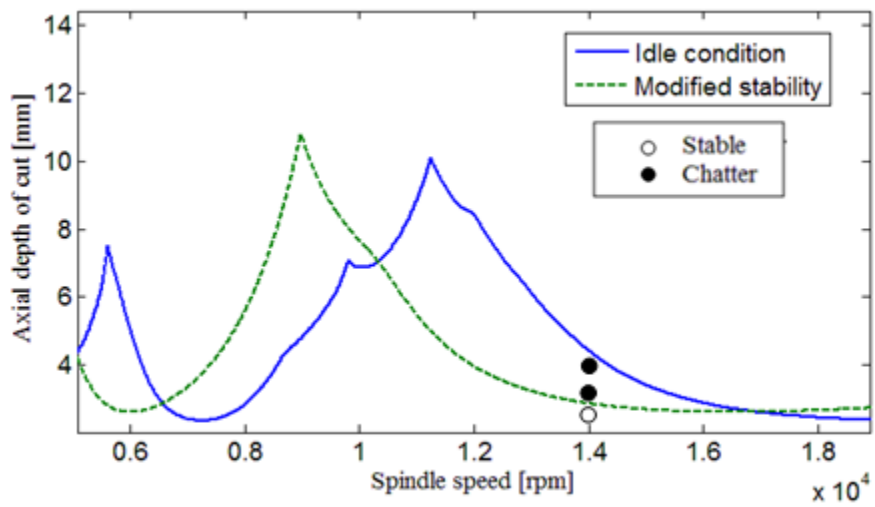


Figure 5-15 Stability diagrams obtained for idle state and 13900 rpm - 14000 rpm spindle speeds.

As seen from Figure 5-13 - Figure 5-15, with the increasing spindle speed, deviations in the stability of the cutting operation increases. Also note that each stability diagram given in Figure 5-13 - Figure 5-15, is valid in the vicinity of the spindle speeds used during identification. In addition to the stability diagrams given in Figure 5-13 - Figure 5-15, predictions obtained using modified stability diagrams are given in Table 5-8 with the actual chatter test results.

Table 5-8 Predictions obtained using modified stability diagrams and actual values of the chatter frequency and axial depth of cut.

Spindle Speed (rpm)	Predicted a_{lim} (mm)	Predicted chatter frequency ω_c (Hz)	Actual a_{lim} (mm)	Actual chatter frequency ω_c (Hz)
6200	2.7	694.3	2.65	694
6300	2.65	696.8	2.6	697
7400	2.85	727	2.8	727
7500	3.07	728.3	3.1	728
14000	2.8	616	3	616

As seen from Table 5-8, compared to predictions given in Table 5-5 which are obtained using tool point FRF of the idle state of machining center, stability of the cutting operation can be predicted accurately with the modified stability diagrams.

5.2.2 Case Study 2

In addition to the identification of speed dependent system behavior during cutting operation, in order to investigate the effect of cutting forces on system dynamics, tool point FRF of the same spindle – holder – tool assembly is identified under various cutting forces.

For a cutting operation at a certain spindle speed, cutting forces can be increased by increasing radial immersion or feed per tooth. Therefore, to investigate the effect of force amplitude on the system dynamics two alternative approaches can be applied. First, identification can be performed with various radial depth of cuts. For instance, stability diagrams of a cutting operation on 7075 aluminum workpiece with 0.1 mm/tooth feed are calculated for radial immersion of 100% and 50%. Calculated stability diagrams are given in Figure5-16.

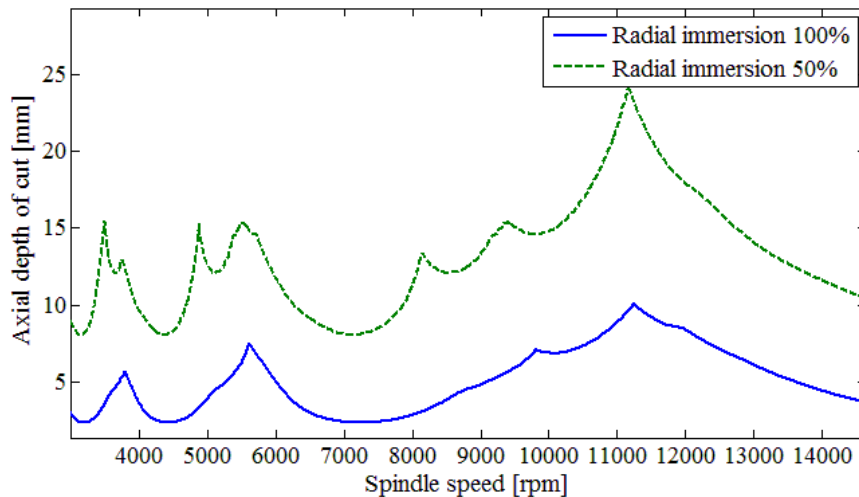


Figure5-16 Stability diagrams obtained by idle state FRF with radial immersion of 100% and 50%.

As seen from Figure5-16, when radial immersion is decreased, stable axial depth of cuts increase. Since it is difficult to perform chatter tests with such high axial depth of cuts, altering cutting forces with changing radial immersion is not a feasible approach for this case.

For the second alternative, stability diagrams of a cutting operation on 7075 aluminum workpiece with 100% radial immersion with feed per tooth values of 0.08 mm/tooth and 0.2 mm/tooth are calculated. Calculated stability diagrams are given in Figure 5-17.

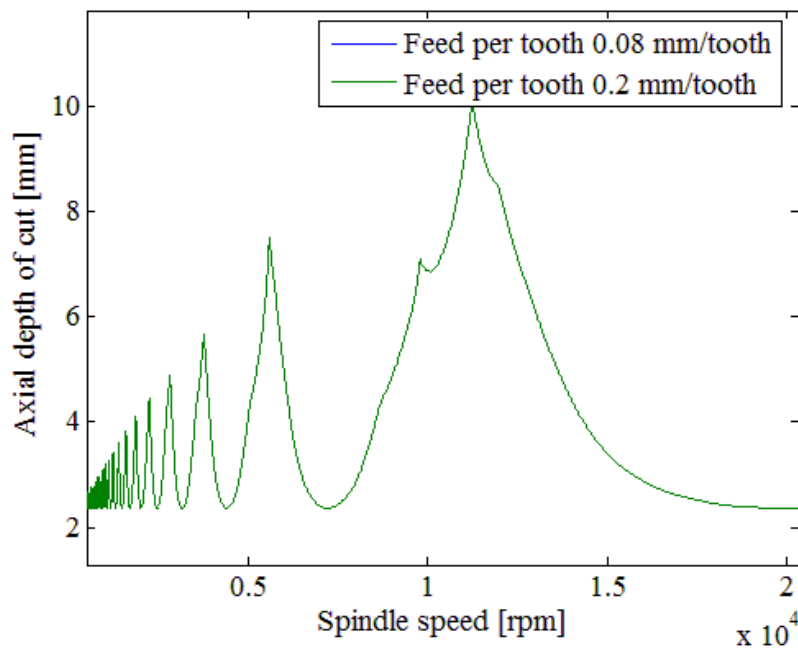


Figure 5-17 Stability diagrams obtained by idle state FRF with feed 0.08 mm/tooth and 0.2 mm/tooth.

As seen from Figure 5-17, changing feed of the cutting operation does not affect stability of the process. Therefore, for the investigation of the effect of cutting forces on the system dynamic, chatter tests are performed at 7500 rpm spindle speed with feed values of 0.08 mm/tooth, 0.1 mm/tooth, 0.16 mm/tooth and 0.2 mm/tooth values. Radial immersion is taken as 100%. Experimentally determined chatter frequencies and corresponding axial depth of cuts at the limit are given in Table 5-9 with the predicted chatter frequencies and axial depth of cuts obtained using stability diagrams for idle condition.

Table 5-9 Predicted and actual values of the chatter frequency and axial depth of cut for 7500 rpm spindle speed with changing feed.

Feed per tooth (mm/tooth)	Predicted a_{lim} (mm)	Predicted chatter frequency ω_c (Hz)	Actual a_{lim} (mm)	Actual chatter frequency ω_c (Hz)
0.08	2.42	764.4	3	731
0.1	2.42	764.4	3.1	728
0.16	2.42	764.4	3.25	718
0.2	2.42	764.4	3.45	706

As seen from Table 5-9, with increasing feed, deviations between the predicted and actual stability of the cutting operation increases. This behavior is an obvious evidence of the force dependent characteristics of the tool point FRF.

Similar to the previous case studies, using the chatter test results modal parameters of the dominant mode is identified and identified modal parameters for x and y directions are given in Table 5-10 and Table 5-11, respectively.

As seen from identification results given in Table 5-10 and Table 5-11, with increasing feed, the dominant mode deviates more from the idle condition. This behavior shows that system dynamics is also affected by the forcing level that excites the machining center.

Table 5-10 Identified modal parameters in x direction at 7500 rpm spindle speed with various feed

	Idle	Feed 0.08 mm/tooth	Feed 0.1 mm/tooth	Feed 0.16 mm/tooth	Feed 0.2 mm/tooth
Natural frequency (Hz)	800	726	726	716	699
Damping (%)	7.79	6.8	6.9	8	9

Table 5-11 Identified modal parameters in y direction at 7500 rpm spindle speed with various feed

	Idle	Feed 0.08 mm/tooth	Feed 0.1 mm/tooth	Feed 0.16 mm/tooth	Feed 0.2 mm/tooth
Natural frequency (Hz)	744	684	676	663	651
Damping (%)	7.79	8.5	8	7.4	7

Finally, in order to verify the accuracy of identified modal parameters under operational conditions, stability diagrams are recalculated using identified modal parameters and they are given in Figure 5-18. As seen from Figure 5-18, feed values of the cutting operations cause deviations in the actual stability of the process and with increasing feed deviations in the stability increase. Also note that modified stability diagrams given in Figure 5-18 are valid at 7500 rpm spindle speed and for higher spindle speeds such as 12000 rpm, deviations from idle condition will be much more and it is observed that effects of operating conditions cause increase in stability limit at 7500 rpm spindle speed. However; at 12000 rpm spindle speed effects of operating conditions cause decrease in stability limit.

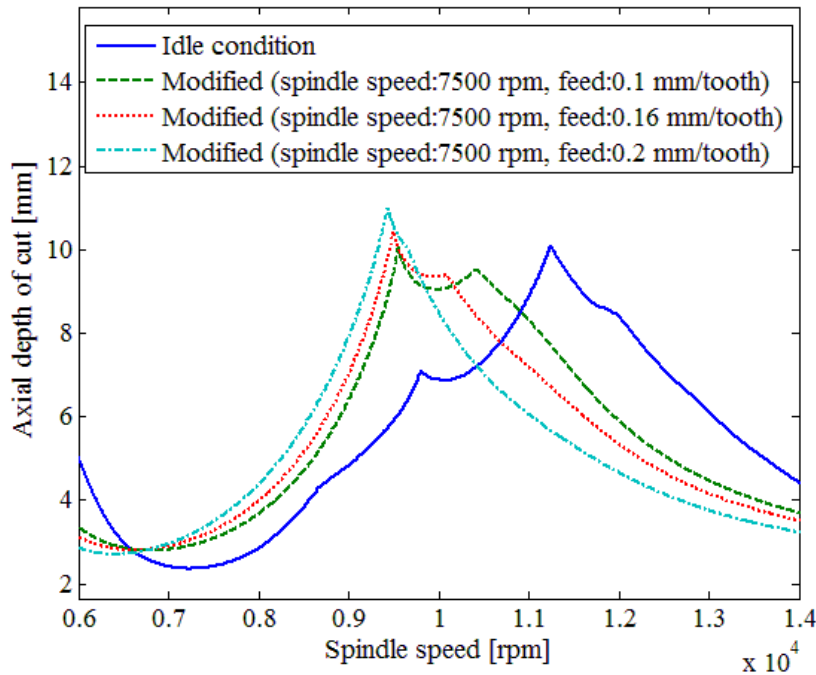


Figure 5-18 Stability diagrams obtained by idle state FRF and identified in process FRFs at 7500 rpm spindle speed with feed of 0.1 mm/tooth, 0.16 mm/tooth, and 0.2 mm/tooth.

Table 5-12 Predictions obtained using idle condition, modified stability diagrams and actual values of the chatter frequency and axial depth of cut.

Feed (mm/tooth)	Predicted a_{lim} (mm) (idle FRF)	Predicted a_{lim} (mm) (in process FRF)	Actual a_{lim} (mm)
0.1	2.7	3.08	3.1
0.16	2.65	3.22	3.25
0.2	2.85	3.42	3.45

Finally, cutting forces are calculated using Cutpro software with identified tool point FRFs at 7500 rpm spindle speed and feed values of 0.1 mm/tooth, 0.16 mm/tooth, and 0.2 feed/tooth. Calculated cutting forces in x, y and z directions are given in Figure 5-19 - Figure 5-21, respectively. Also note that, since cutting forces are also affected by axial depth of cut, during the calculation of cutting forces corresponding axial depth of cut at limit is used for each feed values.

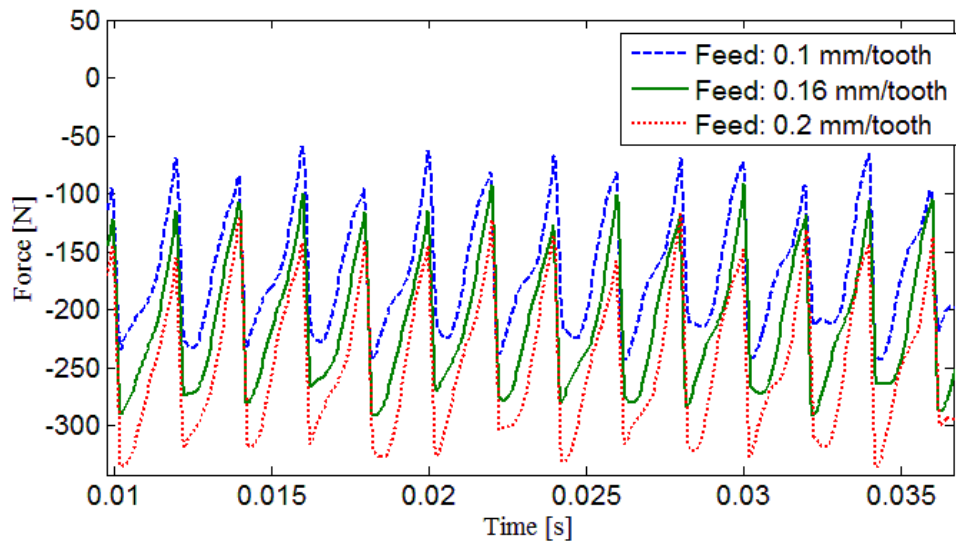


Figure 5-19 Cutting forces in x direction

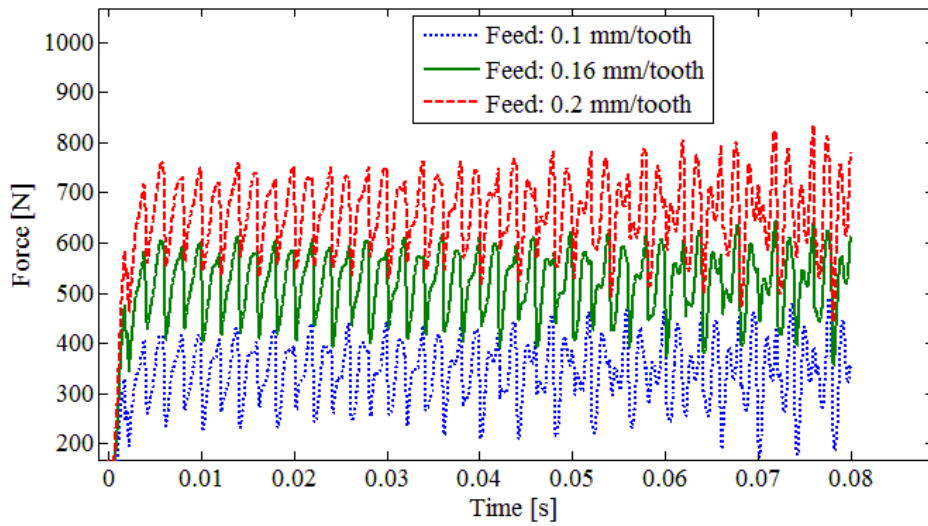


Figure 5-20 Cutting forces in y direction

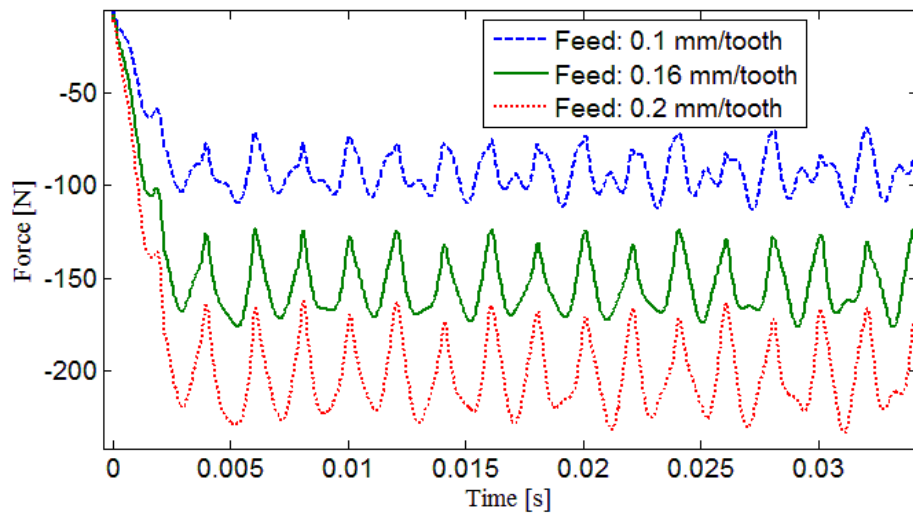


Figure 5-21 Cutting forces in z direction

As seen from Figure 5-19 - Figure 5-21, with increasing feed values, considerable amount of increase in cutting forces occurs. These force dependent characteristics can be attributed to the variations of the bearing stiffness values with increasing force on bearings.

5.2.3 Case Study 3

In order to investigate the spindle – holder – tool assembly dynamics under operational conditions where the tool point FRF is dominated by tool mode, 12 mm carbide tool with 58 mm overhang length is clamped to machining center with the holder given in Table 5-1. First, tool point FRF in x and y directions are measured by impact testing and given in Figure 5-22 and Figure 5-23, respectively.

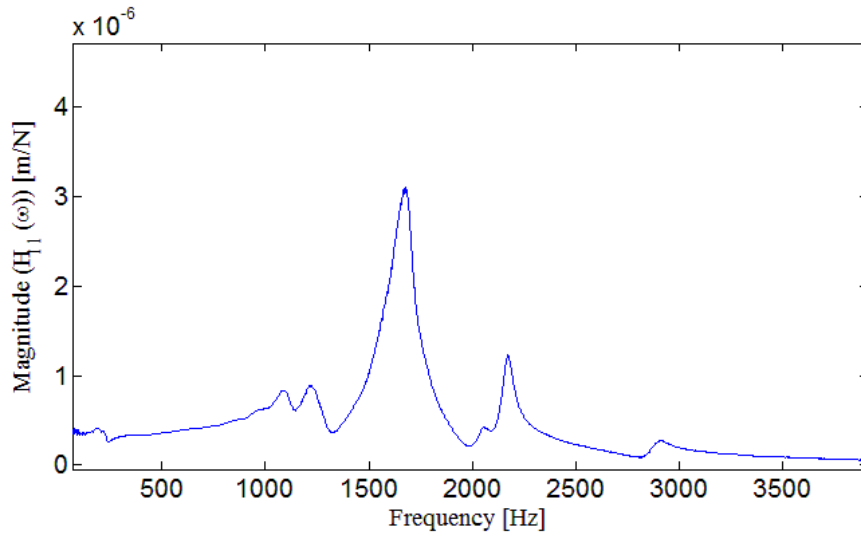


Figure 5-22 Tool point FRF in x – direction at the idle state.

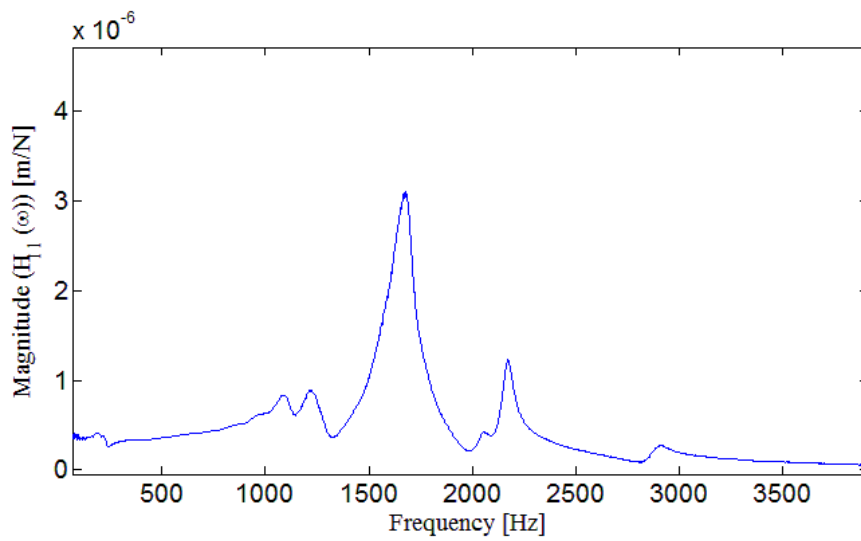


Figure 5-23 Tool point FRF in y – direction at the idle state.

In addition to the tool point FRFs given in Figure 5-22 and Figure 5-23, modal parameters of the tool point FRFs are identified using modal identification techniques and obtained modal parameters of the tool point FRFs in x and y directions are given in Table 5-13.

Table 5-13 Modal parameters of the tool mode in x and y directions.

	Natural frequency (Hz)	Modal stiffness (N/m)	Damping ratio (%)
x direction	1649	5.08×10^6	2.26
y direction	1669	4.16×10^6	3.98

Similar to previous case studies, stability diagram is determined for machining of 7075 aluminum with 100 % radial depth of cut using the tool point FRFs of the idle state of machining center. Calculated stability diagram is given in Figure 5-24. In addition to calculated stability diagram, chatter tests are performed at various spindle speeds and chatter test results are shown in Figure 5-24. Obtained chatter frequencies and corresponding axial depth of cuts at the limit are given in Table 5-14 with the predicted chatter frequencies and axial depth of cuts.

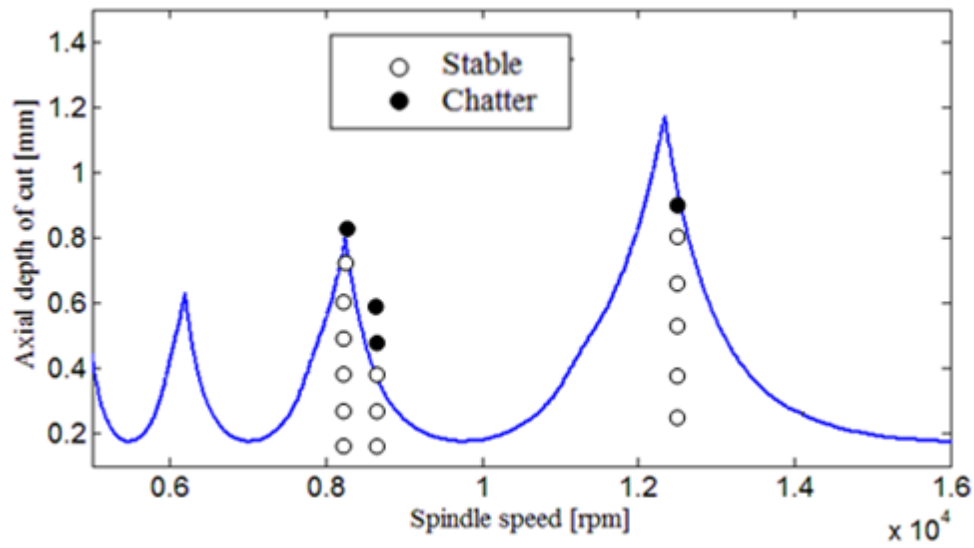


Figure 5-24 Stability diagrams obtained for idle state and chatter test results.

Table 5-14 Predicted and actual values of the chatter frequency and axial depth of cut.

Spindle Speed (rpm)	Predicted a_{lim} (mm)	Predicted chatter frequency ω_c (Hz)	Actual a_{lim} (mm)	Actual chatter frequency ω_c (Hz)
8400	0.57	1598	0.59	1614
8450	0.52	1605	0.54	1619
12500	0.95	1575	0.8	1580
12600	0.84	1580	0.78	1574
12650	0.79	1582	0.72	1583

As seen from Figure 5-24 and Table 5-14, there is not a significant deviation between the predicted and actual stability limits and chatter frequencies. Moreover, using the experimentally determined chatter frequencies and axial depth of cut, dominant tool mode of tool point FRF is identified for different spindle speeds. Identification results for x and y directions are given in Table 5-15 and Table 5-16, respectively.

Table 5-15 Identified modal parameters for tool mode in x direction at various spindle speeds.

Tool mode	Spindle speed 0 rpm	Spindle speed 8400 rpm - 8500 rpm	Spindle speed 12500 rpm - 12600 rpm
Natural frequency (Hz)	1649	1650	1625
Modal stiffness (N/m)	5.08×10^6	5.086×10^6	4.93×10^6
Modal damping ratio (%)	2	1.9	1.9

Table 5-16 Identified modal parameters in y direction at various spindle speeds.

Tool mode	Spindle speed 0 rpm	Spindle speed 8400 rpm - 8500 rpm	Spindle speed 12500 rpm - 12600 rpm
Natural frequency (Hz)	1669	1669	1640
Modal stiffness (N/m)	4.16×10^6	4.16×10^6	4.01×10^6
Modal damping ratio (%)	2.78	1.6	1.7

As shown in Table 5-15 and Table 5-16, compared to case study 1, small amounts of deviations are observed between idle state and rotating state of machining center. For instance; deviation between idle state and 12500 rpm spindle speed condition is 1.7% for x direction. Also for 8400 rpm spindle speed 4 Hz increase (0.25 %) in tool mode of the tool point FRF in x direction is observed which might be due to the experimental error or variation of the holder – tool connection parameters.

Finally, stability diagrams are recalculated using identified tool point FRFs and modified stability diagrams are validated by experimentally obtained chatter frequency and axial depth of cut. For validation purposes, modified stability diagram is obtained using identified tool point FRFs for 8400 rpm and 8450 rpm spindle speeds. Predicted values using modified stability diagram and actual values of the chatter frequency and axial depth of cut are given in Table 5-17.

Table 5-17 Actual values of the chatter frequency and axial depth of cut and predicted values by modified stability diagrams.

Spindle Speed (rpm)	Predicted a_{lim} (mm)	Predicted chatter frequency ω_c (Hz)	Actual a_{lim} (mm)	Actual chatter frequency ω_c (Hz)
6300	0.455	1620	0.46	1630
8400	0.59	1614	0.59	1614
8450	0.52	1617	0.54	1619

As seen from Table 5-17, using modified stability diagram, chatter can be predicted accurately for 8400 and 8450 rpm spindle speeds. This is an expected result since tool point FRF is identified using chatter test results performed at 8400 and 8450 rpm spindle speeds. Using the same modified stability diagram, chatter behavior of the cutting operation can be predicted accurately for 6300 rpm spindle speed as well.

In addition, modified stability diagram is recalculated using the tool point FRFs identified using experimental results obtained at 12500 and 12600 rpm spindle speeds. Predictions obtained using modified stability and experimental results are also given in Table 5-18.

Table 5-18 Actual values of the chatter frequency and axial depth of cut and predicted values by modified stability diagrams.

Spindle Speed (rpm)	Predicted a_{lim} (mm)	Predicted chatter frequency ω_c (Hz)	Actual a_{lim} (mm)	Actual chatter frequency ω_c (Hz)
12500	0.75	1581	0.77	1574
12600	0.72	1585	0.72	1583

In this chapter a new identification procedure is proposed and applied on a real machining center for different holder – tool combinations. Identification results show that tool point FRF thus stability of the cutting operations is affected by spindle speed and cutting forces simultaneously depending on the holder – tool combinations. For the cases where tool mode is dominant, it is observed that tool point FRF is not affected by the rotating conditions. However, when stability of the cutting operation is determined by the spindle and holder modes, deviations due to rotational conditions becomes crucial. It is also observed that both spindle speed and cutting forces affect the tool point FRF and cause variations in the tool point FRF, thus on chatter stability.

CHAPTER 6

IDENTIFICATION OF BEARING DYNAMICS

During cutting operations gyroscopic moments and centrifugal forces cause variations in bearing dynamics. Although there exists speed dependent bearing models in literature, in machining centers bearings are located inside machining centers and speed dependent bearing characteristics are not supplied by the manufacturer. Even though bearing information is obtained from the manufacturer, after several years of operation bearing dynamic characteristics will not remain the same. Therefore, identification of speed dependent bearing dynamics plays a crucial role for the accurate prediction of machining stability.

6.1 Identification of Bearing Parameters at Idle State

In order to identify bearing parameters at idle state, the holder - tool combination given in Table 5-2 and Table 5-3 is used as a case study and it is clamped to 5 axis machining center. Spindle dimensions of the machining center are given in Table 6-1. Then, tool point FRFs in x and y directions are obtained using impact testing.

Table 6-1 Spindle Dimensions

Segment number	1	2	3	4	5	6	7	8	9
Length (mm)	32	16	22	45	78	279	20	16	66
Outer Diameter (mm)	80	80	80	80	90	75	64	60	55
Inner Diameter (mm)	45	40	35	30	27	41	31	31	31

In addition to experimentally obtained tool point FRFs, spindle – holder – tool assembly is modeled for the idle state using analytical modeling procedure given in Chapter 2. Note that in order to obtain tool point FRF analytically, bearing and interface parameters should be determined. Since there does not exist any analytical model for the interface parameters and bearing are located inside the machining center, these parameters are determined experimentally. For that purpose, first, tool point FRF in x direction is calculated with the interface and bearing parameters given in Table 6-2 and Table 6-3. Then, calculated tool point FRF is taken as an initial estimate and by manually tuning the analytically obtained tool point FRFs with respect to experimentally obtained tool point FRFs interface parameters and bearing parameters are identified. Identified interface parameters and bearing parameters in x direction are given in Table 6-4 and Table 6-5, respectively. Calculated tool point FRF is given in Figure 6-1 with the experimentally obtained tool point FRF.

Table 6-2 Initial estimates of the interface parameters for x direction

	Translational Stiffness (N/m)	Rotational Stiffness (N.m/rad)	Translational Damping (N.s/m)	Rotational Damping (N.m.s/rad)
Spindle–holder interface	5×10^7	1×10^6	10	22
Holder – tool interface	5×10^7	1×10^6	10	10

Table 6-3 Initial estimates of the bearing parameters for x direction

	Translational Stiffness (N/m)	Rotational Stiffness (N.m/rad)	Translational Damping (N.s/m)	Rotational Damping (N.m.s/rad)
Front bearing	5×10^6	1×10^6	1000	10
Rear bearing	5×10^7	1×10^6	1000	10

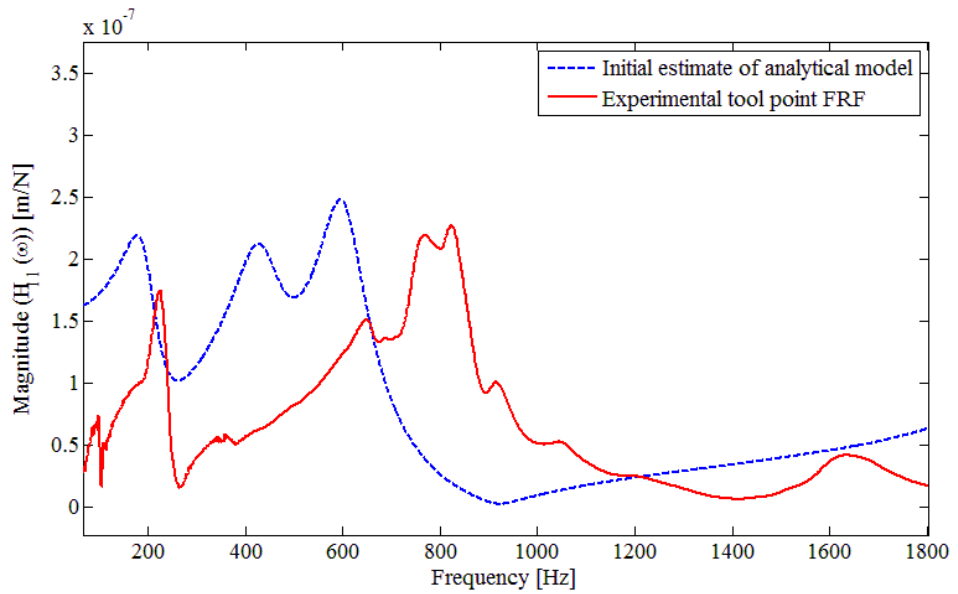


Figure 6-1 Tool point FRF in the x direction for the idle state obtained using impact testing and initially estimated interface parameters and bearing parameters.

Table 6-4 Dynamic properties of the interfaces in x direction.

	Translational Stiffness (N/m)	Rotational Stiffness (N.m/rad)	Translational Damping (N.s/m)	Rotational Damping (N.m.s/rad)
Spindle–holder interface	7.6×10^7	1.6×10^6	100	220
Holder – tool interface	8.2×10^7	1.5×10^6	100	100

Table 6-5 Dynamic properties of the bearings in x direction.

	Translational Stiffness (N/m)	Rotational Stiffness (N.m/rad)	Translational Damping (N.s/m)	Rotational Damping (N.m.s/rad)
Front bearing	9.6×10^6	7.6×10^6	3500	10
Rear bearing	4.55×10^7	1.6×10^6	2600	40

Similarly, interface and bearing parameters in y direction are identified by manually tuning the analytically obtained tool point FRFs with respect to experimentally obtained tool point FRFs in y direction. Identified interface and bearing parameters are given in Table 6-6 and Table 6-7, respectively.

Table 6-6 Dynamic properties of the interfaces in y direction.

	Translational Stiffness (N/m)	Rotational Stiffness (N.m/rad)	Translational Damping (N.s/m)	Rotational Damping (N.m.s/rad)
Spindle–holder interface	12.6×10^7	1×10^6	50	170
Holder – tool interface	8×10^7	1.5×10^6	100	100

Table 6-7 Dynamic properties of the bearings in y direction.

	Translational Stiffness (N/m)	Rotational Stiffness (N.m/rad)	Translational Damping (N.s/m)	Rotational Damping (N.m.s/rad)
Front bearing	1.45×10^6	3.83×10^6	3500	10
Rear bearing	1.02×10^8	1.5×10^6	1000	10

Analytically obtained tool point FRFs in x and y directions (by using identified interface and bearing parameters) are shown in Figure 6-2 and Figure 6-3, respectively, together with the experimentally obtained tool point FRFs.

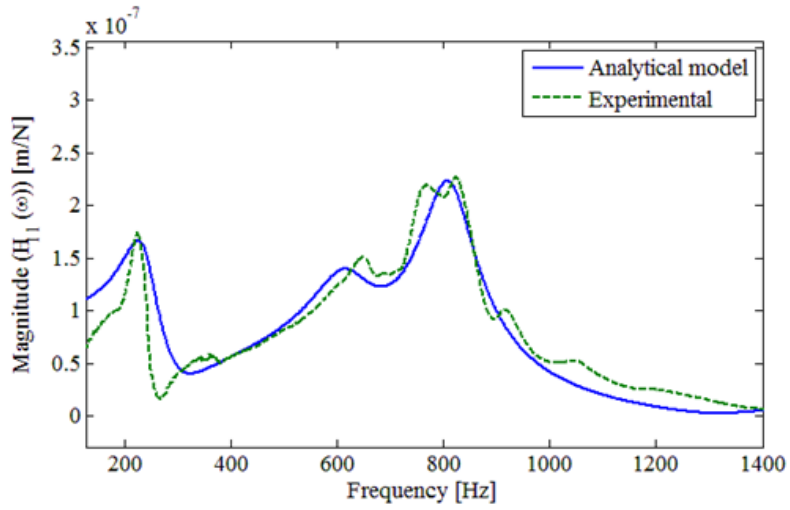


Figure 6-2 Analytically and experimentally obtained tool point FRFs in the x direction for the idle state.

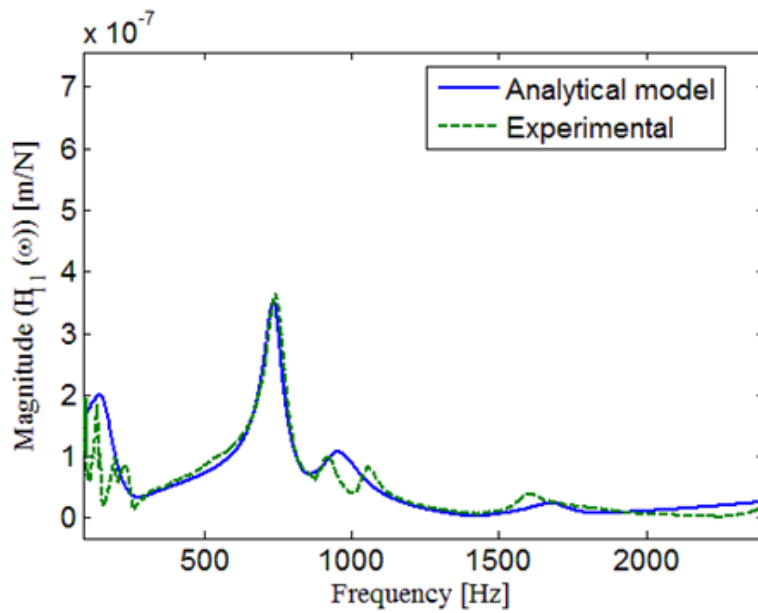


Figure 6-3 Analytically and experimentally obtained tool point FRFs in the y direction for the idle state.

6.2 Identification of Contact Parameters

Accurate identification of contact dynamics is very crucial in predicting the dynamic behavior and chatter stability of spindle-tool assemblies in machining centers. The stiffness and damping parameters of these critical interfaces affect the prediction of chatter frequencies and depth of cut limits, respectively. Contact parameters at the spindle – holder and holder – tool interfaces can be obtained by manually tuning the analytically obtained tool point FRFs with respect to experimentally obtained tool point FRFs as given in previous section. In addition to this approach, contact parameters can be identified using closed form method proposed by Orkun et al. [61, 62]. In this identification method, elastic receptance coupling equations previously used for coupling the system components (spindle, holder and tool) are rearranged to give the complex stiffness matrix at the holder-tool and spindle-holder interfaces in a closed-form manner as follows [61, 62]:

$$[K_{sh}] = \left[\left[[H_{12}]^{-1} \left[[H_{11}] - [SH_{11}] [H_{21}]^{-1} \right]^{-1} - [H_{22}] - [S_{11}] \right] \right]^{-1} \quad (6.1)$$

$$[K_{ht}] = \left[\left[[T_{12}]^{-1} \left[[T_{11}] - [SHT_{11}] [T_{21}]^{-1} \right]^{-1} - [T_{22}] - [SH_{11}] \right] \right]^{-1} \quad (6.2)$$

In order to identify contact parameters using the proposed method, right hand sides of Equation (6.1) and Equation (6.2) should be determined. In these equations, holder, tool and spindle receptances can be obtained analytically. In addition, receptances of spindle – holder ($[SH_{11}]$) and spindle – holder – tool ($[SHT_{11}]$) assemblies can be obtained experimentally.

For the spindle – holder – tool assembly receptance matrix, the first element of the matrix which is H_{11}^{sh} can be obtained by performing impact testing. But the remaining receptances cannot be obtained due to the difficulty in measuring

angular displacements and exciting the system with moment. Therefore, approximate methods are applied for determining the Rotational Degree of Freedom (RDOF) related receptances L_{11}^{sh} , N_{11}^{sh} and P_{11}^{sh} [61,62]. As it is shown that proposed identification method is highly sensitive to the noise in measured FRF data, it is suggested to identify the dynamical contact parameters by taking the average of the parameters calculated using the data obtained at several frequencies at the mode which is most sensitive to contact dynamics.

Although the contact parameters identified by using this approach yield pretty accurate results, contact parameters should be identified for each holder – tool combinations and this will be time consuming due to test requirement for each combination. In order to eliminate experimental dependency, the method is extended further by using neural networks [63]. In this approach, neural networks are trained using identified contact parameters. Therefore, it is shown that by performing identification for limited sets of holder – tool combination, contact parameters can be predicted in a wide range of holder – tool combination and experimental dependency can be eliminated in contact parameter identification.

6.3 Effect of Bearing Dynamics on Tool Point FRF

As seen from the identification results given in Section 6.1, front and rear bearings have translational and rotational stiffnesses. Also, as shown in Chapter 5, only variation of the dominant mode that determines chatter stability can be identified using inverse stability solution procedure. Therefore, using the experimentally identified tool point FRFs under cutting conditions, only bearing parameters that affect the elastic mode can be determined accurately. Thus, before the identification of speed dependent bearing dynamics, effects of each bearing parameter on tool point FRF should be investigated.

In order to investigate the effects of bearing dynamics on tool point FRF, first spindle – holder – tool assembly given in Section 6.1 is modeled with the interface and bearing parameters given in Table 6-4 and Table 6-5. Then, front bearing translational stiffness value is decreased 30% and remaining parameters are kept constant. Obtained tool point FRF in x direction is given with the original tool point FRF in Figure 6-4.

As seen from Figure 6-4, variation of translational stiffness of front bearing affects the rigid body mode of the spindle and elastic modes that determine the stability are not affected. Therefore, front bearing translational stiffness values at idle state can be used and translational stiffness of front bearings can be eliminated in the identification procedure of speed dependent bearing dynamics.

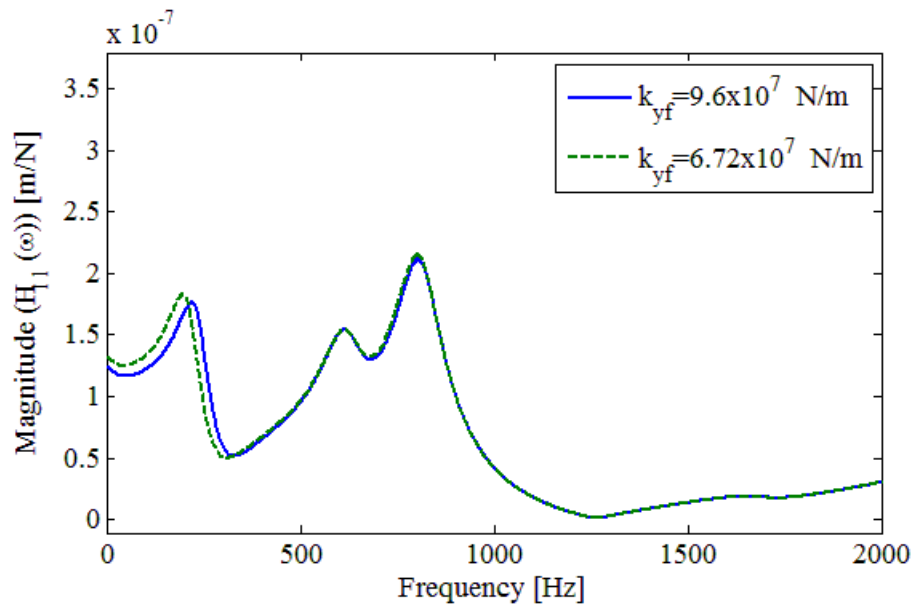


Figure 6-4 Effect of translational stiffness of front bearing on tool point FRF in x direction.

Similarly, in order to investigate the effect of front bearing rotational stiffness values on tool point FRF, corresponding stiffness value is decreased 70% and remaining parameters are kept the same as shown Table 6-4. Calculated tool point FRF in x direction is given with the original tool point FRF in Figure 6-5.

As seen from Figure 6-5, front bearing rotational stiffness does not affect the spindle rigid body mode and mainly affect the elastic mode that determines the stability.

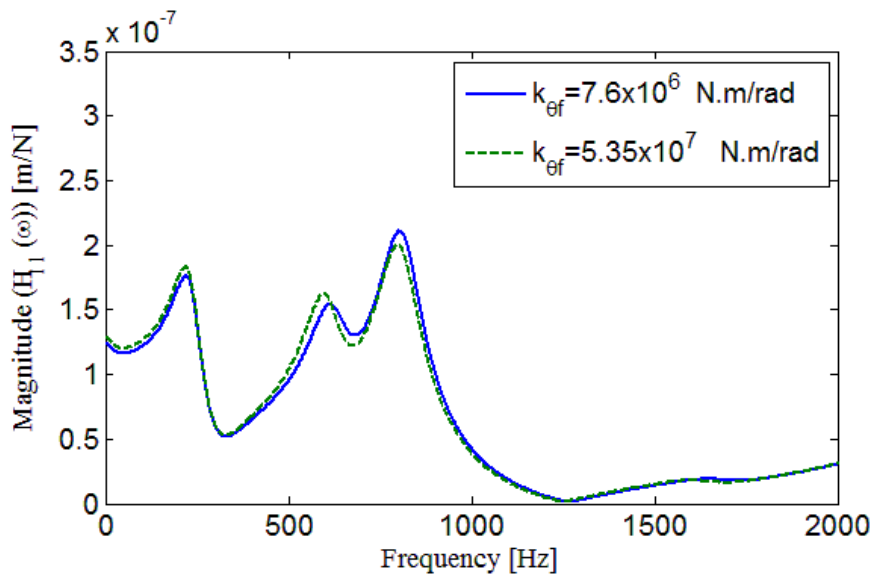


Figure 6-5 Effect of rotational stiffness values of front bearing on tool point FRF in x direction.

In addition to front bearing dynamic properties, effect of rear bearing dynamics on tool point FRF is investigated in a similar manner. First, effect of translational stiffness of rear bearing is investigated by decreasing the stiffness 30 % while keeping remaining parameters the same as shown in Table 6-4.

Then, rotational stiffness of rear bearing is examined similarly and the results obtained are given in Figure 6-6 and Figure 6-7.

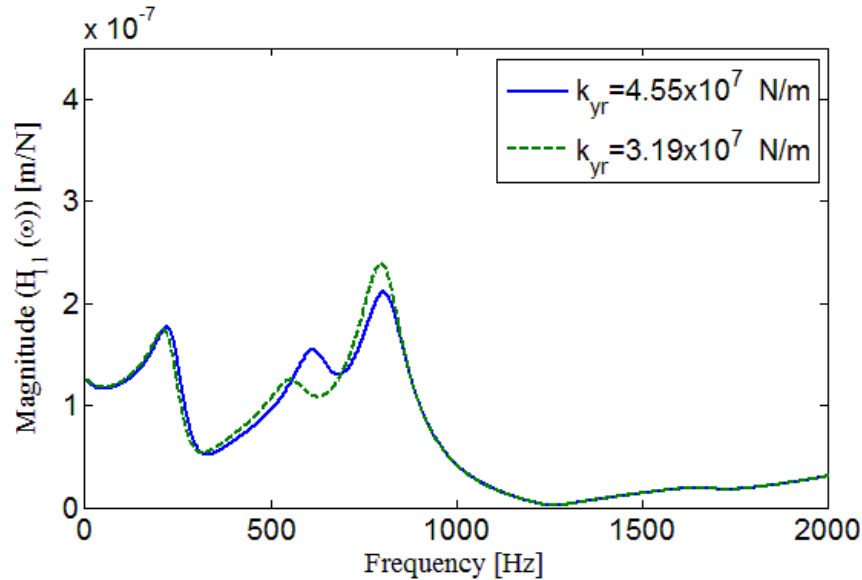


Figure 6-6 Effect of translational stiffness values of rear bearing on tool point FRF in x direction.

Effect analysis results show that, variation of the front bearing rotational stiffness and rear bearing translational stiffness affects the elastic mode and for the accurate prediction of chatter stability during cutting operation, speed dependent dynamics of these bearing parameters should be identified.

Note that effect analysis results are valid for the case studied. For different holder – tool combinations and machining centers, effect of each bearing parameter on tool point FRF should be investigated carefully. In cases where different effects are observed, identification method suggested in this study

should be performed and bearing parameters that affect tool point FRF and cutting stability should be identified.

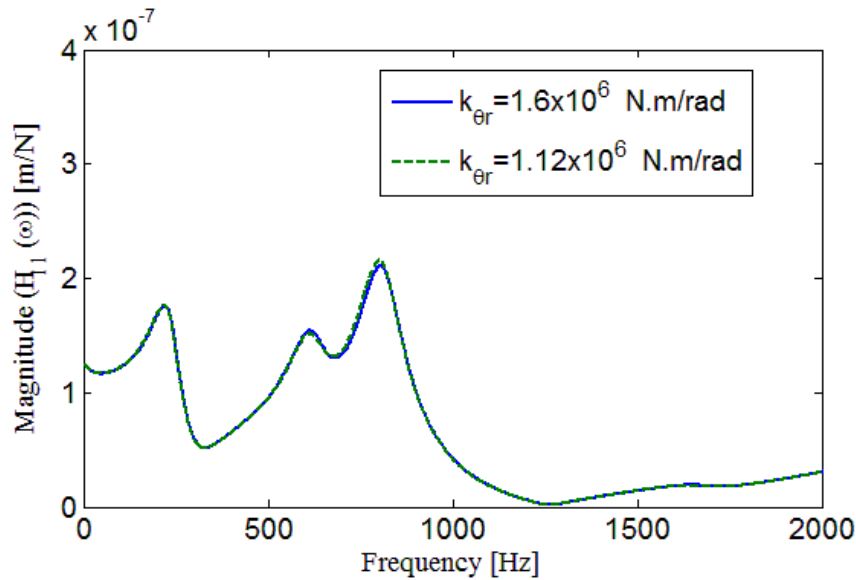


Figure 6-7 Effect of rotational stiffness values of rear bearing on tool point FRF in x direction.

6.4 Identification of Bearing Dynamics under Operational Conditions

In addition to identified bearing parameters and analytically determined tool point FRFs for idle state of the machining center, speed dependent bearing parameters are identified using experimentally identified in process tool point FRFs. Identification of speed dependent bearing parameters is performed by manually tuning analytically obtained tool point FRF. Identified bearing stiffness values for x and y directions are given in Table 6-8 and Table 6-9, respectively.

As seen from identification results given in Table 6-8 and Table 6-9, bearing stiffness values decrease with increasing spindle speed as expected. For instance, at 14000 rpm spindle speed bearing stiffness values decreases to 40 % of the idle values.

Table 6-8 Identified speed dependent bearing stiffness values in x direction.

	Idle state	6400 rpm	7500 rpm	14000 rpm
Front Bearing Rotational Stiffness (N.m/rad)	7.65×10^6	5.73×10^6	5.12×10^6	3.21×10^6
Rear Bearing Translational Stiffness (N.m/rad)	4.55×10^7	3.41×10^7	3.05×10^7	1.91×10^7

Table 6-9 Identified speed dependent bearing stiffness values in y direction.

	Idle state	6400 rpm	7500 rpm	14000 rpm
Front Bearing Rotational Stiffness (N.m/rad)	3.83×10^6	3.06×10^6	2.98×10^6	2.22×10^6
Rear Bearing Translational Stiffness (N.m/rad)	1.02×10^8	0.816×10^8	0.805×10^8	0.55×10^8

Afterwards, using identified speed dependent bearing parameters, tool point FRFs are recalculated. As an example, analytically determined tool point FRFs for x and y directions for idle state and 6400 rpm spindle speed are given in Figure 6-8 and Figure 6-9, respectively. Also note that, analytically determined tool point FRF for 6400 rpm spindle speed contains both gyroscopic effects and bearing stiffness variations.

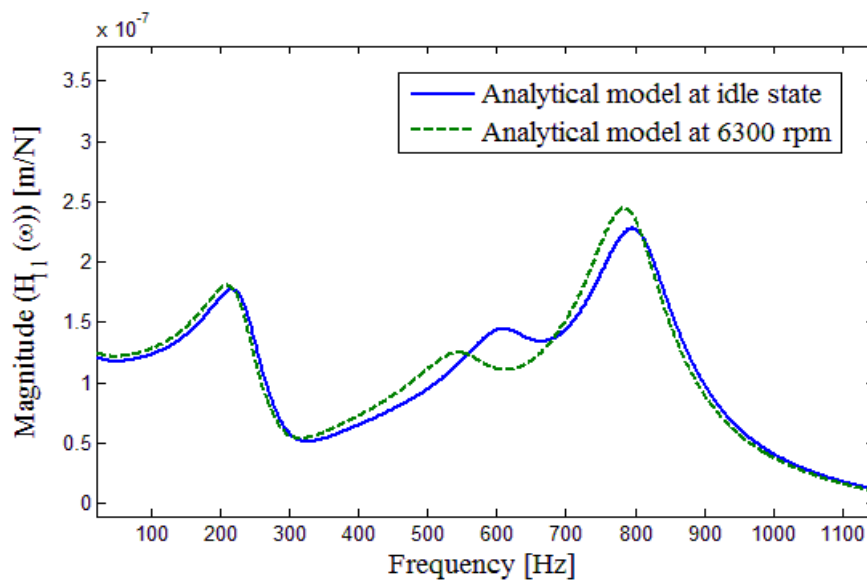


Figure 6-8 Analytically determined tool point FRFs in x direction for idle state and 6400 rpm spindle speed.

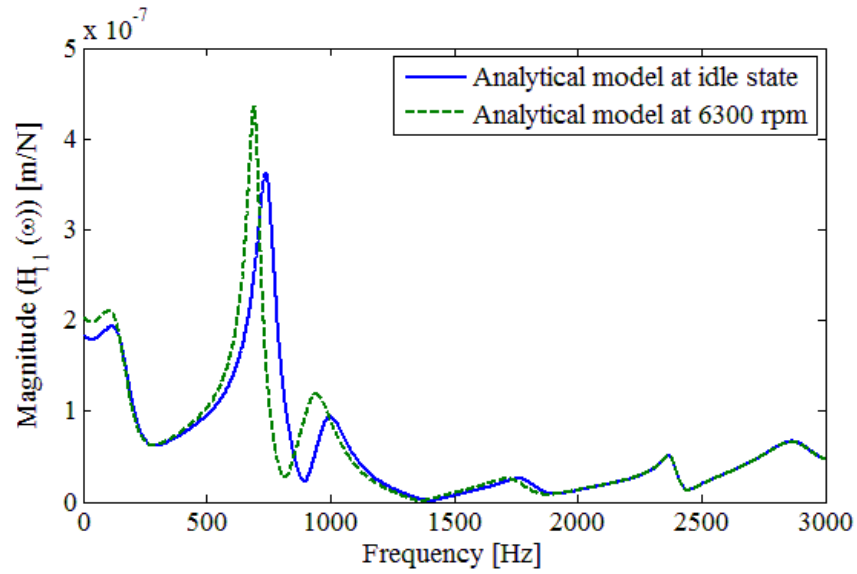


Figure 6-9 Analytically determined tool point FRFs in y direction for idle state and 6400 rpm spindle speed.

In order to check the accuracy of stability prediction, stability diagrams are calculated for machining of aluminum 7075 with 100% radial immersion. Calculated stability diagrams are given in Figure 6-10 with the actual chatter test results presented in Section 5.2.2.1.

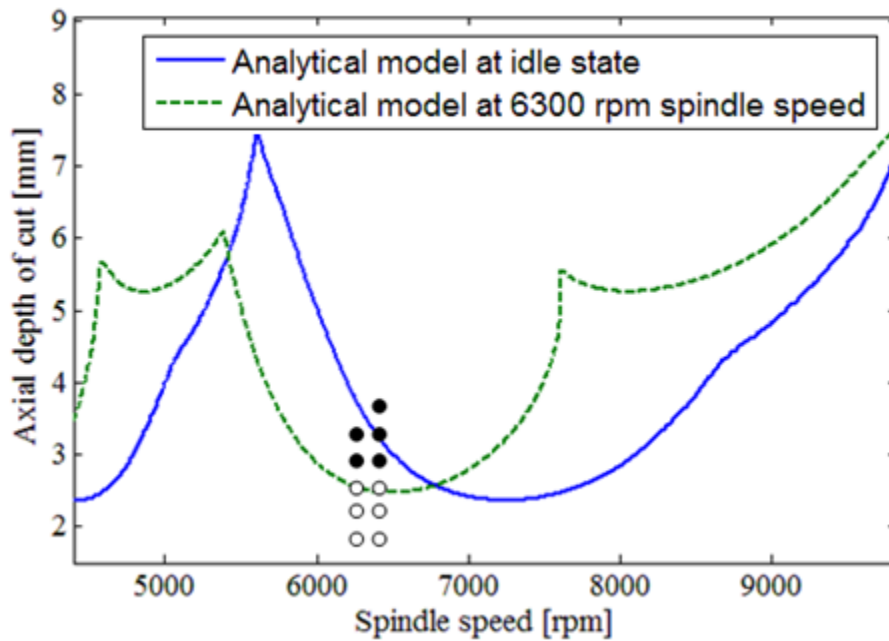


Figure 6-10 Analytically obtained stability diagrams for idle state, 6300 rpm spindle speed and chatter test results.

Similarly, tool point FRF is calculated analytically for 7500 rpm and 14000 rpm spindle speeds using the corresponding identified speed dependent bearing parameters, and stability diagrams are determined using analytically obtained tool point FRFs. Obtained stability diagrams are given in Figure 6-11 and Figure 6-12 with the chatter test results.

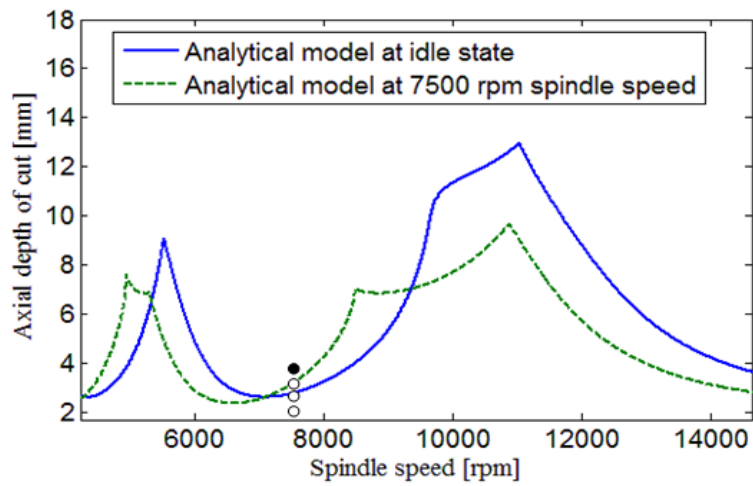


Figure 6-11 Analytically obtained stability diagrams for idle state, 7500 rpm spindle speeds and chatter test results.

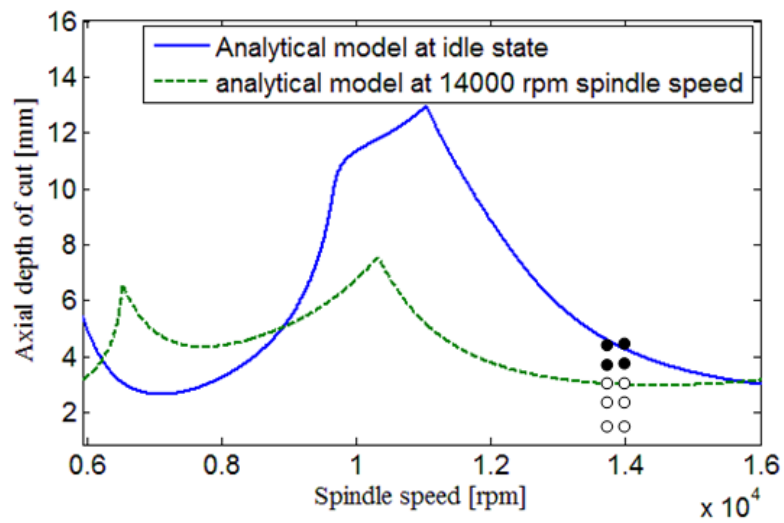


Figure 6-12 Analytically obtained stability diagrams for idle state, 14000 rpm spindle speeds and chatter test results.

As seen from stability predictions given in Figure 6-10 - Figure 6-12, using the identified speed dependent bearing parameters, actual stability of the cutting operation can be predicted analytically. In addition to the given stability diagrams, predicted axial depth of cut at limit and chatter frequencies for various spindle speeds are given in Table 6-10 with the actual chatter test results.

Table 6-10 Actual values of the chatter frequency and axial depth of cut at limit and predicted values by in process FRFs and idle FRFs.

Spindle Speed (rpm)	Predicted a_{lim} (mm) using idle FRF	Predicted a_{lim} (mm) using in process FRF	Predicted chatter frequency ω_c (Hz) using in process FRF	Actual a_{lim} (mm)	Actual chatter frequency ω_c (Hz)
6200	4	2.73	694	2.65	694
6300	3.6	2.61	696.5	2.6	697
7400	2.39	2.9	726	2.8	727
7500	2.42	3.1	728.5	3.1	728
14000	4.45	2.98	616	3	616

Note that stability diagrams given in Figure 6-10 - Figure 6-12 are valid in the vicinity of the corresponding spindle speeds only. Tool point FRFs are recalculated for 100 rpm spindle speed increments in 6000 rpm – 14500 rpm spindle speed band and limiting axial depth of cut at each spindle speed is determined. Then, complete stability diagram which is valid for all spindle

speeds is obtained by combining the calculated limiting axial depth of cut and spindle speed pairs. Obtained stability diagram is given in Figure 6-13 with the stability diagrams valid only at 6300 rpm and 14000 rpm spindle speeds.

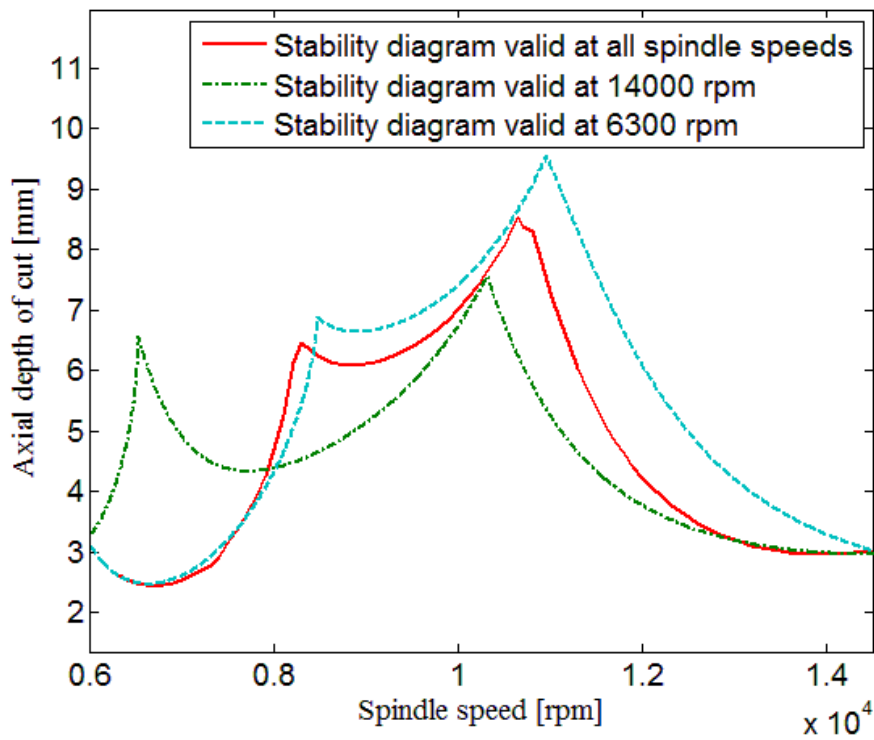


Figure 6-13 Stability diagram calculated using tool point FRF at 6300 rpm spindle speed, 14000 rpm spindle speed and combined stability diagram valid at all spindle speeds.

As seen from Figure 6-13, stability diagram calculated for 6300 rpm spindle speed over estimates stability limit at higher spindle speeds. Similarly, stability limit calculated for 14000 rpm spindle speed over estimates stability limit at lower spindle speeds. However, combined stability diagram shows actual

stability behavior of the cutting operation and can be used in stability prediction for all spindle speeds. Moreover, combined stability diagram is given in Figure 6-14 with the stability diagram obtained using tool point FRF at idle state.

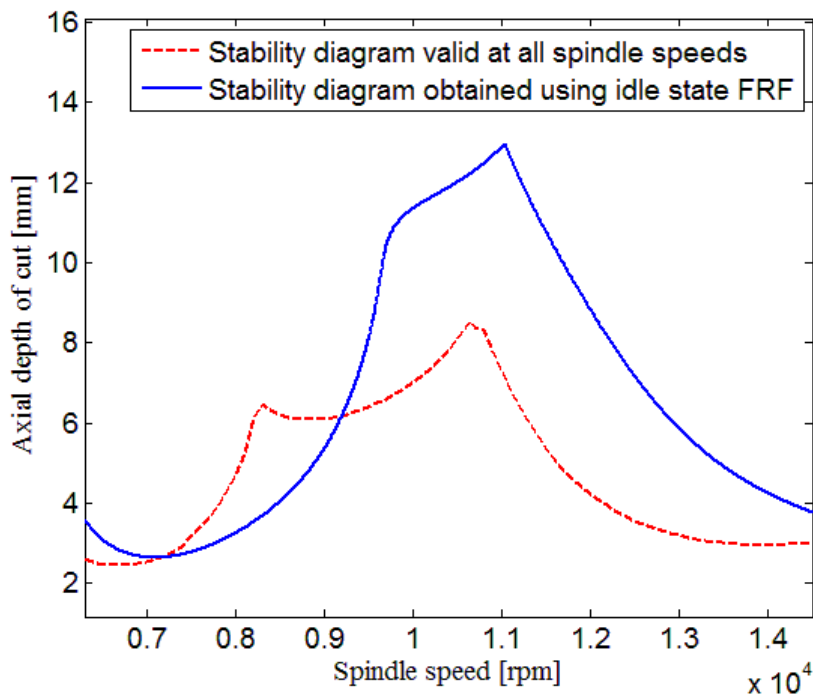


Figure 6-14 Stability diagram calculated using tool point FRF at idle state and combined stability diagram valid at all spindle speeds.

In addition to identified bearing dynamics with varying spindle speed, bearing stiffness values are identified at 7500 rpm spindle speed for different feed values using the chatter test results given in Section 5.2.2.2. Identified bearing parameters in x and y directions are given in Table 6-11 and Table 6-12, respectively.

Table 6-11 Identified force dependent bearing stiffness values in x direction.

	0.1 mm/tooth	0.16 mm/tooth	0.2 mm/tooth
Front Bearing Rotational Stiffness (N.m/rad)	5.12×10^6	4.44×10^6	4.21×10^6
Rear Bearing Translational Stiffness (N.m/rad)	3.05×10^7	2.78×10^7	2.55×10^7

Table 6-12 Identified force dependent bearing stiffness values in y direction

	0.1 mm/tooth	0.16 mm/tooth	0.2 mm/tooth
Front Bearing Rotational Stiffness (N.m/rad)	2.98×10^6	2.72×10^6	2.6×10^6
Rear Bearing Translational Stiffness (N.m/rad)	8.05×10^7	7.75×10^7	7.24×10^7

As seen from Table 6-11 and Table 6-12, with increasing feed bearing stiffness values decrease. Identification results show that, in addition to spindle rotational speed, bearing dynamics is also affected by forces acting on the system.

In this chapter, bearing parameters under operational conditions are investigated. First, bearing parameters at idle state are identified using

experimentally obtained tool point FRFs and analytical model suggested. Then, effect of translational and rotational stiffness values of front and rear bearings on tool point FRF is analyzed. Results show that, variation of the front bearing rotational stiffness and rear bearing translational stiffness affect the dominant elastic mode for the case studies. Finally, using effect analysis results bearing parameters that affect dominant mode of the tool point FRF are identified at various spindle speeds and feed values. Identification results show that bearing parameters decrease with increasing spindle speed and cutting forces that excite the system.

CHAPTER 7

EXPERIMENTAL VERIFICATION AND CASE STUDIES

In this chapter, verification of the analytical modeling procedure and identification methods is performed. For that purpose, holder – tool combination which was not used in the identification procedure is clamped to the machining center and the tool point FRF is calculated using the analytical model suggested along with the previously identified bearing parameters. Then, stability diagrams are calculated and accuracy of the predicted stability diagrams is investigated with chatter tests. In addition, variations of the tool point FRF and stability are investigated for a dominant tool mode case.

7.1 Case Study 1

In order to verify the analytical modeling procedure and identification methods, a 4-teeth carbide tool of 100 mm length and 25 mm diameter is clamped to the same machining center used in previous Chapters with a different holder which was not used in the identification procedure presented in Chapter 6. The overhang length of the tool is 56 mm and holder dimensions are given in Table 7-1.

First, tool point FRF is measured by impact testing at the idle state of the machining center. The tool point FRFs are also calculated using the analytical model suggested with the identified bearing and interface parameters which are given in Chapter 6. Calculated tool point FRFs in x and y directions are shown along with the experimentally obtained tool point FRFs in Figure 7-1 and Figure 7-2, respectively.

Table 7-1 Holder dimensions

Segment number	1	2	3	4	5	6
Length (mm)	25	10	90	16	6	10
Outer Diameter (mm)	63.5	50	63	48	64	55
Inner Diameter (mm)	25	25	10	10	10	10

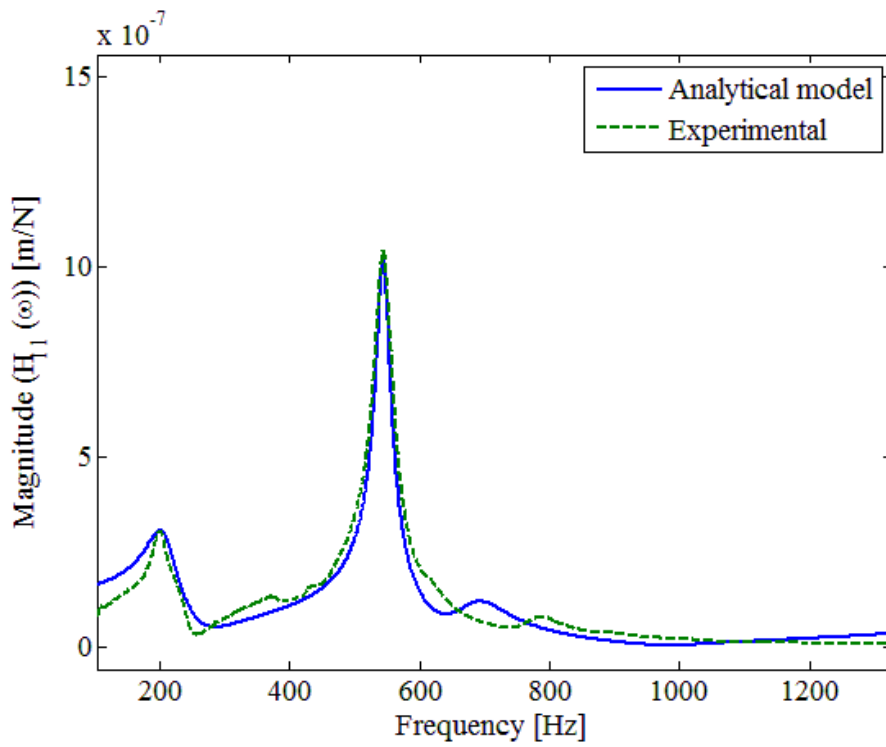


Figure 7-1 Analytically and experimentally obtained tool point FRFs in the x direction for the idle state.

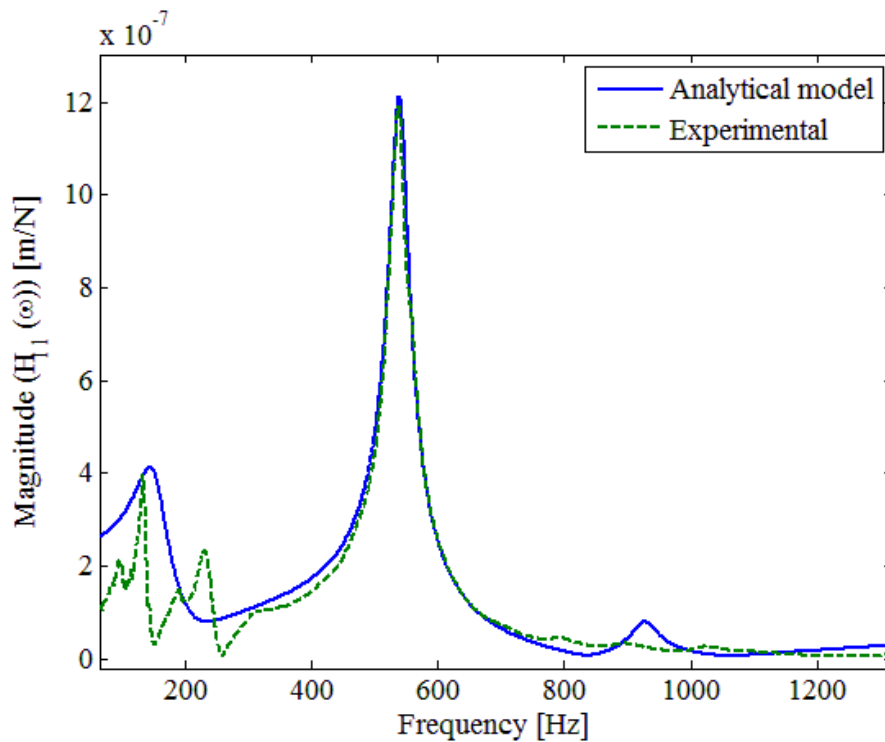


Figure 7-2 Analytically and experimentally obtained tool point FRFs in the y direction for the idle state.

As seen from Figure 7-1 and Figure 7-2, analytically and experimentally obtained tool point FRFs are in good agreement in the frequency band containing dominant mode at 550 Hz. Note that, bearing dynamics are not affected by holder and tool dimensions and remain the same as identified in Chapter 6. Not only bearing dynamics, but also the dynamics of the spindle – holder interface does not change when a different holder is clamped to the same machining center. Thus the same spindle – holder interface parameters can be used for different holder combinations. Finally, since spindle and holder elastic modes are not affected by the contact parameters at holder – tool interface, average values can be used for the holder – tool contact parameters. Thus in the analytical model, the previously identified interface and bearing parameters can be used, and tool point FRFs can be calculated analytically

without performing any experimental work. Theoretically calculated FRFs are given Figure 7-1 and Figure 7-2.

In addition to tool point FRFs at idle state of the machining center, tool point FRFs including gyroscopic effects and bearing stiffness variations at 6000 rpm and 7000 rpm spindle speeds are also calculated. Note that, the bearing stiffness values employed in the analysis for spindle speeds of 6300 rpm and 7500 rpm are the values identified in Chapter 6. For 6000 rpm and 7000 rpm spindle speeds, linear speed dependent variation is assumed for the bearing dynamics, and the corresponding bearing stiffness values are determined by applying interpolation. Obtained rotational tool point FRFs in x and y directions are given in Figure 7-3 and Figure 7-4, respectively.

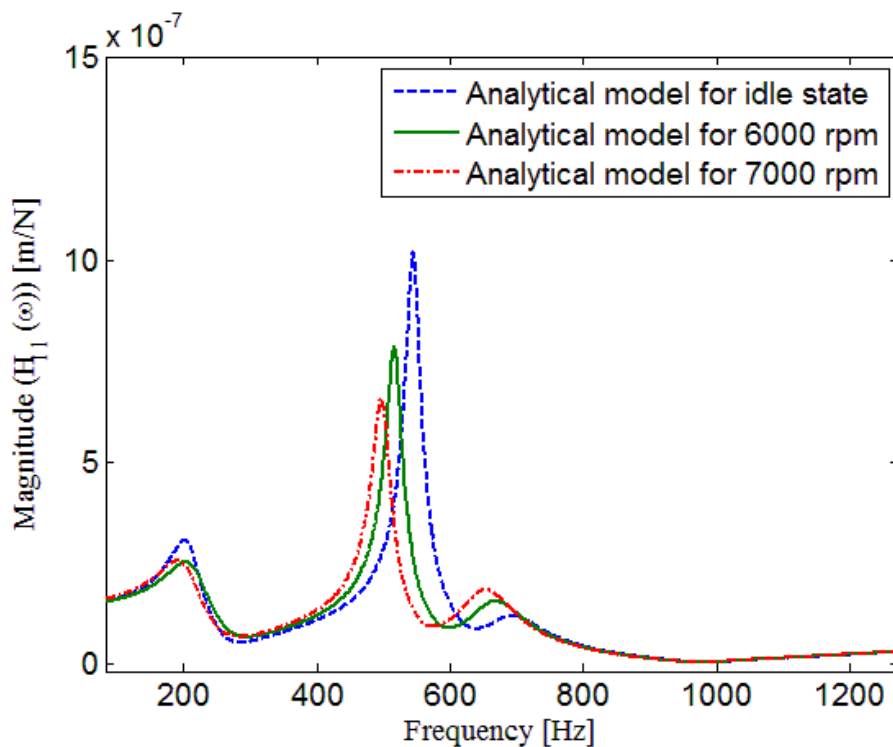


Figure 7-3 Analytically determined tool point FRFs in x direction for idle state, 6000 rpm and 7000 rpm spindle speeds.

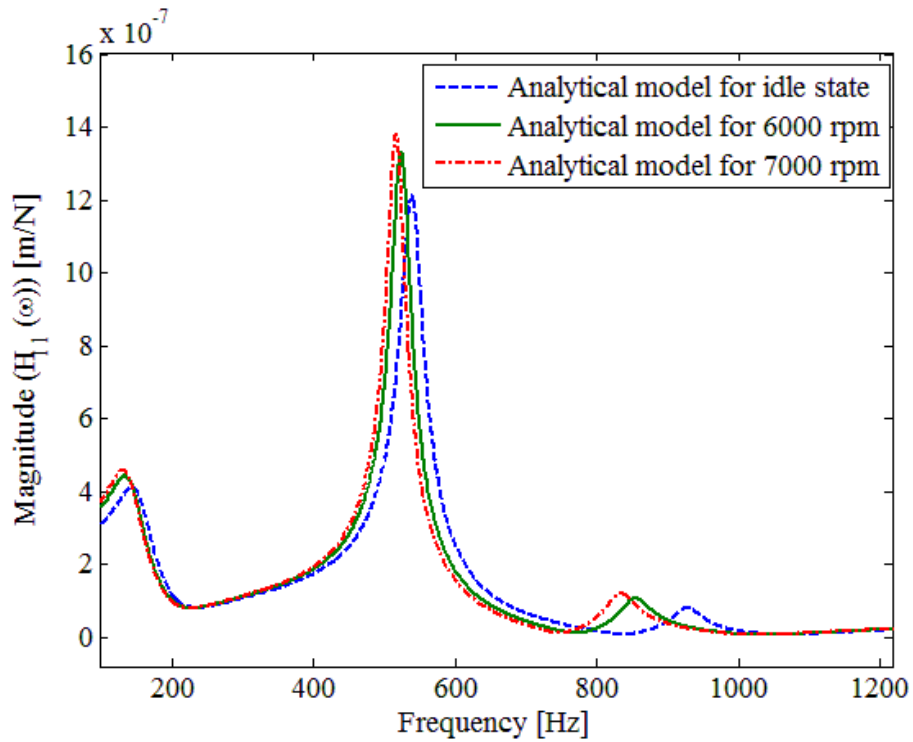


Figure 7-4 Analytically determined tool point FRFs in y direction for idle state, 6000 rpm and 7000 rpm spindle speeds.

In addition to calculated tool point FRFs, stability diagrams are calculated for machining of 7075 aluminum with 100 % radial immersion and 0.1 mm/tooth feed using the stability model proposed Budak and Altıntaş [5]. Finally, chatter tests are performed at 6000 rpm and 7000 rpm spindle speeds. Calculated stability diagrams both for idle FRFs and in process FRFs are given with the chatter test results in Figure 7-5 and Figure 7-6.

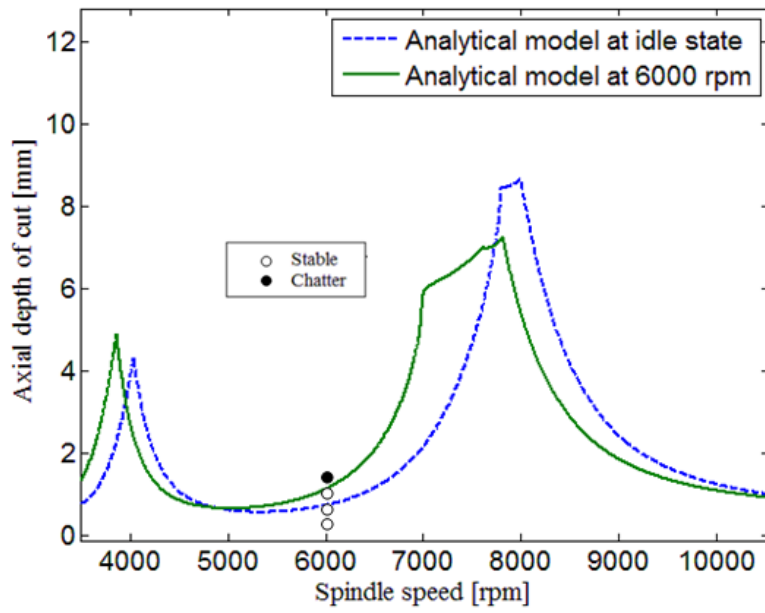


Figure 7-5 Analytically obtained stability diagrams for idle state, 6000 rpm spindle speed and chatter test results.

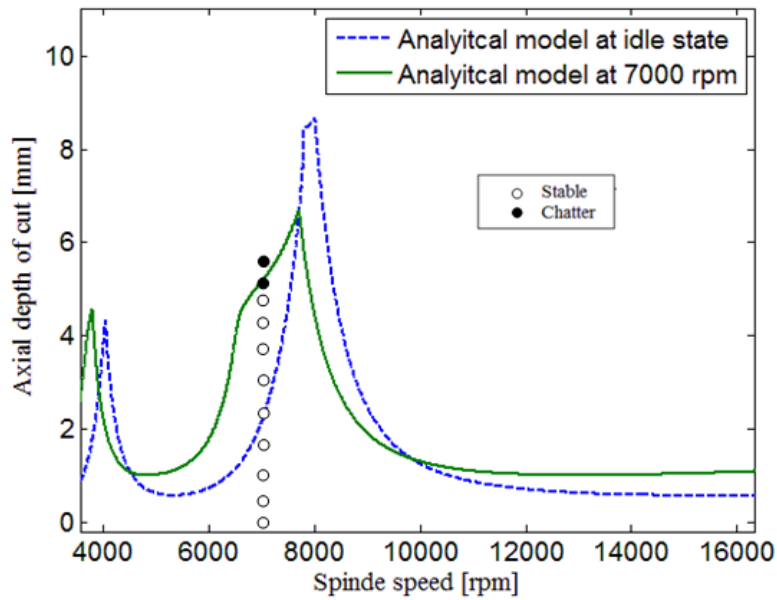


Figure 7-6 Analytically obtained stability diagrams for idle state, 7000 rpm spindle speed and chatter test results.

As seen from Figure 7-5 and Figure 7-6, actual stability of the cutting operation can be predicted much more accurately with the tool point FRFs including gyroscopic effects and bearing stiffness variations. For instance, at 6000 rpm spindle speed, predicted axial depth of cut using idle FRF is 0.74 mm. However; in actual cutting operation chatter occurred at 1.1 mm which can be predicted by using in process FRF is 1.13 mm. Similarly, at 7000 rpm spindle speed, predicted axial depth of cut using idle FRF is 2.17 mm. However; in actual cutting operation chatter occurred at 5 mm and it can be predicted as 5.15 mm by using in process FRF. Stability predictions using idle FRFs and in process FRFs are given in Table 7-2 with the actual stability of the cutting operation.

Table 7-2 Actual stability limit and stability predictions using idle FRFs and in process FRF

Spindle Speed (rpm)	Predicted a_{lim} (mm) using idle FRFs	Predicted a_{lim} (mm) using in process FRFs	Actual a_{lim} (mm)
6000	0.74	1.13	1.1
7000	2.17	5.15	5

Similar to the stability predictions given in Chapter 6, stability diagrams given in Figure 7-5 and Figure 7-6 are valid in the vicinity of the corresponding spindle speed only. Therefore, for the accurate prediction of actual stability of the cutting operation, tool point FRF should be recalculated at that operating

speed and the corresponding stability should be used before the machining operation.

7.2 Case Study 2

As shown in the previous section, variations in bearing dynamics due to changes in rotational speed cause deviations in the stability of the cutting operation. However; using analytical model suggested and identified bearing dynamics, actual stability of a cutting operation can be predicted accurately. In this section, holder – tool combinations for which the dominant tool mode determines the stability regions are analyzed. For that purpose, a 4-teeth carbide tool of 72 mm length and 12 mm diameter is clamped to the same machining center. The overhang length of the tool is 58 mm. Holder dimensions are given in Table 7-3.

Table 7-3 Holder dimensions

Segment number	1	2	3	4	5
Length (mm)	25	18	16	6	10
Outer Diameter (mm)	63.5	50	44	64	55
Inner Diameter (mm)	12	12	15	15	15

First, tool point FRF is measured by impact testing at the idle state of the machining center. Then by manually tuning the analytically obtained tool point FRFs, contact parameters at the holder – tool interface are identified and then the tool point FRF of the spindle – holder – tool assembly is calculated by using identified contact and bearing parameters. For the bearing dynamics and contact parameters at the spindle – holder interface, previously identified

values are used. Identified contact parameters in x and y directions are given in Table 7-4. Analytically obtained tool point FRFs for idle state in x and y directions are compared with the experimentally obtained tool point FRFs in Figure 7-7 and Figure 7-8, respectively.

Table 7-4 Contact parameters at holder – tool interface in x and y direction

Holder – tool interface	Translational Stiffness (N/m)	Rotational Stiffness (N.m/rad)	Translational Damping (N.s/m)	Rotational Damping (N.m.s/rad)
x direction	8.1×10^6	1×10^6	20	10
y direction	7.3×10^6	1×10^6	20	10

As seen from Figure 7-7 and Figure 7-8, unlike in the case study 1 given in Section 7.1, tool point FRF is dominated by the tool mode, and the spindle mode located at 1200 Hz will not have any contribution to stability of the cutting operation.

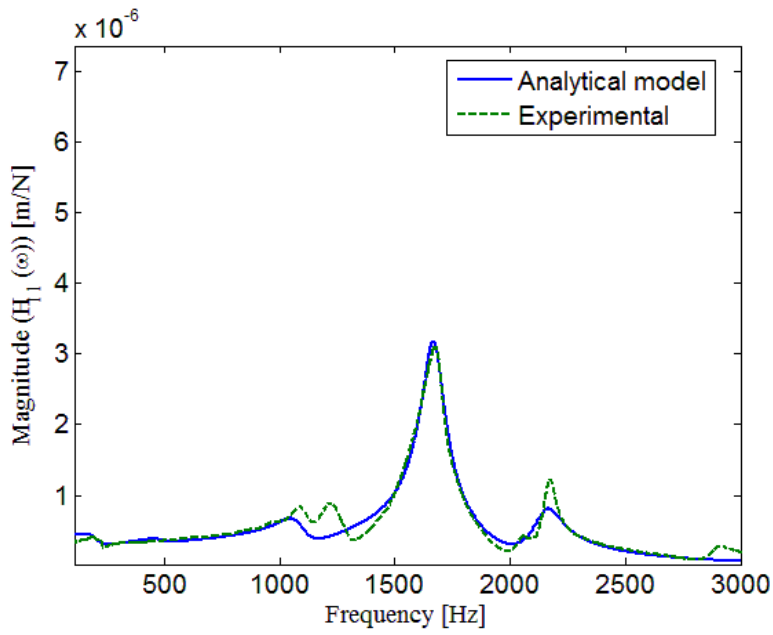


Figure 7-7 Analytically and experimentally obtained tool point FRFs in the x direction for the idle state.

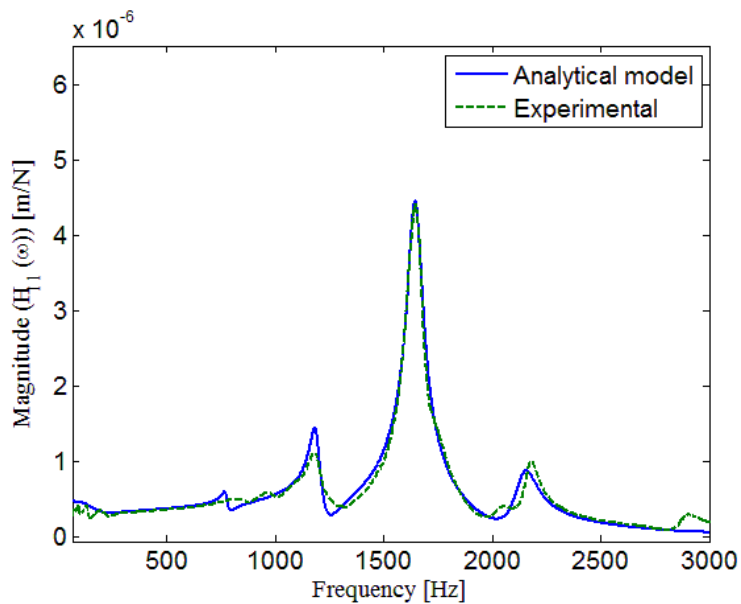


Figure 7-8 Analytically and experimentally obtained tool point FRFs in the y direction for the idle state.

Secondly, in order to investigate effect of rotational conditions on stability, gyroscopic moments and bearing stiffness variations are examined separately. First, tool point FRFs are calculated for idle state, 14000 rpm and 35000 rpm spindle speeds analytically with the same bearing parameters. Then, using analytically obtained tool point FRFs, stability diagrams are calculated for the machining of 7075 aluminum with 100 % radial immersion and 0.1 mm/tooth feed. Obtained stability diagrams are given in Figure 7-9.

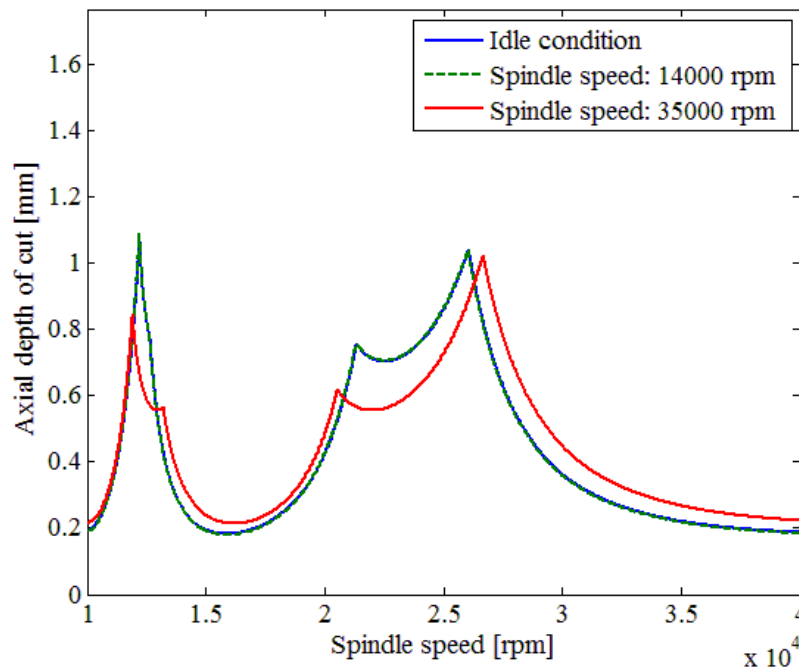


Figure 7-9 Stability diagrams predicted using the tool tip FRFs for idle state, 14000 rpm and 35000 rpm spindle speed (effects of operating speed on bearing dynamics are not considered).

As seen from Figure 7-9, at 14000 rpm, gyroscopic moments do not affect stability of the process and expected variations are observed at 35000 rpm spindle speed. Also note that, since same bearing parameters are used in tool point FRF calculations, observed deviations in Figure 7-9 are due to gyroscopic moments only.

In order to investigate the effects of bearing stiffness variations on tool point FRF, rear bearing translational stiffness values are decreased 70 % and remaining parameters are kept constant. Then, tool point FRF is calculated for the decreased and nominal values of the bearing parameters. Obtained tool point FRFs are given in Figure 7-10.

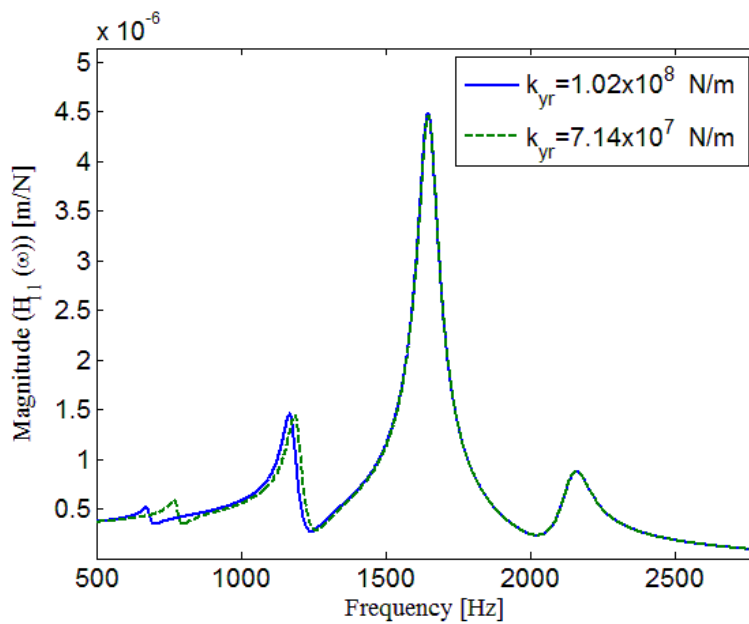


Figure 7-10 Effect of translational stiffness values of rear bearing on tool point FRF.

As shown in Figure 7-10, 70 % decrease in rear bearing translational stiffness value does not cause variations in the tool mode, and only spindle modes are affected by the bearing variations.

Similarly, in order to examine the effect of front bearing rotational stiffness on tool point FRF, corresponding stiffness value is decreased 70 % while keeping the remaining parameters constant, and tool point FRF is recalculated. Calculated tool point FRFs for both cases are given in Figure 7-11. As seen from Figure 7-11, front bearing rotational stiffness variations mainly effects spindle modes and there exist negligible change in the tool mode.

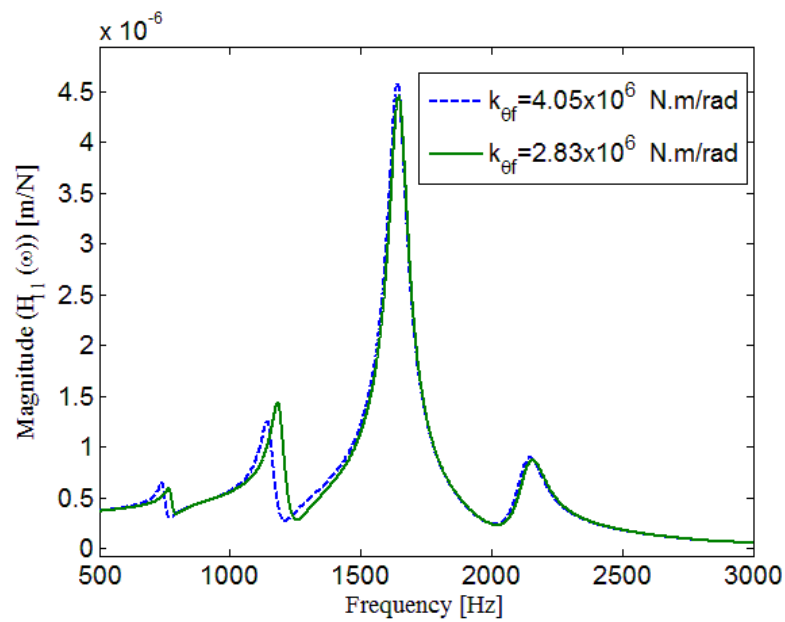


Figure 7-11 Effect of rotational stiffness values of front bearing on tool point FRF.

In addition to effect analysis given in Figure 7-9 - Figure 7-11, combined effects of gyroscopic moments and bearing stiffness variations are investigated. For that purpose, tool point FRF of the spindle – holder – tool assembly is calculated for 8500 rpm spindle speed with bearing stiffness values identified in Chapter 6 for that speed. Then using analytically obtained tool point FRFs, stability diagrams are calculated for the machining of 7075 aluminum with 100 % radial immersion and 0.1 mm/tooth feed. Calculated stability diagrams both for idle state and 8500 rpm spindle speed are given in Figure 7-12.

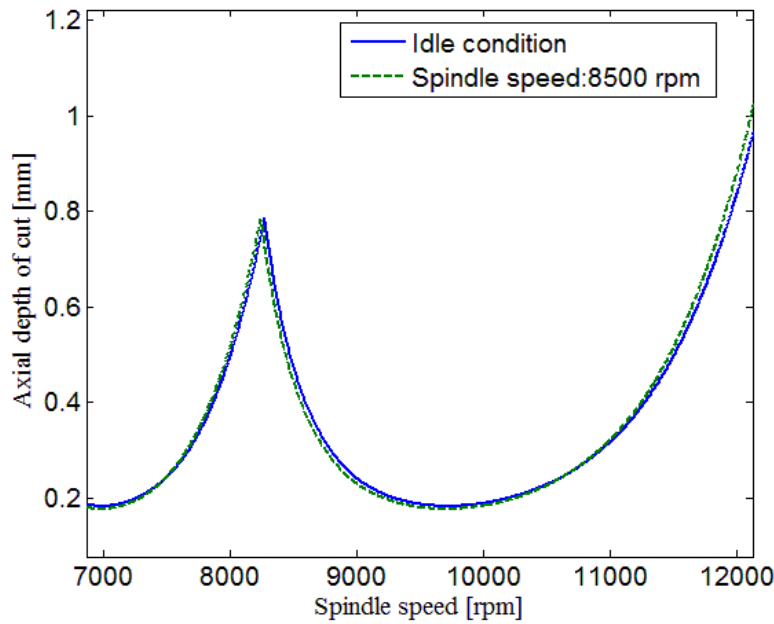


Figure 7-12 Stability diagrams predicted using the tool tip FRFs for idle state and 8500 rpm spindle speed with bearing stiffness variation effect.

As seen from Figure 7-12, since tool mode is not affected by the bearing variations as shown in Figure 7-10 and Figure 7-11, negligible variations are observed between stability diagrams obtained using idle and in process FRFs. Similarly, tool point FRFs are calculated for 12500 rpm spindle speed and stability diagram is calculated for in process FRFs. Obtained stability diagram is given in Figure 7-13 with the stability diagrams obtained using idle FRF. As seen from Figure 7-13, small deviations occur in the stability of the cutting operation for 12500 rpm spindle speed.

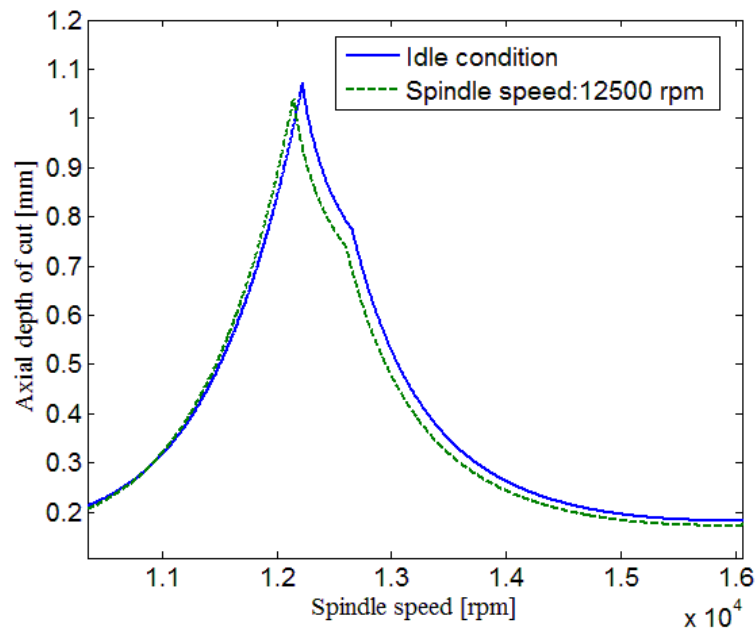


Figure 7-13 Stability diagrams predicted using the tool tip FRFs for idle state and 12500 rpm spindle speed with bearing variation effect.

In addition to calculated stability diagrams, chatter tests are performed and obtained results are given with the predicted axial depths of cut at limit using idle FRFs and in process FRFs in Table 7-5. As seen from Table 7-5, compared to case study 1, deviations between the actual stability and predicted stability using idle FRF is not crucial.

To sum up, as shown in case study 1, variation in the bearing stiffness values affects the spindle elastic modes and considerable deviations are occurred in the stability of the cutting operation when spindle modes are dominant in the tool point FRF. On the contrary, as shown in case study 2, when relatively thick end mill is clamped to machining center and tool point FRF is dominated by the tool mode, bearing stiffness variations have negligible effect on stability diagrams since tool mode is not affected by bearing dynamics. Therefore it can be concluded that, for the cases where spindle modes are dominant in the tool point FRF, modeling approach presented in this study should be employed and in process tool point FRFs including variations of the bearing dynamics should be calculated.

Table 7-5 Predicted and actual values of axial depth of cut.

Spindle Speed (rpm)	Predicted a_{lim} (mm) using idle FRF	Predicted a_{lim} (mm) using in process FRF	Actual a_{lim} (mm)
8500	0.48	0.47	0.49
12500	0.84	0.78	0.75
12600	0.79	0.75	0.76

CHAPTER 8

CONCLUSIONS

8.1 Conclusions

In this thesis, a complete analytical model for a machining center under operational conditions is presented by extending the previously developed model by Erturk et al. [37]. In addition to analytical model suggested, a new procedure is proposed for the identification of tool point FRF and bearing dynamics under operational conditions. Modeling approach developed and the numerical and experimental studies carried out in this thesis are summarized and major conclusions obtained are given in this section.

In machine tool studies high speed machining centers are generally modeled using FEM. However, in this study an alternative modeling procedure is suggested. In the model suggested, machining center subassemblies (spindle, holder and tool) are modeled using Timoshenko beam model including gyroscopic effects where tool point FRF is obtained by structural coupling and modification methods. The method proposed is verified by FEM using ANSYS. The results show that the method developed can provide highly accurate predictions with a considerable reduction in computational time. In addition to the accuracy and computational speed of the method proposed, the further advantage of using receptance coupling and modification techniques is demonstrated with a machine tool application in which modifications only in certain parts of the system are required. In such applications computational time is reduced drastically. For instance, with the method developed, tool point FRF is obtained 70 times faster compared to FEM as given in Chapter 2.

Using the analytical model proposed, variations of tool point FRF under operational conditions are investigated for different spindle – holder – tool assemblies. In the case studies, two main effects that result in tool point FRF variations due to operating conditions are examined. First, changes in the tool point FRF due to the gyroscopic effects are investigated. Second, the effects of bearing stiffness variation on the tool point FRFs are investigated. It is observed that, due to gyroscopic moments stability limits increase with increasing spindle speed. In addition, variations in bearing stiffness values affect stability diagram depending on the holder – tool combination. It is observed that, variation in the bearing stiffness values affects the spindle elastic modes and considerable deviations are occurred in the stability of the cutting operation when spindle modes are dominant in the tool point FRF. On the contrary when relatively thick end mill is clamped to machining center and tool point FRF is dominated by the tool mode, bearing stiffness variations have negligible effect on stability diagrams since the tool mode is not affected by bearing dynamics. Therefore it can be concluded that, for the cases where spindle modes are dominant in the tool point FRF, variations of the bearing dynamics due to operating conditions should be considered in the dynamic analysis and therefore in stability studies.

In addition to the analytical model developed, dynamics of a milling machine during operation is investigated experimentally, not only to verify analytical model developed, but also for the determination of the tool point FRF during cutting operation. In these experimental studies two different approaches are employed. First, the system dynamics is investigated with the examination of the input and output relation between cutting forces and the system response. In this approach, due to the measurement capability of the dynamometer, tool point FRF is determined for lower frequencies and elastic modes that determine the stability could not be identified. Also due to the noise problems at high spindle speeds, tool point FRFs could not be identified above 2000 rpm spindle speed. In the second approach, a new identification procedure is proposed which is called inverse stability solution procedure. In this method,

experimentally determined chatter frequency and corresponding axial depth of cut are used in order to identify tool point FRF. Identification method suggested is applied to a real machining center and it is shown that tool point FRF can be accurately identified with the method proposed. Moreover, it is observed that, both spindle rotational speed and cutting forces cause variations in tool point FRF. In addition to the success of the proposed method in tool point FRF identification, it has the advantage of eliminating the necessity of using expensive equipments such as dynamometer and laser vibrometer. The method suggested requires impact testing equipment for the idle FRF measurement and a simple microphone for the detection of chatter frequency and limit value of axial depth of cut.

As shown in numerical case studies presented in Chapter 3, variations of the bearing dynamics under cutting conditions should be included in the analysis for accurate prediction of the stability. In machining centers bearings are located inside the machining centers and speed dependent bearing characteristics are not supplied by the manufacturer. Even if the bearing information is obtained from the manufacturer, after several years of operation the dynamic characteristics will not remain the same. Therefore, identification of bearing dynamics plays a crucial role for the accurate prediction of machining stability. In this thesis, using the identified tool point FRFs under cutting conditions and employing the analytical model suggested, speed and force dependent bearing stiffness values are identified. Regarding the bearing stiffness identification, the observed variations in the dynamic behavior are attributed to the changes in the bearing parameters assuming that contact dynamics at the spindle – holder interface are not affected by the cutting conditions. Identification results show that bearing stiffness values decrease with increasing spindle speed and increasing cutting forces.

Finally, it is shown that experimentally identified spindle – holder interface parameters and speed dependent bearing dynamics can be used in modeling different holder – tool combinations in the same machining center. Therefore,

with the implementation of identified speed dependent bearing characteristics to the analytical model, stability of high speed cutting operations can be predicted accurately before cutting operations, which was the primary objective of this thesis.

The contribution of this study to the literature can be summarized as follows:

First, an alternative modeling procedure is suggested for the tool point FRF calculation including gyroscopic moments. In analytical model proposed, instead of applying FEM, sub-segment Frequency Response Functions (FRFs) are obtained analytically and sub-segment FRFs obtained are coupled by using receptance coupling method. Unlike existing approaches, machining center is modeled using symmetric beam elements with free-free end conditions regardless of the actual boundary conditions, and bearing properties are included into system dynamics by employing structural modification techniques. Thus, response of the system under operating conditions is obtained by using symmetric beam elements by reducing the computational cost drastically, without losing accuracy.

Second, using analytical model developed, effects of gyroscopic moments and bearing stiffness variations are investigated with numerical examples which give better insight in machine tool dynamics under operational conditions.

Third, a new identification procedure is proposed for the in process tool point FRF identification. In identification method developed, in process FRFs are identified using experimentally obtained axial depth of cuts and chatter frequencies. Using identification method developed the necessity of expensive equipments, complicated experimental setups and signal processing problems are eliminated. Moreover, stability diagrams are recalculated using identified in process FRFs and it is shown that deviations in stability of the machining operations can be predicted much more accurately by using identified in process FRFs.

Fourth, bearing dynamics of a machining center under operating conditions are identified for the first time in the literature. It is shown that bearing dynamics is affected by spindle rotational speed and cutting forces that excite the machining center. Using identification method developed, bearing dynamics under various spindle speeds and cutting forces is identified. Furthermore, using analytical model suggested and identified speed dependent bearing stiffness values, stability diagram which is valid at all spindle speeds is calculated. This is the first time in the literature that complete stability diagram including effects of gyroscopic moments and bearing stiffness variations is theoretically obtained and experimentally verified.

Finally, a different holder – tool combination is clamped to same machining center and it is shown that tool point FRF of the new assembly can be predicted by using the analytical model proposed and the previously identified bearing dynamics, without performing further experiments. Therefore, experimental dependency is eliminated in stability predictions. In addition, it is shown that when spindle modes are dominant, the stability of the machining operation is affected by bearing stiffness variations. On the contrary, when the tool is the most flexible component in the machining center, negligible variations occur in the stability due to bearing stiffness variation. These conclusions enable researchers and machine shop operators to understand the underlying cause of frequently observed and unexpected deviations in stability of the machining operations.

The outcome of the thesis is believed to help increasing not only the accuracy of chatter stability predictions, but also better understanding of machine tool dynamics under operational conditions which is essential in selection of stable process conditions and machine tool design for increased productivity.

8.2 Recommendations for Future Work

Although in this study a complete modeling procedure is presented, there are several aspects that need to be investigated further.

First of all, in this study bearing stiffness variations due to gyroscopic moments, centrifugal forces and cutting forces are investigated. However, effects of thermal variations are not included in the analysis. Therefore, an experimental set up which enables measurement of spindle temperature can be constructed and identification can be performed at various bearing temperatures. Thus, variation of the bearing stiffness values with increasing temperature can be identified.

Secondly, in this study, variations in the tool point FRFs are attributed to variations of the bearing dynamics and it is assumed that contact parameters at the spindle – holder and holder – tool interface remain same under operational conditions. Detailed analysis need to be performed by increasing preload on bearings since with increasing preload, variations in the bearing stiffness values decrease. Therefore, for high preloaded bearings, amount of deviations between in process and idle tool point FRFs should be lower than the observed deviations presented in this study. Such a further study will provide the validity of the contact parameter assumption. On the contrary, if the same deviations are observed in high preloaded bearing case, speed dependent contact parameters should also be identified and should be implemented to the model with the speed dependent bearing dynamics.

REFERENCES

- [1] S.A. Tobias, W. Fishwick, The chatter of lathe tools under orthogonal cutting conditions, Transactions of ASME 80 (1958) 1079-1088.
- [2] J. Tlustý, M. Poláček, The stability of machine tools against self-excited vibrations in machining, Proceedings of the ASME International Research in Production Engineering (1963) 465-474.
- [3] I. Minis, T. Yanushevsky, R. Tembo, R. Hocken, Analysis of linear and nonlinear chatter in milling, Annals of the CIRP 39 (1990) 459-462.
- [4] Y. Altintas, E. Budak, Analytical prediction of stability lobes in milling, Annals of the CIRP 44 (1995) 357-362.
- [5] E. Budak, Y. Altintas, Analytical prediction of chatter stability in milling – part I: general formulation; part II: application to common milling systems, Transactions of ASME, Journal of Dynamic Systems, Measurement, and Control 120 (1998) 22-36.
- [6] Y. Altintas, Manufacturing Automation, Cambridge University Press, (2000).
- [7] T. Schmitz, R. Donaldson, Predicting high-speed machining dynamics by substructure analysis, Annals of the CIRP 49 (1) (2000) 303-308.
- [8]] T. Schmitz, M. Davies, M. Kennedy, Tool point frequency response prediction for high-speed machining by RCSA, Journal of Manufacturing Science and Engineering 123 (2001) 700-707.

- [9] T. Schmitz, M. Davies, K. Medicus, J. Snyder, Improving high-speed machining material removal rates by rapid dynamic analysis, *Annals of the CIRP* 50 (1) (2001) 263-268.
- [10] E.B. Kivanc, E. Budak, Structural modeling of end mills for form error and stability analysis, *International Journal of Machine Tools and Manufacture* 44 (2004) 1151-1161.
- [11] G.S. Duncan, T. Schmitz, An improved RCSA model for tool point frequency response prediction, *Proceedings of the 23rd International Modal Analysis Conference*, January 30 – February 3, 2005, Orlando, FL (on CD).
- [12] A. Ertürk, H.N. Özgüven, E. Budak, Analytical modeling of spindle-tool dynamics on machine tools using Timoshenko beam model and receptance coupling for the prediction of tool point FRF, *International Journal of Machine Tools and Manufacture* 46 (2006) 1901-1912
- [13] E. Budak, A. Ertürk, H.N. Özgüven, A modeling approach for analysis and improvement of spindle-holder-tool assembly dynamics, *Annals of the CIRP* 55 (2006) 369-372
- [14] A. Ertürk, E. Budak, H.N. Özgüven, Selection of design and operational parameters in spindle-holder-tool assemblies for maximum chatter stability by using a new analytical model, *International Journal of Machine Tools and Manufacture* 47 (2007)1401-1409.
- [15] C.W. Lee, *Vibration Analysis of Rotors*, Kluwer Academic Publishers, Dordrecht (1993).

- [16] M.I. Friswell, J. E. T. Penny, S. D. Garvey, A. W. Lees, Dynamics of Rotating Machines, Cambridge Aerospace Series, (2010).
- [17] D.J. Ewins, Modal testing: Theory, practice and application, Research Studies Press, Baldock, Hertfordshire, England, (2000).
- [18] E. Rivin, Stiffness and Damping in Mechanical Design, Marcel Dekker Inc (1999).
- [19] B. J. Stone, The state of the art in the measurement of the stiffness and damping of rolling element bearings, CIRP Annals Manufacturing Technology 31 (1982) 529-538.
- [20] T. A. Harris, Rolling Bearing Analysis, 4th ed., John Wiley and Sons, New York (2001).
- [21] Y. Altintas, Y. Cao, Virtual design and optimization of machine tool spindles, CIRP Annals- Manufacturing Technology 54 (2005) 379-382.
- [22] Y. Cao, Y. Altintas, Modeling of spindle-bearing and machine tool systems for virtual simulation of milling operations, International Journal of Machine Tools & Manufacture 47 (2007) 1342-1350.
- [23] G. L. Xiong, J. M. Yi, C. Zeng, H. K. Guo, L. X. Li, Study of gyroscopic effect of the spindle on the stability characteristics of the milling system, Journal of materials Processing Technology 138 (2003) 379-384.
- [24] M. R. Movahhedy, P. Mosaddegh, Prediction of chatter in high speed milling including gyroscopic effects, International Journal of Machine Tools & Manufacture 46 (2006) 996-1001.

- [25] H. Li, Y. C. Shin, Analysis of bearing configuration effects on high speed spindles using an integrated dynamic thermo-mechanical spindle model, *International Journal of Machine Tools & Manufacture* 44 (2004) 347-364.
- [26] L. Hong, C.S. Yung, Analysis of bearing configuration effects on high speed spindles using an integrated dynamic thermo-mechanical spindle model, *International Journal of Machine Tools & Manufacture* 44 (2004) 347-364.
- [27] C. W. Lin, J. F. Tu, J. Kamman, An integrated thermo-mechanical-dynamic model to characterize motorized machine tool spindles during very high speed rotation, *International Journal of Machine Tools & Manufacture* 43 (2003) 1035-1050.
- [28] D. Nelson, A finite rotating shaft element using Timoshenko beam theory, *ASME Journal of Mechanical Design* 102 (4) (1980) 793–803.
- [29] C.W. Lee, *Vibration Analysis of Rotors*, Kluwer Academic Publishers, Dordrecht (1993).
- [30] Y. Kang, Y.P. Chang, J.W. Tsai, L.H. Mu, Y.F. Chang, An investigation in stiffness effects on dynamics of rotor–bearing–foundation systems, *Journal of Sound and Vibration* 231 (2000) 343–374.
- [31] G. H. Jang and S. H. Lee, Free vibration analysis of a spinning flexible disk spindle system supported by ball bearing and flexible shaft using the finite element method and substructure synthesis, *Journal of Sound and Vibration* 251(1) (2002) 59-78.

- [32] C. Eric, D. Flavio, Georges Jacquet-Richardet, Toward global modeling approaches for dynamic analyses of rotating assemblies of turbo machines, *Journal of Sound and Vibration* 282 (2005) 163–178.
- [33] K.L. Cavalca, P.F. Cavalcante, E.P. Okabe, An investigation on the influence of the supporting structure on the dynamics of the rotor system, *Mechanical Systems and Signal Processing* 19 (2005) 157–174.
- [34] D. Combescure, A. Lazarus, Refined finite element modeling for the vibration analysis of large rotating machines: Application to the gas turbine modular helium reactor power conversion unit, *Journal of Sound and Vibration* 318 (2008) 1262–1280.
- [35] D.A. Frew, C. Scheffer, Numerical modeling of a high-speed rigid rotor in a single-aerostatic bearing using modified Euler equations of motion, *Mechanical Systems and Signal Processing* 22 (2008) 133–154.
- [36] Y.S. Chena, Y.D. Chenga, T. Yang, K.L. Koai, Accurate identification of the frequency response functions for the rotor–bearing–foundation system using the modified pseudo mode shape method, *Journal of Sound and Vibration* 329 (2010) 644–658.
- [37] C.W. Lee, R. Katz, A. G. Ulsoy, R.A. Scott, Modal analysis of a distributed parameter rotating shaft, *Journal of Sound and Vibration* 122 (1988) 119-130.
- [38] C. W. Lee, Y. G. Jei, Modal analysis of continuous rotor-bearing systems, *Journal of Sound and Vibration* 126 (1988) 345-361.
- [39] Y.G. Jei, C.W. Lee, Modal analysis of continuous asymmetric rotor-bearing systems, *Journal of Sound and Vibration* 152 (1992) 245–262.

- [40] W. Wang, J. Kirkhope, New eigensolutions and modal analysis for gyroscopic/rotor systems, Part 1: Undamped systems, *Journal of Sound and Vibration* 175 (1994) 159-170.
- [41] W. Wang, J. Kirkhope, New eigensolutions and modal analysis for gyroscopic/rotor systems, Part 2: perturbation analysis for damped systems, *Journal of Sound and Vibration* 175 (1994) 171-183.
- [42] R.G. Parker, P. J. Sathe, Exact Solutions for the free and forced vibration of a rotating disk-spindle system, *Journal of Sound and Vibration* 223 (1999) 444-465.
- [43] S. W. Hong, J. H. Park, Dynamic analysis of multi-stepped, distributed parameter rotor-bearing systems, *Journal of Sound and Vibration*, 227 (1999) 769-785.
- [44] S. J. Rothberg, J.R. Baker, N.A. Halliwell, Laser vibrometry: pseudo-vibration, *Journal of Sound and Vibration* 135 (1989) 516–522.
- [45] M. Denman, N.A.Halliwell, S.J. Rothberg, Speckle noise reduction in laser vibrometry: experimental and numerical optimization, *Second International Conference on Vibration Measurements by Laser Techniques: Advances and Applications* (1996) 12–21.
- [46] K Tatara, M. Rantatalob, P. Grena, Laser vibrometry measurements of an optically smooth rotating spindle, *Mechanical Systems and Signal Processing* 21 (2007) 1739-1745.
- [47] J.R Bell, S.J. Rothberg, Laser vibrometers and contacting transducers, target rotation and six degree-of-freedom vibration: what do we really measure?, *Journal of Sound and Vibration* 237 (2000) 245–261.

- [48] J.R Bell, S.J. Rothberg, Rotational vibration measuring using laser doppler vibrometry: comprehensive theory and practical application, *Journal of Sound and Vibration* 238 (2000) 673–690.
- [49] J.R Bell, S.J. Rothberg, On the application of laser vibrometry to translational and rotational vibration measurements on rotating shafts, *Measurement* 35 (2004) 201–210
- [50] K. Tatar, P. Gren, Measurement of milling tool vibrations during cutting using laser vibrometry, *International Journal of Machine Tools and Manufacture* 48 (2007) 380-387.
- [51] I. Zaghbani, V. Songmene, Estimation of machine-tool dynamic parameters during machining operation through operational modal analysis, *International Journal of Machine Tools and Manufacture* 49 (2009) 947-957.
- [52] H. Opitz, M.C. Weck, Determination of the transfer function by means of spectral density measurements and its application to dynamic investigation of machine tools under machining conditions, 10th International MTDR Conference (1969) 349-378.
- [53] I. E. Minis, E.B Magrab, I.O. Pandelidis, Improved methods for the prediction of chatter in turning, Part 1: Determination of structural response parameters, *Transactions of the ASME* 112 (1990) 12-20.
- [54] E.Budak, L.T. Tunç, Identification and modeling process damping in turning and milling using a new approach, *Annals of the CIRP* 59 (2010) 403-408.

- [55] J.D. Aristizabal-Ochoa, Timoshenko beam-column with generalized end conditions and nonclassical modes of vibration of shear beams, *Journal of Engineering Mechanics* 130 (2004) 1151–1159.
- [56] H.N. Ozguven, Structural modifications using frequency response functions *Mechanical Systems and Signal Processing* 4 (1990) 53-63.
- [57] J.S. Bendat, A.G. Piersol, *Random Data Analysis and measurement Procedures*, Fourth edition, Wiley (2010).
- [58] J.S. Bendat, A.G. Piersol, *Engineering Applications of Correlation and Spectral Analysis*, 2nd Edition, Wiley-Interscience (1993).
- [59] K. Shin, J. Hammond, *Fundamentals of Signal Processing for Sound and Vibration Engineers*, Wiley (2008).
- [60] O. Özşahin, H. N. Özgüven, E. Budak, “Analysis and Compensation of Mass Loading Effect of Accelerometers on Tool Point FRF Measurements for Chatter Stability Predictions”, *International Journal of Machine Tools and Manufacture*, Vol. 50, No. 6, 585-589, 2010.
- [61] O. Özşahin, “An Investigation on Dynamic Contact parameters in Machining Center Spindle - Tool Assemblies”, M.Sc. thesis, Middle East Technical University, 2008.
- [62] Ozsahin, O., Erturk, A., Ozguven, H.N. and Budak, E., “A Closed-Form Approach for Identification of Dynamical Contact Parameters in Spindle-Holder-Tool Assemblies”, *International Journal of Machine Tools and Manufacture*, Vol. 49, pp. 25-35, 2009.

- [63] Ozsahin, O., Ozguven, H. N. and Budak, E., “Estimation Of Dynamic Contact Parameters For Machine Tool Spindle-Holder-Tool Assemblies Using Artificial Neural Networks”, Proceedings of the 3rd CIRP International Conference on Manufacturing Engineering (ICMEN), Kassandra, Greece, October 1-4, 2008.

CURRICULUM VITAE

PERSONAL INFORMATION

Surname, Name: Özşahin, Orkun

Nationality: Turkish (TC)

Date and Place of Birth: 11 August 1982, Aydın-Çine

Marital Status: Married

Cell Phone: +9 0 542 4548000

email: orkunozsahin@gmail.com

EDUCATION

Degree	Institution	Year of Graduation
Ph.D	METU Mechanical Engineering	2014
M.S.	METU Mechanical Engineering	2008
B.S.	METU Mechanical Engineering	2005

WORK EXPERIENCE

Year	Place	Enrollment
2008-2013	METU Department of Mechanical Engineering	Research Assistant
02.2008-12. 2008	TUSAS Aerospace Industry (TAI)	Structural Analysis Engineer
August 2004	Vestel	Intern Engineering Student
August 2003	BOSCH	Intern Engineering Student

PROJECTS INVOLVED

2011-2014

TUBİTAK supported project: Analysis, Modeling and Optimization of Simultaneous Machining Processes Performed on Multi-Tasking Machine Tools.

2008-2011

TUBİTAK supported project: Development of improved process stability and machine tool dynamics models for increased productivity in metal cutting operations.

2005-2008

TUBİTAK supported project: Increasing productivity of metal cutting operations in high speed machining centers by modeling of machine tool and workpiece dynamics.

PUBLICATIONS

Refereed Journal Papers

O. Özşahin, H. N. Özgüven, E. Budak, “Analysis and Compensation of Mass Loading Effect of Accelerometers on Tool Point FRF Measurements for Chatter Stability Predictions”, International Journal of Machine Tools and Manufacture, Vol. 50, No. 6, 585-589, 2010.

Ozsahin, O., Erturk, A., Ozguven, H.N. and Budak, E., “A Closed-Form Approach for Identification of Dynamical Contact Parameters in Spindle-Holder-Tool Assemblies”, International Journal of Machine Tools and Manufacture, Vol. 49, pp. 25-35, 2009.

Papers Published in Conference Proceedings

O. Ozsahin, E. Budak, H. N. Ozguven, "Analytical Modeling of the Machine Tool Spindle Dynamics under Operational Conditions" Proceedings of the – 37th MATADOR Conference, 24-27July, Manchester, UK, 2012.

O. Ozsahin, E. Budak, H. N. Ozguven, "Investigating Dynamics of Machine Tool Spindles under Operational Conditions", Proceedings of the 13th CIRP Conference on Modeling of Machining Operations, 12-13 May 2011, Sintra, Portugal, Advanced Materials Research, Vol. 223, pp. 610-621, 2011.

Özşahin, O., Özgüven, H. N. and Budak, E., "Mass Loading Effect of Accelerometers on Tool Point FRF and Stability Diagrams", Proceedings of the 12th CIRP Conference on Modeling of Machining Operations, San Sebastian, Spain, May 12-13, 2009.

Ozsahin, O., Ozguven, H. N. and Budak, E., "Estimation Of Dynamic Contact Parameters For Machine Tool Spindle-Holder-Tool Assemblies Using Artificial Neural Networks", Proceedings of the 3rd CIRP International Conference on Manufacturing Engineering (ICMEN), Kassandra, Greece, October 1-4, 2008.

E. Özlü, O. Özşahin, H.N. Özgüven, E. Budak, 'The Use of Noise Measurement in Machining Stability Analysis' The 36th International Congress and Exhibition on Noise Control Engineering, İstanbul, Turkey, 28-31 August 2007.